

Electron spin resonance studies of frustrated quantum spin systems

DISSERTATION

zur Erlangung des akademischen Grades

Doctor rerum naturalium
(Dr. rer. nat.)

vorgelegt

der Fakultät
Mathematik und Naturwissenschaften



von

Dmytro Kamenskyi
geboren am 11.08.1983 in Kharkiv, Ukraine

HLD.



HOCHFELD-MAGNETLABOR DRESDEN
Helmholtz-Zentrum Dresden-Rossendorf e. V.
2012

GUTACHTER:

Prof. Dr. Joachim Wosnitza
Prof. Dr. Bernd Pilawa

Eingereicht am: 21.11.2012

Tag der Verteidigung: 19.03.2013

Abstract

Since the last few decades frustrated spin systems have attracted much interest. These studies are motivated by the rich variety of their unusual magnetic properties and potential applications. In this thesis, excitation spectra of the weakly coupled dimer system $\text{Ba}_3\text{Cr}_2\text{O}_8$, the spin-1/2 chain material with distorted diamond structure $\text{Cu}_3(\text{CO}_3)_2(\text{OH})_2$ (natural mineral azurite), and the quasi-two-dimensional antiferromagnet with triangle spin structure Cs_2CuBr_4 have been studied by means of high-field electron spin resonance. Two pairs of gapped modes corresponding to transitions from a spin-singlet ground state to the first excited triplet state with zero-field energy gaps, of 19.1 and 27 K were observed in $\text{Ba}_3\text{Cr}_2\text{O}_8$. The observation of ground-state excitations clearly indicates the presence of a non-secular term allowing these transitions. Our findings are of crucial importance for the interpretation of the field-induced transitions in this material (with critical fields $H_{c1} = 12.5$ T and $H_{c2} = 23.6$ T) in terms of the magnon Bose-Einstein condensation. The natural mineral azurite, $\text{Cu}_3(\text{CO}_3)_2(\text{OH})_2$, has been studied in magnetic fields up to 50 T, revealing several modes not observed previously. Based on the obtained data, all three critical fields were identified. A substantial zero-field energy gap, $\Delta = 9.6$ K, has been observed in Cs_2CuBr_4 above the ordering temperature. It is argued that contrary to the case for the isostructural Cs_2CuCl_4 , the size of the gap can not be explained solely by the uniform Dzyaloshinskii-Moriya interaction, but it is rather the result of the geometrical frustration stabilizing the spin-disordered state in Cs_2CuBr_4 in the close vicinity of the quantum phase transition between a spiral magnetically ordered state and a 2D quantum spin liquid.

Contents

Abstract	iii
1 General properties of frustrated spin systems	1
1.1 Introduction	1
1.2 Frustrated compounds and Dzyaloshinskii-Moriya interaction . . .	10
2 Experimental methods	17
2.1 General remarks on electron spin resonance	17
2.2 Experimental techniques	21
2.2.1 Microwave-cavity technique	24
2.2.2 Transmission method	27
2.2.3 Torque detection of ESR	28
3 ESR studies of the quantum spin-dimer system $\text{Ba}_3\text{Cr}_2\text{O}_8$	35
3.1 Introduction	35
3.2 Experimental details	39
3.3 Results and discussion	39
3.4 Conclusion	47
4 Magnetic properties of the quasi-one-dimensional frustrated compound $\text{Cu}_3(\text{CO}_3)_2(\text{OH})_2$	49
4.1 Introduction	49
4.2 Experimental details	56
4.3 Results	57
4.4 Discussion	64
4.4.1 Dimer-Monomer model	64
4.4.2 Triangular model	66
4.4.3 Energy-level diagram	69
4.4.4 Six-spin model	76
4.5 Conclusion	79
5 Magnetic excitations in the two-dimensional frustrated system Cs_2CuBr_4	81

Contents

5.1	Introduction	81
5.2	Experimental details	88
5.3	Results and discussion	88
5.4	Conclusions	94
6	Summary	95

1 General properties of frustrated spin systems

1.1 Introduction

Studies of cooperative phenomena in magnetism has provided rich ground for testing theories of interacting spin systems. Magnetic systems provide a very good benchmark for generic concepts pertaining to collective phenomena in nature. This is due in part to the availability of a large variety of diverse magnetic materials, that can be chosen to approximate simple theoretical toy models of collective behavior, and, in part, to their ease of study by a lot of experimental techniques [1].

The ground state of a system is very important to understand if we are talking about low-temperature properties and cooperative phenomena of a solid state. Magnetic interactions play an important role in the formation of the ground state in compounds which contain magnetic ions (such as $3d$ and $4d$ transition-metal or rare-earth ions). Some compounds have magnetic interactions between ions that compete with each other. Compounds with such kind of interactions are called frustrated. Frustrated magnetic systems are very interesting because their ground state is difficult to predict. Generally speaking, frustration arises when a system cannot minimize the energy of all pairwise interactions simultaneously because of local geometric constraints. Frustration can lead to exotic phenomena such as macroscopic degeneracies and qualitatively new ground states of matter [2, 3]. In the most extreme case, a system can have a disordered ground state with macroscopic degeneracy; that is, it comprises a huge number of equivalent states of the same energy [1–4]. For example, Wannier showed in 1950 that a triangular lattice of Ising spins has a very large degeneracy of its ground state [5].

Toulouse [6] is often credited with introducing the general concept of magnetic frustration, a term applied to the situation when a large fraction of magnetic sites in a lattice is subject to competing or contradictory constraints. However, we want to note that some specific cases had been described even earlier, for example by Anderson [7] or Wannier [5].

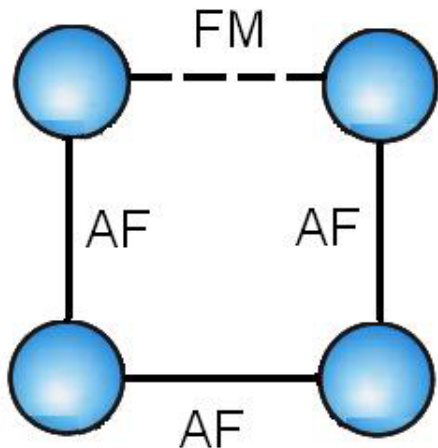


Figure 1.1: Plaquette of the square antiferromagnetic lattice with one bond replaced by a ferromagnetic bond, illustrating frustration induced by site disorder common to most spin glasses.

It is important to distinguish two classes of materials where frustration effects are observed, spin glasses and geometrically frustrated magnets. A good example of a spin-glass material is CuMn , where the diluted Mn atoms are located at random sites in the Cu host. Frustration occurs since the interaction between the Mn atoms is of the Ruderman-Kittel-Kasuya-Yosida type, which is changing signs with a period given by the Fermi wavelength. The Mn-Mn interaction is thus both random and competing, which leads to frustration. This is illustrated in a simpler fashion in Fig. 1.1 where a square lattice with magnetically interacting spins is shown. Introduction of a randomly placed ferromagnetic (FM) bond, e.g. by modifying the exchange interaction by hole doping such as in La_2CuO_4 [8], leads to frustration that results from nearly symmetric and competing interactions; the local field at one spin on the plaquette is much smaller than at its neighbors. A similar situation occurs when the disorder involves site substitution of spins, such as in the case of $\text{Eu}_x\text{Sr}_{1-x}\text{S}$ [4].

The main objects investigated in the framework of this thesis are systems with strong geometric frustrations. Geometric frustrations arise in materials containing antiferromagnetically coupled magnetic moments which reside on geometric units, such as triangles or tetrahedra, that inhibit the formation of a collinear magnetically ordered state. Frustrated systems on a regular lattice or geometrically frustrated systems are worthwhile to study, since we can investigate the frustration effects on the physical properties, not being worried by randomness,

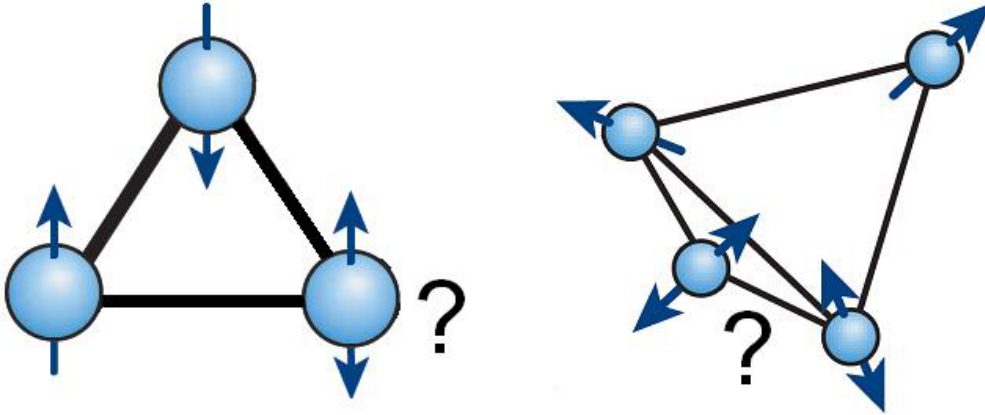


Figure 1.2: Examples of geometrically frustrated spin arrangements: a) equilateral triangle, b) tetrahedron.

which is inevitable in a spin-glass systems. Examples of geometrically frustrated cells are shown in Fig. 1.2.

A triangle of antiferromagnetically interacting spins is the simplest example of frustrations (see Fig. 1.2a). I consider this system in more details. The Hamiltonian for the exchange interaction between two spins can be written as

$$\mathcal{H}_{ex} = -2JS_1 \cdot S_2, \quad (1.1)$$

where J is the exchange constant, S_1, S_2 are the interacting spin operators. The energy is minimized for collinear spin alignments. With $J < 0$ and one J for all nearest-neighbor (nn) pairs of spins in the triangle, we can see that only two of the three spin constraints can be satisfied simultaneously. All three spins cannot be antiparallel. As a result, there are six ground states (three Kramers doublets) (see Fig. 1.3), instead of two caused by the Ising symmetry (up or down) [2]. Such degeneracies can persist for 2D and 3D lattices as well. For example, the ground-state entropy for the ideal triangular Ising paramagnet is extensive and equals $0.323k_B N$, where k_B is the Boltzmann constant and N is the number of spins. The spins fluctuate thermally at low temperatures, although in a correlated manner because they are restricted to the ground state of the Ising antiferromagnet. By analogy to an ordinary liquid, in which the molecules form a dense, highly correlated state that has no static order, the spins in the triangular Ising antiferromagnet form a spin liquid, or cooperative paramagnet.

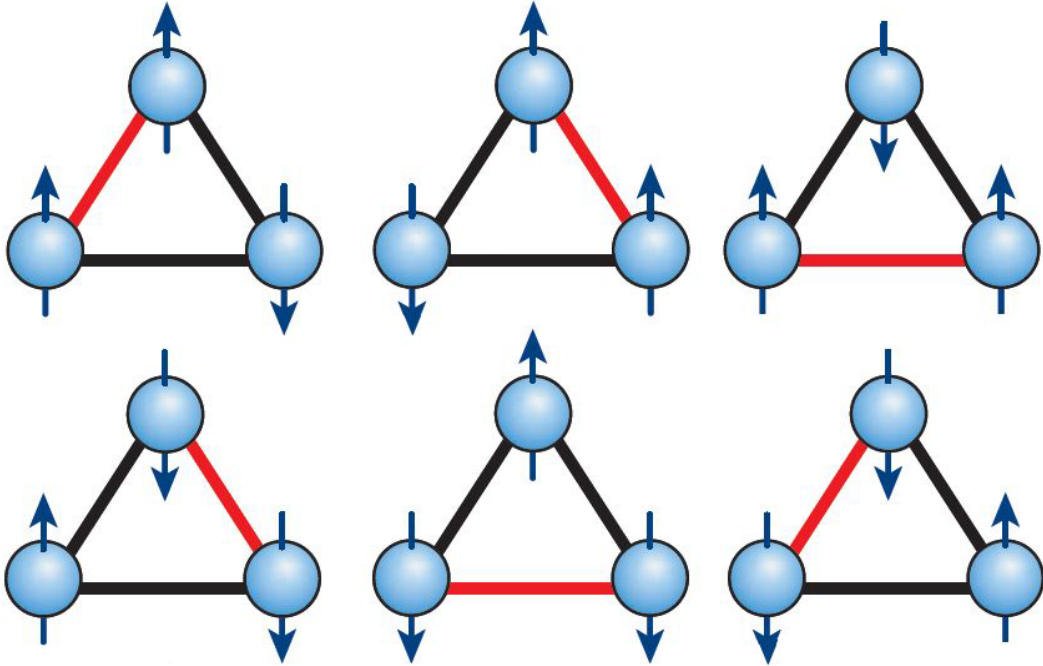


Figure 1.3: Degeneracy of the triangular antiferromagnetical interacted triangular spin system. Blue circles denote magnetic ions, arrows indicate the direction of spin, and red lines denote the axis on which the spins are parallel. From Ref. [2].

The exchange constant, J , can be different for different spin pairs in real crystals. Therefore, the Hamiltonian (1.1) should be rewritten as the sum of exchange energies between nn spins:

$$\mathcal{H}_{ex} = -1/2 \sum_{ij} J_{ij} \mathbf{S}_i \cdot \mathbf{S}_j. \quad (1.2)$$

If J_{ij} is different for different i and j , the degeneracy will be partially removed. This can lead to a rich excitation spectrum of the system. A similar situation is realized in materials investigated in this work, namely $\text{Cu}_3(\text{CO}_3)_2(\text{OH})_2$ (azurite) and Cs_2CuBr_4 . It has also been shown, theoretically and experimentally, that the ground-state degeneracy can be removed by small perturbations. These perturbations can arise from thermal or quantum fluctuations, single-ion anisotropy, Dzyaloshinskii-Moriya (DM) interactions, dipole-dipole interaction, next-nearest-neighbor interactions. Electron spin resonance (ESR) is one of the most powerful methods to study the energy diagram of excitations in such energy scale (10 GHz - 1 THz, or 0.3 - 35 cm^{-1} , or 0.5 - 50 K). The applications

of the ESR for frustrated systems are discussed in detail in the experimental part of the thesis.

There are a lot of examples of realizable lattices based on the triangle, in the same way that square and cubic lattices are based on a square (Fig. 1.4). The most obvious example of a geometrically frustrated system is that of AF interacting spins arranged on the triangular lattice, as shown in Fig. 1.4b. A three-dimensional analogue of the triangular lattice is the face-centered-cubic lattice (FCC), shown in Fig. 1.4d. Here, as is clear from the lines drawn to depict the nearest-neighbor interactions, it is most realistic to view the FCC lattice as a set of edge-sharing tetrahedra, the tetrahedron being the three-dimensional frustrated entity. The two-dimensional Kagomé lattice ($\text{SrCr}_8\text{Ga}_4\text{O}_{19}$), shown in Fig. 1.4c, is distinguished from the triangular lattice by virtue of having corner-sharing triangles. The three-dimensional analogue is the pyrochlore lattice (Fig. 1.4e) [4]. The one-dimensional diamond lattice ($\text{Cu}_3(\text{CO}_3)_2(\text{OH})_2$, $\text{Cu}_3\text{Mo}_2\text{O}_9$) is shown in Fig. 1.4a.

One of the main motivations for the current interest in these systems stems from suggestions that the frustration and zero-temperature spin fluctuations drive these systems into novel quantum disordered ground states. How can one identify frustration in experiments?

All systems of interest are sufficiently concentrated that magnetic interactions are expected on an energy scale set by the exchange energy, $H_{ex} \sim -2JS^2 \sim k_B T$, where $T \gg 0$ and k_B is the Boltzmann constant. A simple experimental measure of the exchange energy is provided by the familiar Curie-Weiss temperature, Θ_{CW} , which appears in the Curie-Weiss law,

$$\chi = C/(T - \Theta_{CW}), \quad (1.3)$$

where χ is the magnetic susceptibility, C the Curie constant, and T the temperature. From mean-field theory (MF) [9] it can be shown that

$$\Theta_{CW} = 2S(S + 1)/3k \sum Z_n J_n, \quad (1.4)$$

where n is the n -th neighbor and J_n is the corresponding exchange constant, i.e., Θ_{CW} is the algebraic sum of all of the exchange interactions in any magnetic system and, thus, the Curie-Weiss constant sets the energy scale for the magnetic interactions. This constant can be calculated from magnetic-susceptibility data at temperature well above the phase transition. In Fig. 1.5, it is shown how frustration is identified from magnetic-susceptibility data. In the absence of frustration one expects the onset of strong deviations from the Curie-Weiss law for $T \simeq |\Theta_{CW}|$ and the establishment of a long-range ordered state also near Θ_{CW} . For ferromagnetic order this is nearly realized, as $|\Theta_{CW}|/T_C \simeq 1$.

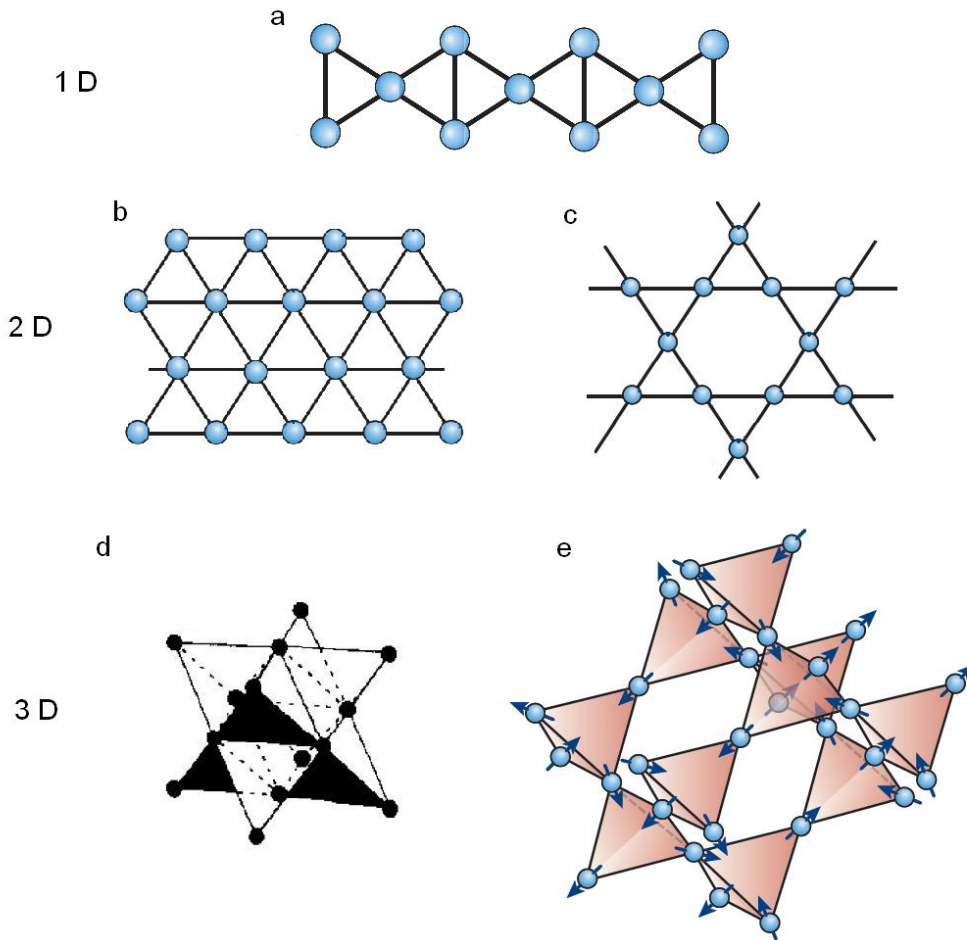


Figure 1.4: Examples of frustrated magnetic lattices. a) Diamond chain, b) triangular lattice, c) Kagomé lattice, d) face-centered cubic lattice, e) pyrochlore lattice.

T_C is the critical temperature below which the long-range ordered state is established.

For antiferromagnetic order, the situation is a bit more complex and the ratio depends on the exact magnetic structure which is adopted but typical values for non-frustrated lattices show a ratio $|\Theta_{CW}|/T_C$ in the range of 2 to 5. For example $|\Theta_{CW}|/T_C$ for LnCrO_3 (Ln is a lanthanid) perovskites in which the simple cubic magnetic sublattice is non-frustrated, ranges from 2 to 3 [10].

More general, it is apparently a characteristic property of geometrically frustrated magnets that they do not order at the temperature expected from the magnitude of the Curie-Weiss constant Θ_{CW} (Fig. 1.5). Instead, they remain in the paramagnetic phase to a much lower temperature with, typically, a spin freezing at $T_f \ll \Theta_{CW}$ [11].

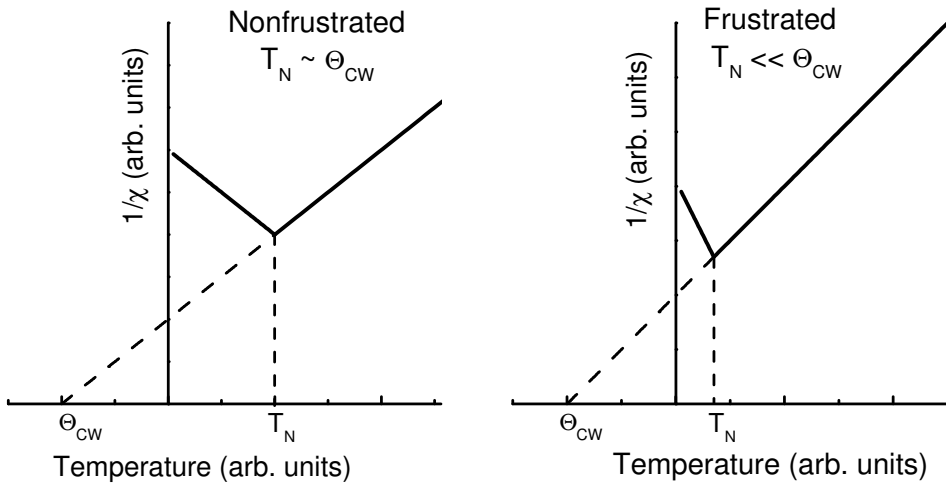


Figure 1.5: Identification of frustrations in antiferromagnetic systems. The left side shows a typical behavior of the inverse susceptibility, $1/\chi$, versus temperature for a nonfrustrated AF, where $\Theta_{CW} \sim T_N$ (T_N - the Neel or ordering temperature). The right side shows a typical curve for a frustrated magnet, where $T_N \ll \Theta_{CW}$.

Thus, we can define an empirical measure of frustration by the relation:

$$f = |\Theta_{CW}|/T_C. \quad (1.5)$$

It has been proposed that the somewhat arbitrary condition, $f > 10$, may be taken as a criterion for the presence of frustration [4]. As will be shown below, in the case of ground states which are not long-range ordered, such as spin glasses, the freezing temperature, T_f , is substituted for T_C .

We have to note that the phenomenon of a transition temperature much lower than predicted by a given exchange constant and number of nearest neighbors is known not only for geometrically frustrated systems. There are

examples of non-frustrated compounds where T_C can be suppressed. One-dimensional (1D) systems, for example, do not undergo long-range ordering. In two-dimensional (2D) case, long-range configurational order only occurs for Ising systems [12]. Therefore, this effect should not be confused with the effect of geometrical frustration. But, there is a clear difference between low dimensionality and frustrations. Low-dimensional magnetic systems develop correlations well above Θ_{CW} given by equation (1.4), as would any non-frustrated system - order parameter fluctuations are not suppressed at high temperatures, they just never develop fully below Θ_{CW} . As a result, there still remains the difficulty in determining this parameter via bulk-susceptibility measurements. So, low-dimensional systems gain entropy by a rarefication of spin density, whereas strong geometrically frustrated (SGF) systems gain entropy by a particular dense spin arrangement. One expects qualitatively different ways how the two system types approach the zero-entropy ground state, and for SGF magnets there will emerge new physics at low temperatures of a type not anticipated by MF or spin-wave theory [4].

Over the last 60 years, experimentalists have found new classes of frustrated magnetic behavior, and theoreticians have been motivated by the broad conceptual applicability of magnetic models to investigate simple frustrated spin systems. These include generalizations of the spin-ice model that display a wealth of interesting thermodynamic phenomena in close resemblance with those observed in real ice. However, although theoretical studies of ice-like phenomena in frustrated spin-ice have long been known, very few, if any, real magnets could be found to display such a behavior. This remained for some time a disappointing situation where close contact between theoretical studies on magnetic-ice models and real systems was lacking, a somewhat untenable predicament in science where one is generally aiming at testing of the theoretical concepts against experiments and vice versa [1].

We noted before that the ground state of a system is very important for its low-temperature properties. We will use the ground-state properties as a criterion for the classifications of SGF compounds. We can divide conditionally all SGF by this criterion into two classes: systems with a long-range ordered ground state and systems with the ground state without long-range ordering.

The possibility to find a long-range ordered magnetic system is determined by the dimensionality of the lattice d and the spin dimensionality D . One can write the Hamiltonian (1.1) in the expanded form

$$\mathcal{H}_{ex} = -2J(S_i^x S_j^x + S_i^y S_j^y + S_i^z S_j^z). \quad (1.6)$$

Parameter D is equal to the number of spin components (x,y,z) which must be taken into account. The case $D = 1$ is known as the Ising model, $D = 2$

corresponds to the X-Y model, and $D = 3$ is the isotropic Heisenberg model. Mermin and Wagner showed in 1966 that only $d = 3$ Heisenberg systems can undergo true long-range order [13]. With the famous exception of $2d$ Ising model. The presence of frustration in the magnetic subsystem make this situation much more complicated.

Long-range-ordered ground state. In computer simulations of periodic site-ordered systems, frustration leads to a variety of unusual topological excitations and ordering phenomena. In real compounds, however, there usually exist additional interactions which relieve the frustration and allow the system to order at a temperature comparable to the dominant interaction strength. For example, in antiferromagnetic oxides such as α - Fe_2O_3 and La_2CuO_4 , DM interaction is responsible for weak ferromagnetism. Thus, in SGF systems, interactions which are negligibly in classical antiferromagnets play often a very important role. These can be interactions beyond next neighbors, DM interaction, dipole coupling, *etc.*

Ground states without long-range order. A lot of materials with frustrated lattices do not exhibit a phase transition to a long-range ordered state. From a microscopic point of view it has long been recognized that such lattices possess a large degeneracy. For example, any configuration in which all tetrahedra are, separately, in a minimum energy state is a ground state. This can be obtained for the case when each tetrahedron has two pairs of antiparallel spins, but there is no correlation between tetrahedra. There exists an enormous number of such configurations and no unique, long-range-ordered state can emerge. Villain has chosen to describe such systems with the oxymoronic label, cooperative paramagnet [14]. The inclusion of the term paramagnetic here also implies that such a system is dynamic, i.e., spin fluctuations should persist at all temperatures. These ideas have been tested at a lot of levels of theory and all possible spin dimensionalities and the accepted consensus is that the pyrochlore lattice with nn antiferromagnetic interactions does not support static, long-range order above 0 K [15].

Non-collinear spin configurations. Most frustrated systems which do undergo a phase transition to a long-range-ordered state adopt so-called non-collinear or compensated spin configurations.

The canonical example is the triangular lattice in which the three spins are aligned at 120° (Fig. 1.6, left) which results in a vector sum of zero for the plaquette and the lattice, thus, globally satisfying the antiferromagnetic constraint. The corresponding compromise configuration for the tetrahedral plaquette and pyrochlore lattice is the 109° structure (Fig. 1.6, right). In both cases there is more than one way to achieve these non-collinear configurations which introduces degeneracy, due to chirality, into the ground state. It should be

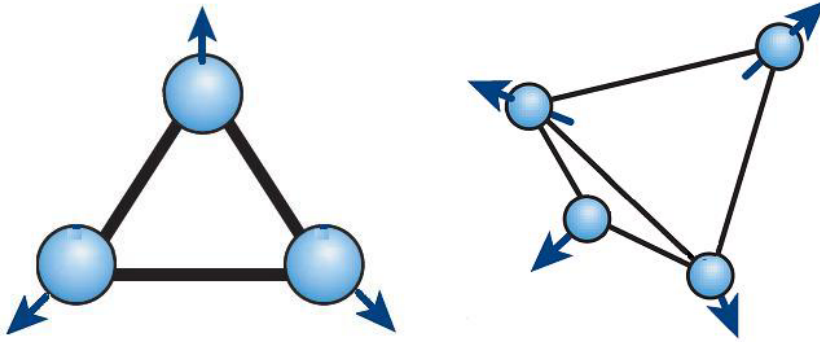


Figure 1.6: Examples of compromise non-collinear magnetic structures.

noted that Ising spins ($D = 1$) on the triangular lattice cannot adopt the compromise structure; two spins can be aligned antiparallel but one will remain frustrated [15].

For actual materials, the 120° structure is found quite commonly for triangular planar lattices. One of such compounds is YMnO_3 [16]. The 109° structure has been reported only for one pyrochlore-lattice compound, namely py-FeF_3 (where *py* is pyrochlore). Materials with the pyrochlore structure, *e.g.* $\text{Y}_2\text{Mo}_2\text{O}_7$, often adopt short-range-ordered ground states and materials with the spinel structure, ZnFe_2O_4 or CoCr_2O_4 for example, adopt very complex spin configurations with large magnetic unit cells as will be discussed in the following. For spinels, the influence of interactions well beyond the next-neighbor level is believed to be important [17].

1.2 Frustrated compounds and Dzyaloshinskii-Moriya interaction

In this section, we discuss in more detail the general physical properties of the strongly geometrically frustrated systems. Table 1 lists several compounds with different degrees of frustration. Following Ramirez [4], I introduce the frustration parameter f (Eq. 1.5) for low-dimensional compounds as well. However, we should keep in mind that the f values for the low-dimensional compounds comprises not only frustration effects but also effects of reduced dimensionality. There is a wide range of Θ_{CW} , from 2.3 to 1000 K, and materials whose ground state is either AF or spin glass (SG), depending on the presence or absence of magnetic site disorder. The most obvious similarity between the compounds is that all have magnetic lattices built out of triangles. For the 2D compounds,

1.2 Frustrated compounds and Dzyaloshinskii-Moriya interaction

Compound	Magnetic lattice	$ \Theta_{CW} $, K	T_N , K	f	Ground state, Ref.
low-dimensional magnets					
LiCrO ₂	triangular	490	15	33	AF, [18]
NiGa ₂ S ₄	triangular	80	< 0.35	> 220	–
SrCr ₃ Ga ₄ O ₁₉	Kagome	515	3.5	150	SG, [19]
ZnCu ₃ (OH) ₆ Cl ₂	Kagome	300	< 0.05	> 6000	–, [20]
*Cu ₃ (CO ₃) ₂ (OH) ₂ (azurite)	diamond	...	1.86	...	AF
Cu ₃ Mo ₂ O ₉	diamond	43	10	4.3	AF, [21]
*Ba ₃ Cr ₂ O ₈	triangular	490	15	33	AF
Sr ₃ Cr ₂ O ₈	triangular	490	15	33	AF
*Cs ₂ CuBr ₄	triangular	...	1.4		–
*Cs ₂ CuCl ₄	triangular	4	0.62	6.5	–
YMnO ₃	triangular	471	71	5.9	AF, [16]
LuMnO ₃	triangular	519	90	5.8	AF, [16]
ScMnO ₃	triangular	495	130	3.8	AF, [16]
three-dimensional magnets					
ZnCr ₂ O ₄	B-spinel	390	12	32.5	AF, [22]
CoCr ₂ O ₄	B-spinel	500	94	5	FM, [23]
FeSc ₂ S ₄	diamond	45	< 0.05	230	AF, [24]
MnSc ₂ S ₄	diamond	23	2.1	10	AF, [24]
Dy ₂ Ti ₂ O ₇	pyrochlore		< 0.05	–	–, [11]
Ho ₂ Ti ₂ O ₇	pyrochlore	2	< 0.05	> 40	–, [25]
CsNiFeF ₅	pyrochlore	210	4.4	48	SG, [26]
Gd ₃ Ga ₅ O ₁₂	garnet	2.3	< 0.03	> 75	–, [27]

Table 1.1: Strongly geometrically frustrated magnets. Compounds described in this thesis are marked by an asterisk.

the lattices are either triangular or Kagomé-like. The three-dimensional lattices are mostly based on tetrahedra, although for the garnet $\text{Gd}_3\text{Ga}_5\text{O}_{12}$, the lattice is more complicated, yet still incorporates triangles. The other similarity among the materials in Table 1 is the single-ion symmetry of the magnetic constituent. Nearly all compounds in this list possess highly isotropic ions, either s-state ions such as Mn^{2+} or Gd^{3+} or transition-metal ions with fully quenched orbital moments. This is consistent with expectations for ordering based on numerical and MF theory modeling [28].

A canonical example of three-dimensional systems with competing interactions is a compound with spinel structure. The study of such compounds actually began about five decades ago. In 1952, experimental studies of chromites with spinel structures (ZnCr_2O_4 , CoCr_2O_4 , *etc*) indicated that the magnetic properties cannot be understood in frame of the Neel theory based on the Weiss MF approximation [29]. The crystal structure has FCC translational symmetry and six magnetic sites per unit cell, two tetrahedral (A sites) and four octahedral (B sites). The strong frustration of the exchange interactions between the ions on the B sites leads to a very rich $B - T$ phase diagram with exotic noncollinear phases. As an example, Fig. 1.7 shows the $B - T$ phase diagram of CoCr_2O_4 . The Curie-Weiss temperature of this compound is around 600 K. However, ferrimagnetic ordering of the Co^{2+} ions (A sites) appears at 94 K. Because of frustration, the Cr^{3+} ions (B sites) form a spiral structure at 50 K, well below Θ_{CW} . There are also a few reorientation transitions at lower temperature. Very recently, a new phase transition in CoCr_2O_4 was discovered (see Fig. 1.7) [23].

One experimental signature of strong frustration is the downward shift in spectral weight, a direct result of local degeneracy – this is the key feature that distinguishes geometric frustration from other effects that reduce the ordering temperature, T_c , to values well below that predicted by MF theory (Eq. 1.4) [33]. The phase diagram of classical antiferromagnets at low temperature is mostly described by the competition between long-range order and the Zeeman energy. However, little is known about how the reduced energy scale for spin freezing in GFMs changes with applied field. This energy scale can be up to two orders of magnitude lower than the mean-field energy, which motivates the question of whether the Zeeman energy competes with the exchange interaction on the MF scale or at this reduced scale. The downward shift of the excitation energies makes ESR a very useful method to investigate SGF compounds.

I have noted before in SGF compounds any small perturbation may have a strong effect on the ground-state properties. An example of such perturbation is DM interaction. This interaction plays a very important role in the resonance properties of the materials. I will analyze the influence of DM interaction

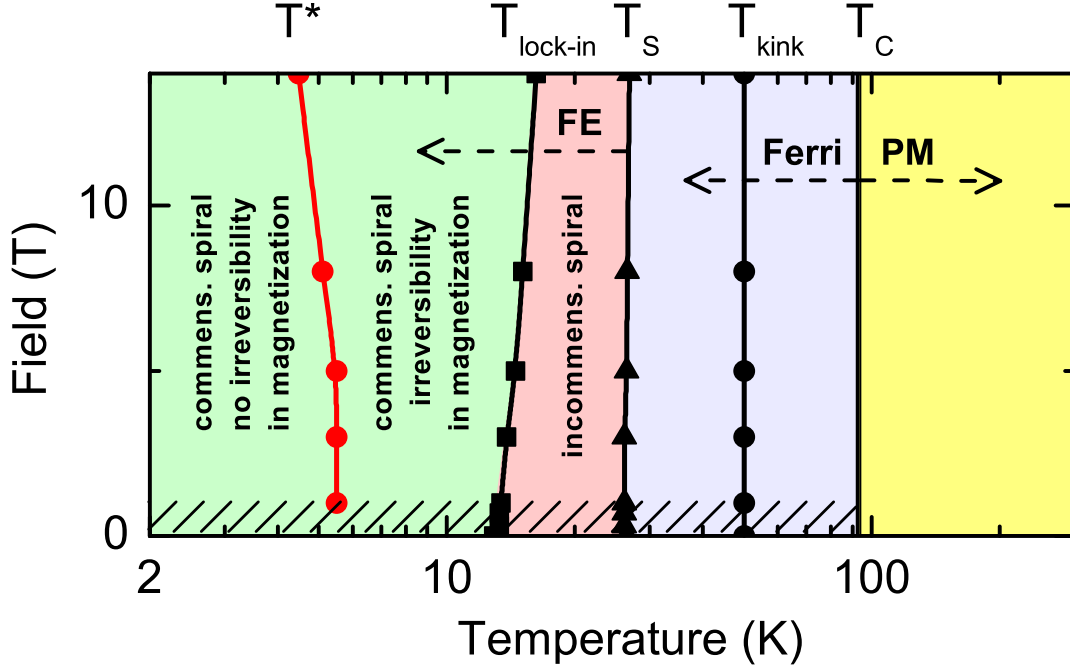


Figure 1.7: The temperature-field phase diagram of CoCr_2O_4 [23].

on the magnetic properties in the experimental part of this thesis. Here, I discuss the nature of this interaction.

In 1960, Moriya developed a theory of anisotropic superexchange interactions extending the Anderson theory of superexchange by including spin-orbit coupling [34]. An antisymmetric spin coupling was suggested by I. Dzyaloshinskii [35] from purely symmetry grounds and the symmetric pseudodipolar interaction was derived by Moriya. DM interaction between two ions i and j is defined by a vector \mathbf{D}_{ij} :

$$H_{ij} = \mathbf{D}_{ij}(\mathbf{S}_i \times \mathbf{S}_j). \quad (1.7)$$

The order of magnitude is estimated to be

$$|\vec{D}| \approx J_0 \cdot \Delta g/g, \quad (1.8)$$

where g is the gyromagnetic ratio and Δg the deviation of g from the value for a free electron ($g_e = 2.0023$). Thus, the spin Hamiltonian (1.2) can be written in the more general form:

$$H_{ex} = -1/2 \sum_{ij} (J_{ij} \mathbf{S}_i \cdot \mathbf{S}_j + \mathbf{D}_{ij}(\mathbf{S}_i \times \mathbf{S}_j) + \mathbf{S}_i \overline{A_{ij}} \mathbf{S}_j), \quad (1.9)$$

where the second term \mathbf{D}_{ij} is the antisymmetric DM interaction and the third term $\overline{A_{ij}}$ is an anisotropic symmetric exchange interaction. The $\overline{A_{ij}}$ is proportional to $(\Delta g/g)^2$. This last term, being one order of magnitude smaller than the DM interaction is often neglected.

In an actual crystal, some components of the symmetric and antisymmetric coupling tensors vanish because of the crystal symmetry. Moriya discussed the antisymmetric coupling from the crystal symmetry point of view. The coupling between two ions in the crystal is considered first. The two ions 1 and 2 are located at the points A and B, respectively, and the point bisecting the straight line AB is denoted by C. The following rules were obtained by Moriya:

- (i) When a center of inversion is located at C, then $\mathbf{D} = 0$.
- (ii) When a mirror plane perpendicular to AB passes through C, then \mathbf{D} is parallel to the mirror plane or \mathbf{D} is perpendicular to AB.
- (iii) When there is a mirror plane including A and B, then \mathbf{D} is perpendicular to the mirror plane.
- (iv) When a two-fold rotation axis perpendicular to AB passes through C, then \mathbf{D} is perpendicular to the two-fold axis.
- (v) When there is an n -fold axis ($n \geq 2$) along AB, then \mathbf{D} is parallel to AB.

Kagome and pyrochlore lattices (Fig. 1.4) are examples of frustrated spin systems where lattice symmetry allows DM interactions. In particular, the magnetism of this lattices continues to yield surprising low-temperature properties. These properties include SG ground states, spin-liquid behavior [32], cooperative paramagnetism, and ice-like zero-point entropy [36].

One of the best-studied substances with Kagome structure is the layered compound $\text{SrCr}_8\text{Ga}_4\text{O}_{19}$ (SCGO). The discovery by Obradors *et al.* [30] of the magnetoplumbite-like insulator compound SCGO with a very large degree of magnetic frustration ($f \simeq 150$), has generated a considerable amount of experimental and theoretical efforts that tried to clarify the properties of this compound and to analyze the features of geometrically frustrated systems. Now, SCGO can be considered as a model substance with Kagome lattice. This compound was studied in detail by numerous of methods: magnetic susceptibility [30, 32], specific heat [19, 32], neutron scattering [38]. Ramirez *et al.* found hysteretic behavior in the DC susceptibility, similar to that of a spin glass, occurring at 3.5 K [32]. The authors proposed that SCGO is a manifestation of a quasi-two-dimensional spin glass, where the correlated spin motion is mainly in the two-dimensional planes except in the vicinity of the transition to three-dimensional order, which occurs at a temperature much lower than the effective temperature because of a small interlayer coupling. Neutron-scattering studies by Broholm *et al.* confirmed the two-dimensional nature of the interactions. In addition, the authors were able to estimate the fraction of moment frozen

into a static configuration and found the surprising result that this accounted for only 25% of the total moment. In other words, ground-state quantum fluctuations account for 75% of the total moment. SCGO was also investigated by means of ESR [31]. But, the authors were focusing on another results (magnetic susceptibility, neutron diffraction) and did not analyze their ESR data in details. They just note a good agreement of the obtained ESR data with magnetic-susceptibility data and the broadening of the ESR line near critical temperature (3.5 K).

A detailed analysis of ESR data in an other Kagome-lattice compound, $\text{ZnCu}_3(\text{OH})_6\text{Cl}_2$, was provided by A. Zorko *et al.* [39]. Based on the analysis of the temperature dependence of their ESR spectra, the authors determined the value of the DM interaction. In addition, they found that DM interaction is the dominant magnetic anisotropy term in the Kagome spin-1/2 compound $\text{ZnCu}_3(\text{OH})_6\text{Cl}_2$.

Probably the most frustrated spin system is the classical Heisenberg antiferromagnet on the pyrochlore lattice (Fig. 1.4e) where the spins reside in the corners of tetrahedra. The number of classical ground states is so large that the system does not order at any finite temperature (as observed for instance for $\text{Dy}_2\text{Ti}_2\text{O}_7$ and $\text{Ho}_2\text{Ti}_2\text{O}_7$) [11, 25]. In a number of other pyrochlore-lattice compounds, as well as in other frustrated systems, deviations from the classical Heisenberg model (e.g., dipolar interactions, single-ion anisotropy, DM interactions) determine which ground state is selected at the lowest temperatures. For a review of magnetic properties of pyrochlore-lattice compounds see Ref. [40].

I discussed the general physical properties of frustrated systems. This class of magnetic materials can be viewed as a separate class of magnets, distinct from e.g. ferromagnets, antiferromagnets, ferrimagnets, and metamagnets. The important elements that define this class are:

- (i) A low transition temperature compared to the Curie-Weiss constant.
- (ii) Shared microscopic properties of a triangle-based magnetic lattice and isotropic local symmetry and exchange interactions.

Most theoretical work on frustrated lattices has been done for Ising spin systems. But, only Heisenberg-type systems are likely to exhibit frustration effects. In the following chapters, I will consider Heisenberg systems with reduced dimensionality.

2 Experimental methods

2.1 General remarks on electron spin resonance

Electron paramagnetic resonance (EPR) or electron spin resonance (ESR) was first realized in Kazan State University (USSR) by Yevgeny Zavoisky in 1944 and has developed into a major scientific technique. EPR signals were detected in copper chloride (CuCl_2), copper sulfate (CuSO_4), manganese sulfate (MnSO_4), and in several other paramagnetic salts. Brebis Bleaney developed a similar technique independently at Oxford University at the same time.

ESR spectroscopy is a powerful method to study magnetic properties of materials. ESR measurements allow the precise probing of local spin properties, which are sensitively modified by factors in the outer environment, such as the crystal structure or neighboring magnetic interactions.

The following advantages of ESR measurements can be summarized:

- (a) High sensitivity. Small concentrations of paramagnetic species are sufficient to obtain ESR signals.
- (b) Detailed and highly accurate information is obtained about the nature of the paramagnetic species and its immediate surroundings.
- (c) Spin Hamiltonian parameters can be measured with high precision.
- (d) The spin-spin interaction between paramagnetic ions can be estimated.
- (f) Spin-lattice relaxation times can be estimated from the linewidth.

On the other hand we should admit some disadvantages of the ESR technique.

- (a) Often, resonances are observable only at low temperatures because of fast spin-lattice relaxations.
- (b) Resonances are limited usually to the ground-state levels.
- (c) Resonance transitions are not always allowed by selection rules.
- (d) Good-quality single crystals are often required.

The ESR phenomena is a resonance absorption of electromagnetic radiation by magnetic systems. Mostly, ESR experiments are carried out in the GHz frequency range. In this chapter, I briefly discuss the origin of ESR absorption and the optimal conditions to carry out experiments.

An electron has a magnetic moment and the spin quantum number $S = 1/2$, with possible spin projections $m_s = +1/2$ and $m_s = -1/2$. When an external

magnetic field with strength B_0 is applied, the electron's magnetic moment aligns either parallel ($m_s = -1/2$) or antiparallel ($m_s = +1/2$) to the field, each alignment having a certain energy $E = g\mu_B m_s B_0$ (Fig. 2.1a). This effect is known as the Zeeman effect (see Ref. [41] for example). The parallel alignment of the external magnetic field and the magnetic moment of the electron corresponds to the lower-energy state, and the separation between the states with antiparallel orientation is:

$$\Delta E = g\mu_B H_0, \quad (2.1)$$

where g is the electron's g -factor (or the Lande g -factor), H_0 is the external magnetic field, and μ_B is the Bohr magneton. This equation implies that the splitting of the energy levels is directly proportional to the magnetic-field strength, as shown in the Fig. 2.1a. I consider $g = 2.0023$ (free electron value) in the examples discussed in this section.

An unpaired electron can move between the two energy levels $m_s = -1/2$ and $m_s = +1/2$ by either absorbing or emitting electromagnetic radiation of energy $E = h\nu$. In combination with Eq. (2.1), this gives us the fundamental equation of ESR spectroscopy:

$$\Delta E = h\nu = g\mu_B H_0, \quad (2.2)$$

or

$$\omega_0 = \gamma H_0, \quad (2.3)$$

where h is the Planck constant, ν is the resonance frequency, $\omega_0 = 2\pi\nu$ is the angular frequency, and $\gamma = g\mu_B/2\pi h$ is the gyromagnetic ratio.

Electromagnetic radiation has both electric and magnetic field components, which oscillate in phase perpendicular to each other and perpendicular to the direction of energy propagation. The oscillating magnetic field induces transitions between the magnetic states with $m_s = -1/2$ and $m_s = +1/2$ with equal probability in either direction. The number of transitions per second is a function of the amplitude H_1 and the frequency ω of the oscillating field. The method for calculating this number is given by A. Abraham and B. Blini in their monograph [42]. The result is

$$w_{ij} = \frac{\pi H_1^2}{2\hbar^2} |\mu_{ij}|^2 f(\omega). \quad (2.4)$$

The shape function $f(\omega)$ is a function of ω describing the linewidth. It is assumed that the $f(\omega)$ has a wide spectrum, but the only significant contribution

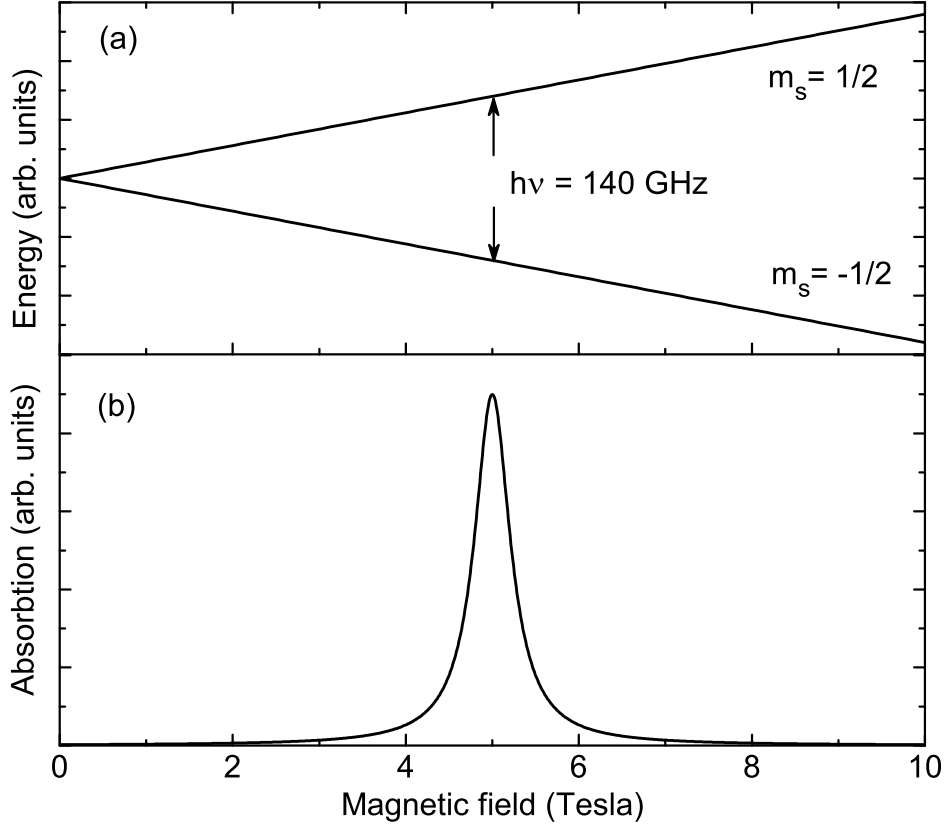


Figure 2.1: (a) Energy-level diagram and (b) absorption spectrum of the electron spin resonance for free electrons ($g = 2.0023$). The absorption has a Lorentzian shape.

to the integral comes from the region where $\omega \approx \omega_0$. The resonance frequency ω_0 given by Eq. (2.3). $f(\omega)$ is normalized as $\int_{-\infty}^{\infty} f(\omega)d\omega = 1$. Usually, Gaussian, Lorentzian, or combinations of these function are used as shape function. $|\mu_{ij}|^2$ is the square of the magnetic dipole matrix element between the states i and j . In the simple case of a pure spin state with full spin \mathbf{S} , we have $|\mu_{ij}|^2 = \langle m_s | \mathbf{S} | m_s \pm 1 \rangle$.

There will be an absorption of energy since the state at lower energy has a larger population, and the total number of transitions in either direction is

proportional to the population of the initial state. In experiment, we have to deal with samples which consist of a large number of paramagnetic centers ($10^6 - 10^{12}$ spins). In thermodynamic equilibrium, the population of spin-only energy levels is given by the Maxwell-Boltzmann distribution:

$$\frac{n_{1/2}}{n_{-1/2}} = \exp\left(-\frac{E_{1/2} - E_{-1/2}}{k_B T}\right) = \exp\left(-\frac{\Delta E}{k_B T}\right) = \exp\left(-\frac{h\nu}{k_B T}\right). \quad (2.5)$$

n_i is the population of the level with spin projection i . At a frequency of 140 GHz and temperature of 4.2 K (liquid-helium temperature), Eq. (2.5) gives $n_{1/2}/n_{-1/2} \simeq 0.202$. At 300 K (room temperature), we have $n_{1/2}/n_{-1/2} \simeq 0.978$. Thus, one can conclude that the intensity of the ESR absorption increases significantly with decreasing temperature. A possible ESR spectrum at 140 GHz is shown in Fig. 2.1b.

The net absorption of the energy per time interval (assuming no significant departure from thermal equilibrium) is

$$\frac{dW}{dt} = w_{ij}(\hbar\omega)(n_{-1/2} - n_{1/2}). \quad (2.6)$$

For simple doublets, the total number of ions is $n = n_i + n_j = n_i(1 + \exp(-\frac{h\nu}{k_B T}))$. In such a case, it follows from from Eqs. (2.4 and 2.5)

$$\frac{dW}{dt} = n \tanh\left(\frac{\hbar\omega}{2k_B T}\right) \frac{\pi\omega H_1^2}{2\hbar} |\mu_{ij}|^2 f(\omega). \quad (2.7)$$

Often in experiments $\hbar\omega/2k_B T \ll 1$ ($\hbar\omega/2k_B T = 1$ for $\nu = 10$ GHz at 0.48 K), so that $1 - \exp(-h\nu/k_B T) \approx -h\nu/k_B T$, and Eq. (2.7) reduces to

$$\frac{dW}{dt} = n \frac{\pi\omega^2 H_1^2}{2k_B T} |\mu_{ij}|^2 f(\omega). \quad (2.8)$$

Using above equations one is able to find optimal conditions for the experimental detection of ESR signals. The absorption intensity is increasing with frequency [Eq. (2.8)]. Concomitantly, the magnetic field usually has to increase as well [Eqs. (2.2) and (2.3)]. The magnetic field produced by conventional electromagnets is about 2 Tesla. The corresponding frequency is 42 GHz for $g = 2$. Superconducting magnets can produce fields up to about 20 Tesla. Such fields allow ESR experiments over a broad frequency range. The limited magnetic fields are not the only problem. The intensity of commonly used radiation sources decreases with frequency. Thus, the most useful frequency range for ESR experiments is 10 – 600 GHz. In the following, I will discuss the different techniques used for ESR experiments and will return to Eqs. (2.7) and (2.8) to estimate the sensitivity of different techniques.

2.2 Experimental techniques

ESR absorption can be observed by either varying the microwave frequency incident on a sample while holding the magnetic field constant or varying the field at constant frequency. In practice, it is usually the frequency that is kept fixed. The reasons for this is the limited sweepability of traditional microwave sources.

In this chapter, I will describe instrumentation details of the ESR experiments made in the framework of this thesis. In its general form, an ESR spectrometer consists of the four indispensable parts: a radiation source, a magnet, a radiation detector, and a probe. The principle scheme of an ESR spectrometer is shown in Fig 2.2.

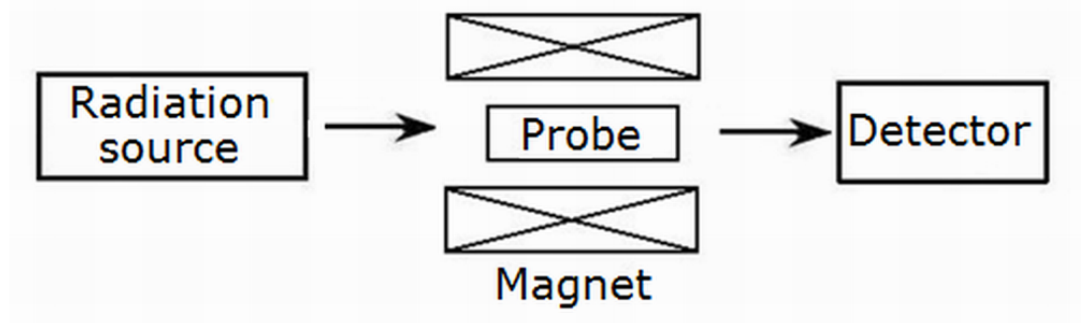


Figure 2.2: Scheme of an ESR spectrometer.

The probe with the sample is installed inside the magnet. Three types of magnets were used in the experiments described in this thesis. Magnetic fields up to 16 T were produced by a liquid-helium-cooled superconducting magnet. The used magnet has a vertical bore and high homogeneity of the magnetic field ($< 10^{-5}$ over 1 cm DSV (diameter spherical volume)). The designed sweeping rate is 0.7 T/min at low fields (0 – 7 T) and 0.5 T/min at high fields (7 – 16 T). For magnetic fields above 16 T pulsed-magnet coils were used. The electrical current through the pulsed coil is produced by discharging a capacitor bank. The strength of the magnetic fields depends on the applied energy and the design of the coil. The maximum available field at the Dresden High Magnetic Field Laboratory (HLD) is about 94 T (July 2012). The discussed ESR experiments were done at fields up to 51 T. The pulse duration is determined by the capacitance of the capacitor bank, the coil inductance, and a crow-bar resistivity. The typical pulse duration is about 0.1 s. The design of the coils is described in detail in Ref. [43]. Some experiments have been done using an X-band (9,4 GHz) Bruker spectrometer. This spectrometer is equipped with an electromagnet producing a maximal field of 2.1 T.

2 Experimental methods

Three types of radiation sources were used: Backward-wave oscillators (BWOs), VDI microwave sources (product of Virginia Diodes Inc.), and Gunn diodes. These sources are covering quasi-continuously the frequency range between 25 GHz and 1.4 THz. The VDI sources and Gunn diodes generate radiation with a good monochromaticity as well as frequency and power stability. These sources have a number of fixed frequencies. Using them in combination with multipliers, we are able to reach frequencies up to 448 GHz.

The frequency of radiation generated by BWOs is proportional to the square root of the applied cathode voltage. The exact function for the frequency calculation is provided by the manufacturer. The output power of the BWOs is a rather complex function of the cathode voltage, from ~ 80 mW in the low-frequency range (163-260 GHz) and to a few mW in the high-frequency range (above 1 THz). The output power of all radiation sources decreases with frequency (see Table 2.1 for details).

	Freq., GHz	Power, mW		Freq., GHz	Power, mW
BWO millimeter and submillimeter wave sources.					
OV 69	34-55	20		OV 32	233-547
OV 70	50-80	15		OV 81	490-859
OV 56	50-81	20		OV 80	524-694
OV 71	78-119	20		OV 83	682-1099
OV 86	113-178	40		OV 82	720-991
OV 87	117-177	30		OV 84	870-1229
OV 24	163-260	30		OV 85	1006-1422
OV 30	154-379	23			
VDI millimeter and submillimeter wave sources.					
	24-28	1460		192-224	26
	48-56	475		288-336	4
	96-112	115		384-448	3.2
Gunn diodes.					
	73.3	40		146.6	1.8
	85	52		219.9	1.8
	96	40		192	3.5

Table 2.1: Radiation sources, frequency ranges, and output power available at the HLD.

A hot-electron n-InSb bolometer was used as a detector to register the THz and sub-THz radiation power (product of QMC Instrument Ltd.). Such kind

of detectors have a high-sensitivity ($\sim 4 \text{ kV/W}$ at $\nu = 33 \text{ GHz}$) and fast response ($\sim 1 \mu\text{s}$). The detector is operated at liquid-helium temperature (4.2 K).

The frequency and the strength of the magnetic field should be measured with high accuracy. For the measurements at comparable low frequencies, a marker sample with well-known g -factor is used. The organic chemical compound 2,2-diphenyl-1-picrylhydrazyl (DPPH) is used as marker, usually. This compound has a very narrow absorption line (1.5 – 4.7 Gauss) and highly isotropic g -factor of 2.0036. The peak position of the DPPH's ESR signal at 200 GHz is 7.132 T. Thus, DPPH can be used as a field-marker up to 445 GHz in the spectrometers equipped with the 16-T superconducting magnet. The slight g -factor anisotropy of DPPH becomes detectable if the measurements are performed at high frequencies ($\nu > 200 \text{ GHz}$). In addition, the stability of the radiation sources reduces with increasing frequency. Therefore, an additional control of the frequency is very important for the experiments carried out at frequencies above 400 GHz. Such high frequencies were generated by BWO sources in the experiments described here. For calibration of the BWOs, the frequency of the radiation was measured as function of the cathode high voltage by a Fabry-Pérot interferometer (Fig. 2.3).

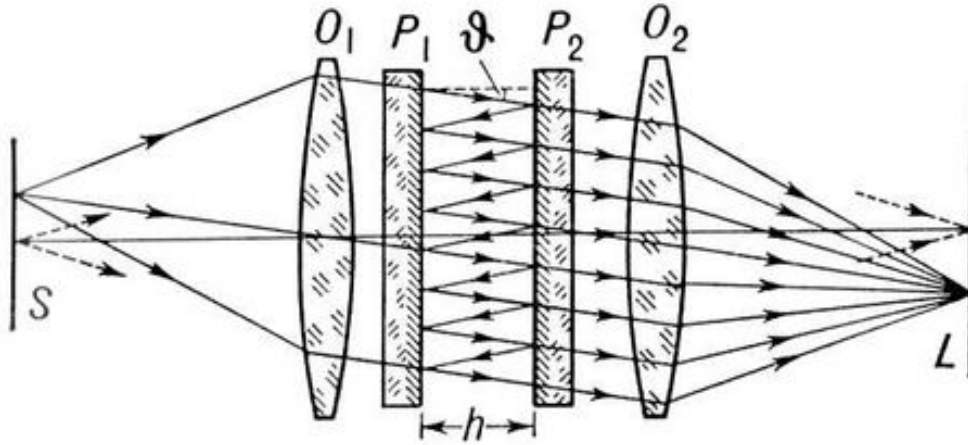


Figure 2.3: Schematic drawing of the Fabry-Pérot interferometer. S – radiation source, L – detector, O_i - lenses, P_i - partially reflective mirrors.

A Fabry-Pérot interferometer or etalon is typically made of a transparent plate with two reflecting surfaces, or two parallel highly reflecting mirrors. It is named after Charles Fabry and Alfred Pérot. Etalon is from the French word *étalon*, meaning measuring gauge or standard. A schematic drawing of the interferometer is shown in Fig. 2.3. Its transmission spectrum as a function of wavelength (λ)

exhibits peaks in the transmission corresponding to resonances of the etalon. The wavelength separation between adjacent transmission peaks is called the free spectral range of the etalon, and is given by:

$$\Delta\lambda = \frac{\lambda_0^2}{2nl \cos \theta + \lambda_0} \approx \frac{\lambda_0^2}{2nl \cos \theta}. \quad (2.9)$$

When the wavelength is fixed the intensity of the transmitted radiation is a function of the distance between the mirrors (h). The wavelength of the radiation can be determined by varying h and measuring the distance (Δh) between maxima in transmission.

Mostly, ESR experiments are carried out in the frequency range 10 - 200 GHz. This frequency range is experimentally very convenient, for a number of reasons: (a) A number of zero-field energy splittings lie in this range; (b) The linewidths in paramagnetic salts typically are in the range 0.1 to 10 GHz; (c) The cavity resonators and waveguide components are of easy handable size; (d) The magnetic fields corresponding to ESR at these frequencies can be obtained easily by superconducting or resistive magnets.

An important part of the spectrometer (2.2) is the probe. There are several possibilities to realize the coupling between the radiation and the sample and to detect the resonances. In the following, I will describe briefly the three methods:

- (i) microwave-cavity technique,
- (ii) transmission method, and
- (iii) the torque detection of ESR.

2.2.1 Microwave-cavity technique

An often used method in ESR spectroscopy is the perturbation-cavity technique. This method is very useful in experimental physics because of its high sensitivity. A schematic drawing of a microwave-cavity-based ESR spectrometer is shown in Fig. 2.4.

From Eqs. (2.7) and (2.8) one can see that the absorbed power increases with the square of the radiation-field amplitude H_1^2 . To make H_1^2 as large as possible, the sample is placed in a tuned circuit or microwave cavity. The microwave cavity is usually a closed metal structure that confines electromagnetic fields in the microwave spectral range. Such cavities act as resonant circuits with very low loss at their operation frequency. Two geometries are mostly used for microwave cavities, rectangular and cylindrical.

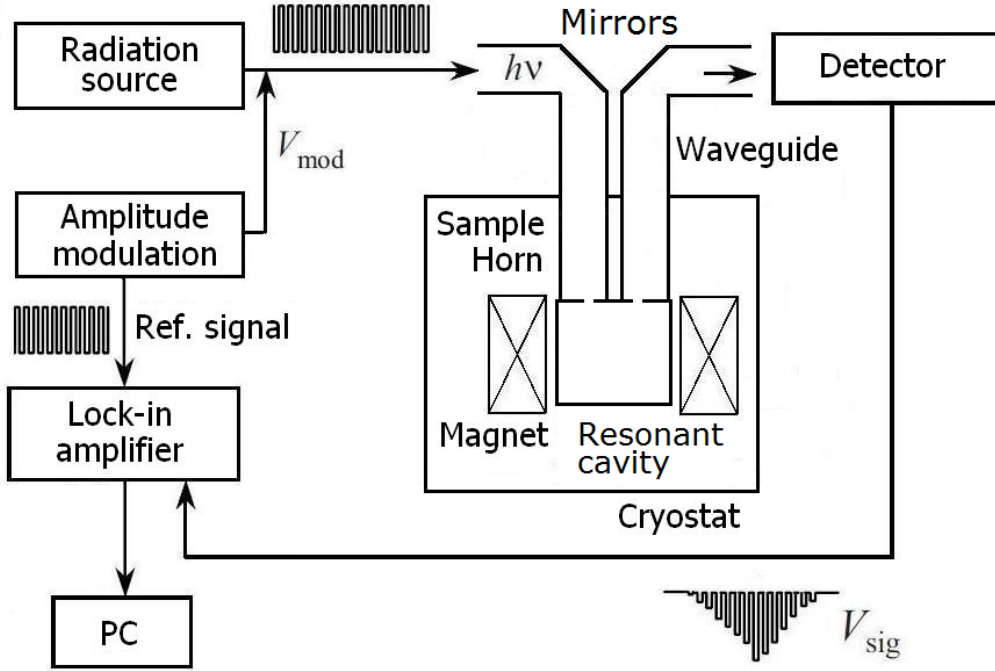


Figure 2.4: Scheme of an ESR spectrometer with resonant cavity.

Resonance frequencies of such microwave cavities can be found in literature [45]. The eigenfrequencies of the rectangular cavity are similar for TE_{mnl} and TM_{mnl} modes and given by

$$f_{mnl} = \frac{ck_{mnl}}{2\pi\sqrt{\mu_r\epsilon_r}} = \frac{c}{2\pi\sqrt{\mu_r\epsilon_r}} \sqrt{\left(\frac{m\pi}{a}\right)^2 + \left(\frac{n\pi}{b}\right)^2 + \left(\frac{l\pi}{d}\right)^2}, \quad (2.10)$$

where k_{mnl} is the wavenumber, c is the speed of light in vacuum, and μ_r and ϵ_r are the relative permeability and permittivity, respectively, a , b , and d are geometric parameters of the cavity.

The eigenfrequencies of the cylindrical cavity are given by

$$f_{mnp} = \frac{c}{2\pi\sqrt{\mu_r\epsilon_r}} \sqrt{\left(\frac{X_{mn}}{R}\right)^2 + \left(\frac{p\pi}{L}\right)^2}, \quad (2.11)$$

$$f_{mnp} = \frac{c}{2\pi\sqrt{\mu_r\epsilon_r}} \sqrt{\left(\frac{X'_{mn}}{R}\right)^2 + \left(\frac{p\pi}{L}\right)^2}, \quad (2.12)$$

where X_{mn} denotes the n -th zero of the m -th Bessel function, and X'_{mn} denotes the n -th zero of the derivative of the m -th Bessel function. L and R are the length and radius of the cavity, respectively. The Eqs. (2.11) and (2.12) correspond to TM and TE modes, respectively. In Fig. 2.5, a picture of a rectangular cavity is shown.

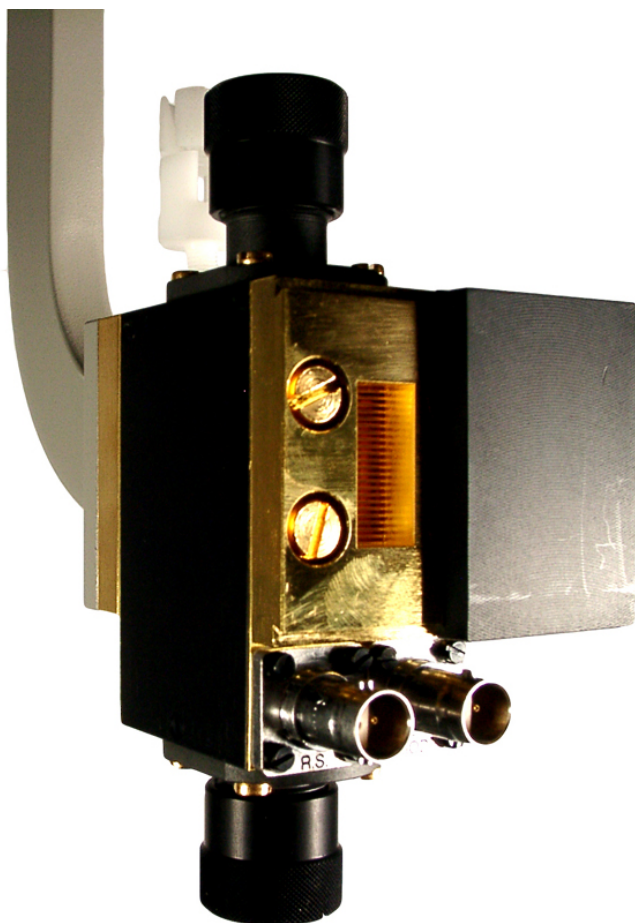


Figure 2.5: The ER 4102ST rectangular cavity has been the standard cavity for all Bruker EPR instruments over many years.

The Q -factor is a dimensionless parameter that describes how strong the damping of a resonator is or, equivalently, characterizes the resonator bandwidth relative to its center frequency. The Q -factor of microwave cavities can

approach several thousands. It usually consists of three parts, representing different mechanisms of power loss. First, Q_c is result the power loss in the walls of the cavity which have finite conductivity. Second, Q_d describes the power loss in the dielectric material filling the cavity. Third, Q_{ext} is the power loss through slits and holes of the cavity. This finally gives

$$Q = \left(\frac{1}{Q_c} + \frac{1}{Q_d} + \frac{1}{Q_{ext}} \right)^{-1}. \quad (2.13)$$

The detailed description of cavity constructions and other microwave elements (such as waveguides, splitters) can be found in Ref. [45].

Often, ESR experiments are performed in the frequency range of 10 - 35 GHz (with corresponding wavelength $\lambda \approx 1 - 3$ cm). Because of the easily accessible field range of about 2 T and the size of the microwave elements for this range, corresponding to the wavelength is very well handable. The most popular cavity-based ESR-spectrometer is based on a 3-cm generator ($\nu = 9.35$ GHz) as shown in Fig. 2.4.

The resonant-cavity method is the best one from a sensitivity point of view. But, we should point out also some disadvantages: (a) The eigenfrequency of the resonant cavity cannot be changed. Changing of the experimental frequency means a replacement of the microwave cavity. (b) It is hardly possible to use microwave cavities for experiments at frequencies above ≈ 200 GHz.

2.2.2 Transmission method

A block scheme of a transmission-type spectrometer is shown in Fig. 2.6. This is the most simple kind of ESR spectrometers. An experiment is carried out by transmitting radiation through the sample. The sample is located inside a waveguide. The radiation is focused on the sample by horns. Thus, all radiation received by the detector transmits through the sample.

The main advantages of transmission-type spectrometers are the tunability of the frequency and the possibility to use high frequencies. Measurements at high frequencies offer the following advantages:

- (i) the higher spectral resolution, which increases with frequency and external magnetic field. This is used e.g. to investigate the structure, polarity, and dynamics of radical microenvironments in spin-modified organic and biological systems through the spin label and probe method.
- (ii) The increase in orientation selectivity and sensitivity in the investigation of disordered systems.
- (iii) The accessibility of spin systems with large zero-field splitting due to

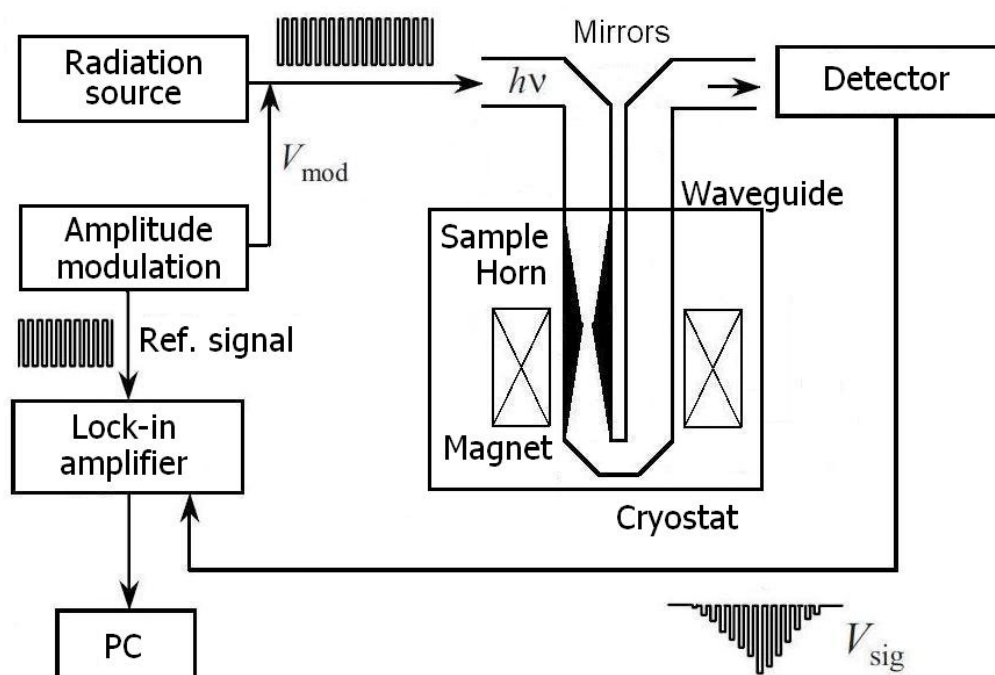


Figure 2.6: Schematic drawing of a transmission-type ESR spectrometer.

the larger microwave quantum energy $h\nu$.

(iv) The cross relaxation of paramagnetic centers decreases dramatically at high magnetic fields, making it easier to obtain more precise and more complete information about the system under study.

However, the transmission method has a relatively low spin sensitivity, compared to the cavity method. Quantitatively, the spin sensitivity of the transmission-type ESR is typically of the order of 10^{14} spin/G, which is five orders of magnitude reduced to that of a cavity-type spectrometer [46]. As a result, the transmission-type ESR experiments have been mainly applied to large-volume samples.

2.2.3 Torque detection of ESR

The limitations of the application of the perturbation-cavity technique described in the previous section motivated scientists to develop an alternative method to measure high-frequency ESR spectra. One possibility is the magnetic detection of ESR absorption. The ESR signal is detected as a change of the mag-

netization associated with the transition between the Zeeman levels. In conventional ESR, the signals are detected by measuring the absorbed power of the electromagnetic wave. It should be noted here that for the case $S = 1/2$, the ESR absorption is also accompanied by a spin reversal since the selection rule $\Delta S_z = 1$ has to be satisfied. Therefore, the magnetization of the system also changes, indicating that ESR transitions can be detected as a change in the magnetization, ΔM , and, thereby, as a change in the magnetic torque, τ . The magnetic torque, $\tau = \mathbf{M} \times \mathbf{H}$, forces the sample magnetization to align along the magnetic-field direction. This is the basic idea of the torque method. Cantilever magnetometers are known as a highly sensitive technique to measure small changes in the magnetic moment. In the following, this method is discussed in more detail.

When a sample containing unpaired electron spins is placed in a magnetic field, there is a net magnetization, M_0 , along the field direction. The magnetization is given by

$$M_0 = n\mu_B \frac{1}{2} \tanh\left(\frac{g\mu_B H}{2k_B T}\right), \quad (2.14)$$

where n is the spin density. In case $\mu_B H \ll k_B T$, the magnetization increases approximately linearly with magnetic field and can be approximated by

$$M_0 \approx \frac{ng\mu_B^2 H}{4k_B T}. \quad (2.15)$$

The resultant magnetic torque is given by

$$|\tau| \propto \Delta g \mu_B H^2 \sin 2\Theta, \quad (2.16)$$

when the sample is rotating in a plane containing two principle axes. Θ is the angle between the external magnetic field and one of the principle axes, Δg is the difference between the g -factors along respective directions. Thus, a magnetic anisotropy is necessary for the torque measurements.

When an oscillating magnetic field of amplitude H_1 and angular frequency ω is applied in the direction perpendicular to \mathbf{H} , the magnetization along \mathbf{H} is given by the Bloch equations as

$$M_z = M_0 \left[\frac{1 + (\omega_0 - \omega)^2 T_2^2}{1 + (\omega_0 - \omega)^2 T_2^2 + \gamma^2 H_1^2 T_1^2 T_2^2} \right], \quad (2.17)$$

where T_1 and T_2 are the longitudinal and transverse relaxation times, respectively, and ω_0 is the magnetic resonance frequency, given by Eq. (2.3). If the resonance condition is satisfied ($\omega = \omega_0$), the magnetization is

$$\delta M_z = M_0 \frac{1}{1 + \gamma^2 H_1^2 T_1^2 T_2^2}. \quad (2.18)$$

If $\gamma^2 H_1^2 T_1^2 T_2^2$ is large compared to unity and T_1 is less than the period of the cantilever resonance, then, in principle, a modulation technique can be used for measuring the change of the magnetization.

In contrast to the cavity method, this method can be extended to the high-frequency region without limitations. First ESR measurements by this method were done using very sensitive microcantilevers [47, 48]. However, microcantilevers require very small samples (not longer than $100 \mu\text{m}$) and are very delicate to use.

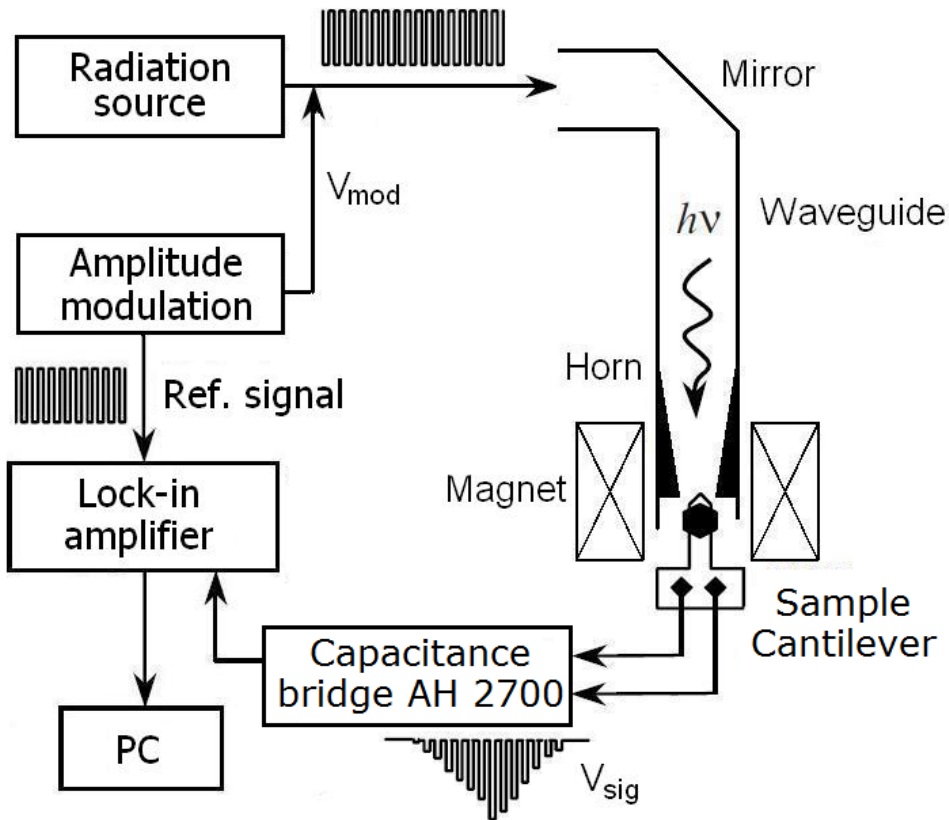


Figure 2.7: Schematic drawing of the cantilever-based ESR spectrometer.

We used instead a capacitive copper-beryllium cantilever in our test experiments. The principle scheme of the cantilever-based spectrometer is shown in Fig. 2.7. Tuneable-frequency VDI radiation sources were used. An amplitude modulation (20-400 Hz) was realized by using a mechanical chopper. A capacitance bridge (AH-2700) is a very important part of spectrometer because small changes in capacitance must be detected.

The copper-beryllium cantilever is one plate of a capacitor and mounted above a fixed copper plate as the other electrode of the capacitor (Fig. 2.8). A sample is fixed on top of the copper-beryllium plate. The external magnetic field is applied perpendicular to the plates. The microwave radiation is applied to the sample position by an oversized waveguide (10 mm stainless-steel tube). The radiation is focused by a horn to the sample. The k vector of the radiation is parallel to the external magnetic field.

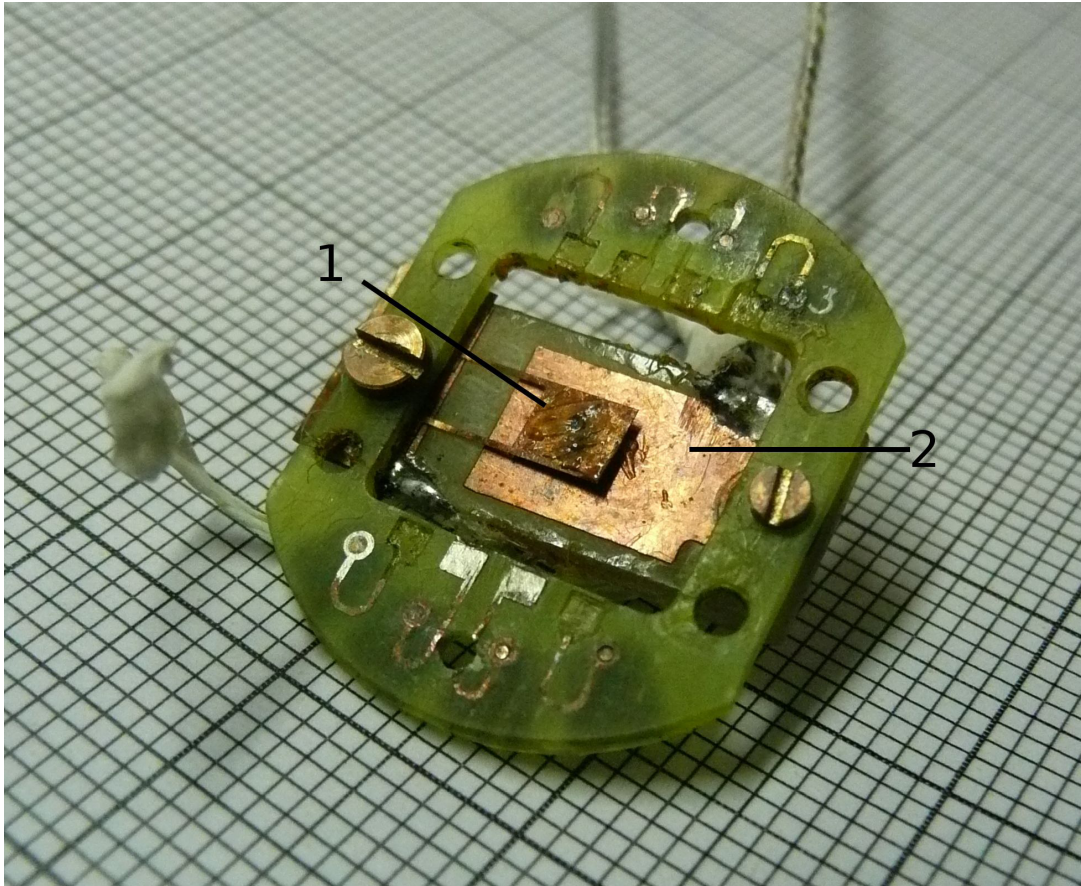


Figure 2.8: Sample holder of the cantilever-based ESR spectrometer. 1 – copper beryllium cantilever. 2 – fixed copper plate.

The test experiments were done using a concentrated magnetic salt, namely hydrated copper sulfate $\text{CuSO}_4 \cdot 5\text{H}_2\text{O}$. This compound was studied in detail in the middle of the twentieth century [49]. The available large sample sizes, the large ESR absorption, the axial anisotropy of the g -factor ($g_{\parallel} = 2.05, g_{\perp} = 2.4$), and the quite useful linewidth (~ 0.2 Tesla) motivated us to use this compound for our test experiments.

First spectra were obtained without amplitude modulation of the radiation. The results are shown in Fig. 2.9. The ESR signal was obtained by subtraction of the torque curve measured without radiation from the curve obtained in presence of the radiation.

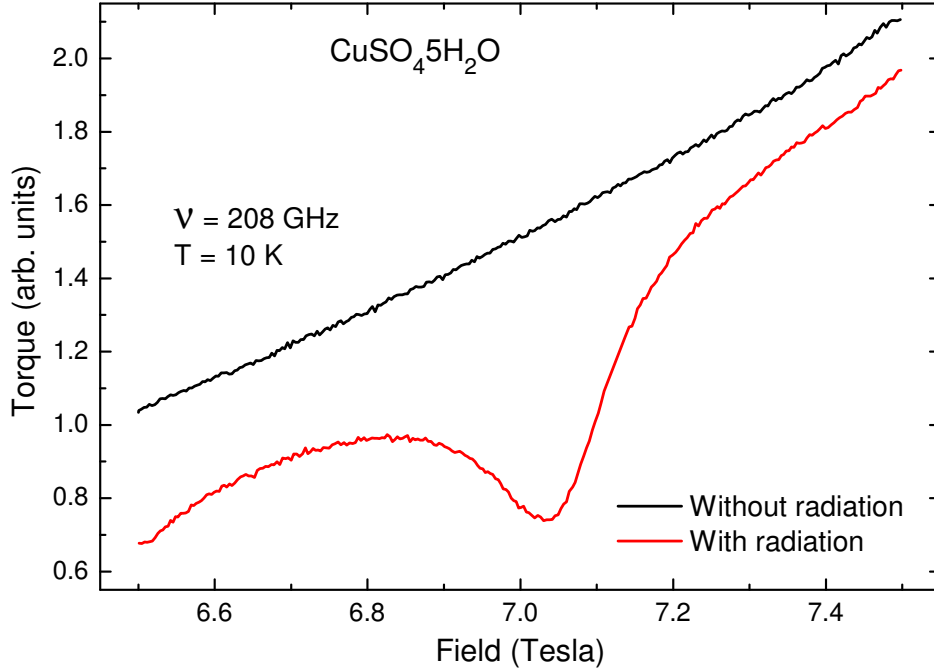


Figure 2.9: Torque signal of $\text{CuSO}_4 \cdot 5\text{H}_2\text{O}$ as function of external magnetic field. The minimum of the detected signals corresponds to a broad ESR absorption.

We increased the sensitivity of our spectrometer by using an amplitude modulation of the microwave radiation. The eigenfrequency of the cantilever ν is roughly 50 Hz for a 50 mg sample mass. The modulation frequency should differ enough from this eigenfrequency to avoid non-linear effects. The modulation was realized by a chopper in the frequency range: 20-300 Hz. An example of the spectrum obtained by this technique is shown in Fig. 2.10.

We observed two absorption lines at a radiation frequency of 211 GHz. There are two inequivalent positions of Cu^{2+} ions in the crystallographic structure. The g -tensors of these ions are equivalent, but their axes have different orientations. This causes the two lines in the ESR spectrum. The fit of the ob-

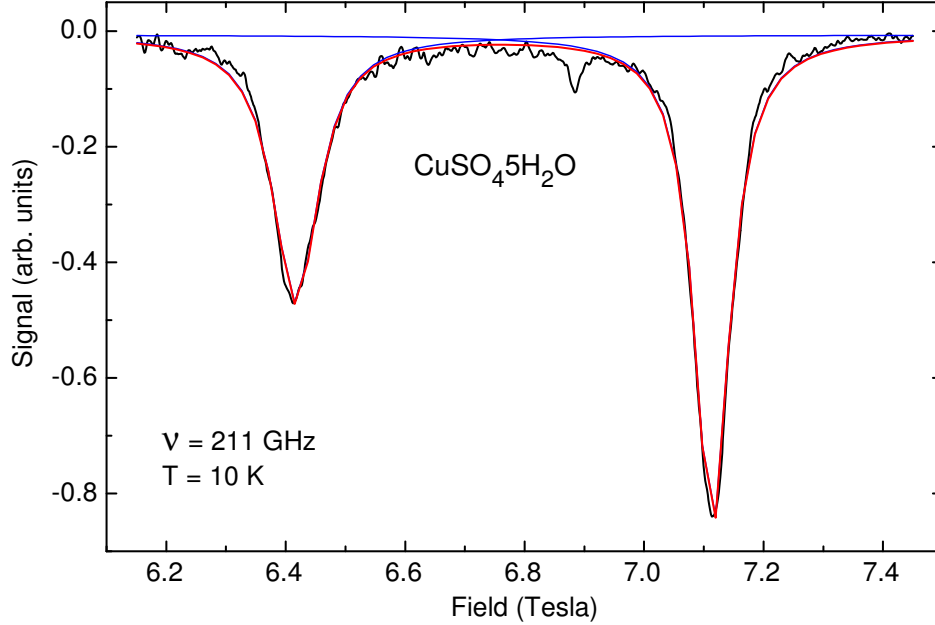


Figure 2.10: ESR spectrum of $\text{CuSO}_4 \cdot 5\text{H}_2\text{O}$ at $\nu = 211$ GHz, $T = 10$ K. The red line is a fit by the sum of two Lorentzian curves (the single Lorentzian lines are shown by the blue curves).

tained spectrum by two Lorentzian lines is shown by the red line in Fig. 2.10. The single Lorentzian lines are shown by blue curves. We determined the g -factors of these lines to 2.11 and 2.35. This results are in good agreement with a data available in literature [49, 50].

The resolution of our device is an order of magnitude lower than the transmission method. Anyway, the resolution is sufficient to detect the ESR signal. The development of the cantilever-based technique is further described in the diploma thesis of André Dankert [51].

To summarize, a new probe for high-field and high-frequency torque-detected ESR spectroscopy was designed and constructed. The probe works in combination with a superconducting 16 Tesla magnet and VDI radiation sources covering the frequency range from 50 up to 400 GHz. The ESR signal can be detected by measuring the capacitance of a cantilever, allowing to work with samples between several μg up to the mg range. The high sensitivity of the spectrometer

2 *Experimental methods*

was demonstrated using the Cu-based inorganic salt $\text{CuSO}_4 \cdot 5\text{H}_2\text{O}$ with a relatively low g -factor anisotropy.

3 ESR studies of the quantum spin-dimer system $\text{Ba}_3\text{Cr}_2\text{O}_8$

3.1 Introduction

Field-induced phase transitions in quantum magnets have recently received a considerable amount of attention, particularly in the context of quantum criticality. Quantum magnets have provided a number of new exotic collective phenomena [3]. A system of coupled spin dimers is an example of a quantum magnet. The field-induced evolution of the ground state was studied in a number of spin-dimer systems with a large diversity of magnetic structures, ranging from the simple weakly isolated isotropic spin dimers TlCuCl_3 [52, 53] to the highly frustrated quasi-two-dimensional network of strongly interacting dimers in $\text{SrCu}_2(\text{BO}_3)_2$ [54, 55]. In some cases, such field-induced phase transitions can be effectively described in terms of Bose-Einstein condensation of magnons [53, 56–58].

In this chapter, I focus on the magnetic properties of the $S = 1/2$ weakly coupled spin-dimer system $\text{Ba}_3\text{Cr}_2\text{O}_8$. This material belongs to a new class of compounds with the general formula $A_3B_2O_8$, where A is an earth-alkali metal and B is a $3d$ transition-metal ion with valence $5+$. $\text{Ba}_3\text{Cr}_2\text{O}_8$ has magnetic Cr^{5+} ions ($3d^1$, $s = 1/2$). At room temperature, this compound crystallizes in the rhombohedral $R\bar{3}m$ space group with lattice parameters $a = 5.73906(5)$ Å, $c = 21.3757(2)$ Å. At $T \simeq 70$ K, $\text{Ba}_3\text{Cr}_2\text{O}_8$ undergoes a structural phase transition due to the cooperative Jahn-Teller effect. This effect is induced by the orbital degeneracy of the Cr^{5+} ($3d^1$) ion. The phase transition is accompanied by the lowering of the symmetry from rhombohedral $R\bar{3}m$ to monoclinic $C2/c$ [59].

The magnetic structure of $\text{Ba}_3\text{Cr}_2\text{O}_8$ is shown schematically in Fig. 3.1. The Cr^{5+} ions are coordinated tetrahedrally. These ions form dimers along the crystallographic c axis which in turn are coupled into a triangular lattice in the ab plane. The distance between the Cr^{5+} ions in the dimers is $d = 3.934(6)$ Å at room temperature [60]. The intradimer magnetic interaction is antiferromagnetic and geometrically frustrated. The values of the exchange

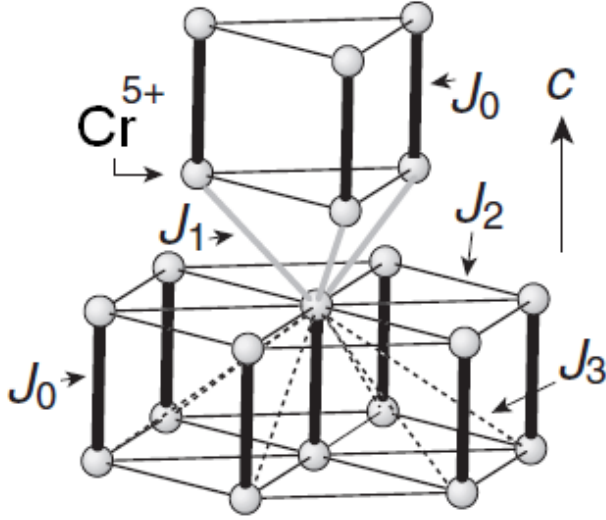


Figure 3.1: Network of the Cr^{5+} ions in the crystal structure of $\text{Ba}_3\text{Cr}_2\text{O}_8$. The first, second, third, and fourth nearest-neighbor exchange interactions J_0 , J_1 , J_2 , and J_3 are expressed as thick, gray, thin, and dashed lines, respectively. From Ref. [60].

intra- and inter-dimer interactions are known from magnetic-susceptibility experiments: $J_0 \simeq 27.6$ K, $J' \simeq 7.7$ K [60].

Recently, the magnetic properties of $\text{Ba}_3\text{Cr}_2\text{O}_8$ have been studied by means of magnetization, magnetocaloric effect [61], specific heat [58, 62], and elastic and inelastic neutron scattering [59]. Since the inter-dimer exchange interactions are strongly frustrated, $\text{Ba}_3\text{Cr}_2\text{O}_8$ does not exhibit any long-range ordering down to 0.3 K without external magnetic field.

The temperature-field phase diagram is shown in Fig. 3.2. Two critical fields, $H_{c1} \simeq 12.5$ T and $H_{c2} \simeq 23.6$ T for $T \rightarrow 0$, have been extracted for $\text{Ba}_3\text{Cr}_2\text{O}_8$ with a maximal transition temperature $T_c \simeq 2.7$ K at $H \simeq 18$ T (see Fig. 3.2). In this region, the system has a long-range antiferromagnetically ordered state [61].

Inelastic neutron-scattering measurements revealed a complex excitation spectrum, which cannot be explained solely based on the simplest model of weakly interacting dimers. The excitation spectrum exhibits three excitation modes with pronounced dispersions. Figure 3.3 shows the dispersions along three high symmetry directions. Along the $(0, 0, l)$ direction, a weakly dispersive excitation mode centered at about 2 meV is observed with a bandwidth

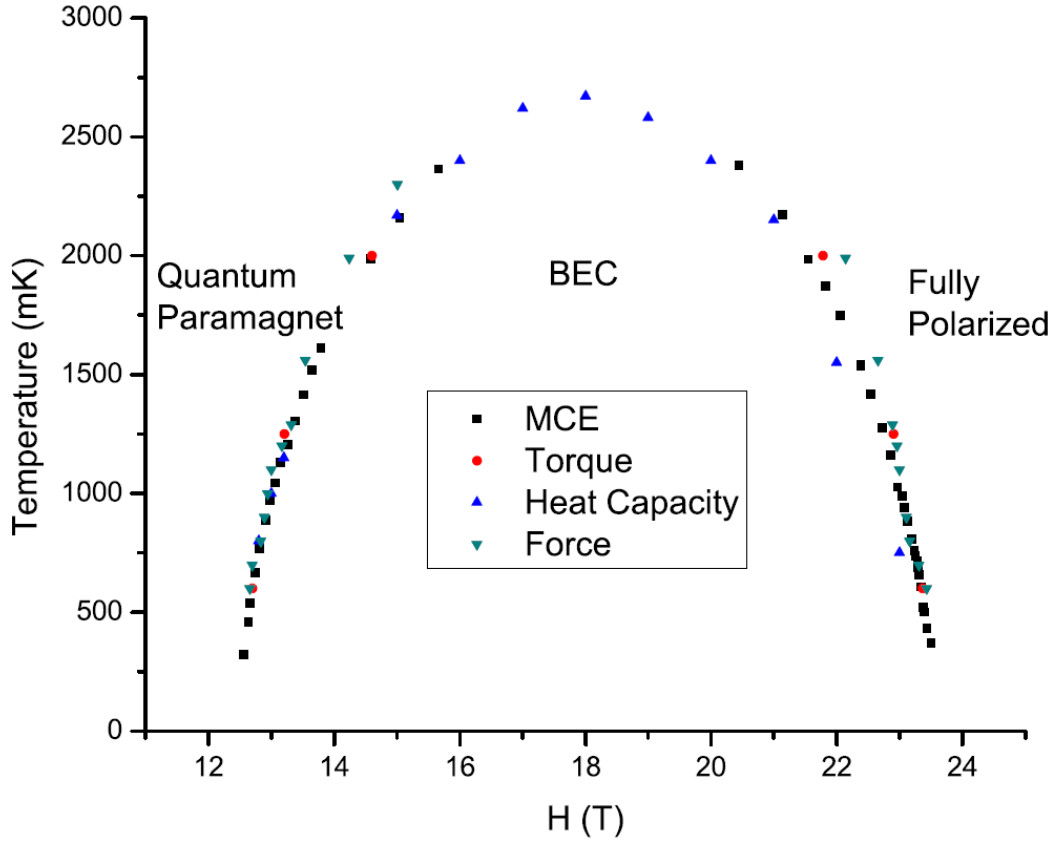


Figure 3.2: The temperature-field phase diagram of $\text{Ba}_3\text{Cr}_2\text{O}_8$ for $H \parallel c$. (From Ref. [61].)

of $\simeq 0.7$ meV (Fig. 3.3a). The excitation spectrum was described assuming spatially anisotropic interdimer interactions in three crystal domains formed in $\text{Ba}_3\text{Cr}_2\text{O}_8$ as a result of the structural phase transition at $T \simeq 70$ K. This dispersion is due to the weak interdimer interaction J_1 between the dimer planes (see Fig. 3.1). The dispersions along the $(h, h, 3)$ and $(h, h, 3h)$ directions, which probe the intraplane interdimer interactions, J_2, J_3 , as well as the out-of-plane ones, show three excitation modes (see Figs. 3.3b and 3.3c).

Analysis of the dispersions shows that this compound is an excellent model system for three-dimensional weakly coupled dimers with dominant intradimer coupling $J_0 = 2.38$ meV (27.6 K) and weak averaged interdimer coupling $J' \leq 0.52(2)$ meV (6 K).

Previously, ESR studies of $\text{Ba}_3\text{Cr}_2\text{O}_8$ have been performed in the frequency range from 70 to 380 GHz in magnetic fields up to 13 T [62]. Three ESR modes were observed for $H \perp c$: two gapped modes and one gapless mode.

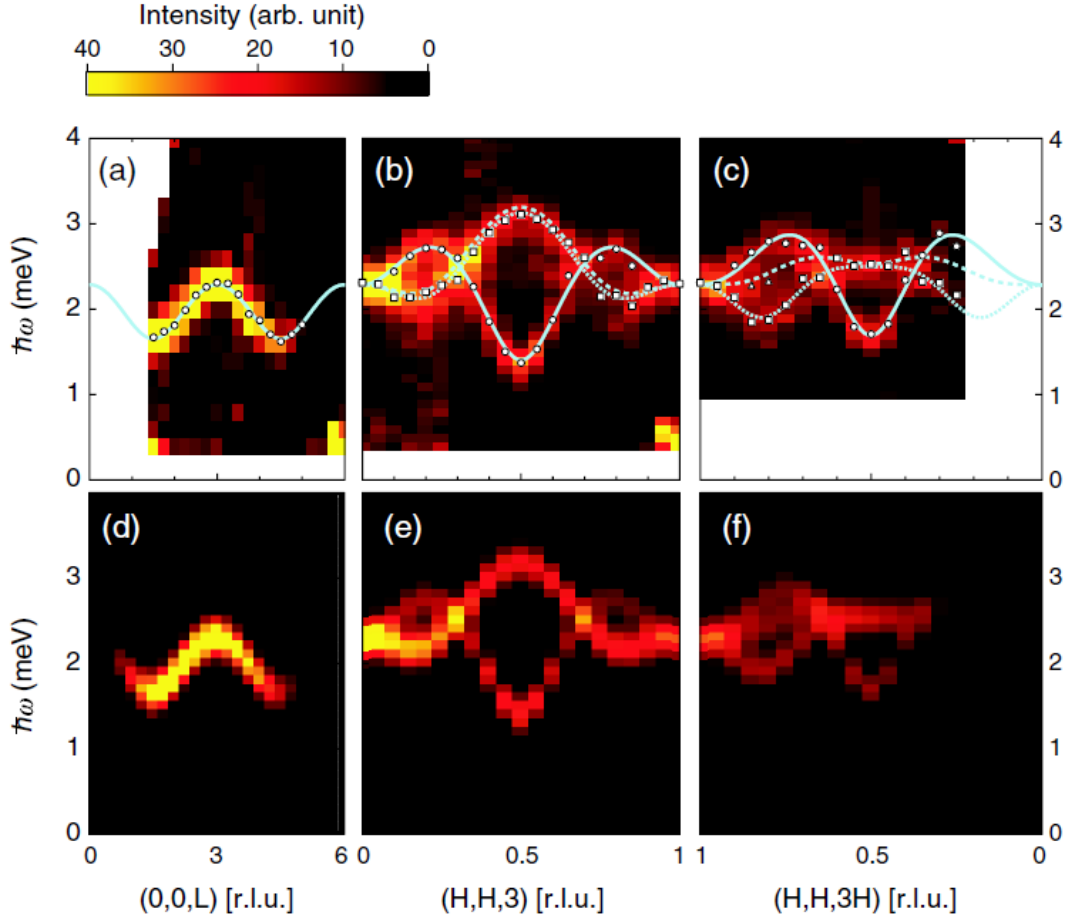


Figure 3.3: Contour maps of dispersion relations in $Ba_3Cr_2O_8$ along (a) $(0, 0, l)$, (b) $(h, h, 3)$, and (c) $(h, h, 3h)$. The data were taken by performing constant \mathbf{Q} scans at 1.7 K. The circles represent the peak positions obtained by fitting the data with simple Gaussians. (d), (e), and (f) Calculated dispersions and intensities based on a model of spatially anisotropic interdimer interactions. From Ref. [59].

The gap values $\Delta_{AB} = 546$ GHz (2.26 meV) and $\Delta_{CD} = 406$ GHz (1.62 meV) were determined by extrapolating the frequency-field dependence of these modes to zero field. These gap values are in good agreement with the results of inelastic neutron-scattering (Fig. 3.3a). The slope is the same for all modes and corresponds to $g = 1.94$ ($H \perp c$). Noticeably, the observation of gapped modes suggest the presence of intra-dimer DM interaction in this compound. The value of the DM interaction can be estimated by Eq. (1.8), to $|\vec{D}| \approx J_0 \cdot \Delta g / g \approx 0.9$ K.

In this chapter, I report systematic studies of the magnetic excitation spectrum of $\text{Ba}_3\text{Cr}_2\text{O}_8$ by tunable-frequency ESR spectroscopy in extended frequency (50 – 700 GHz) and magnetic field (up to 25 T) ranges. The two gaps, $\Delta_{AB} = 563 \pm 1$ GHz and $\Delta_{CD} = 399 \pm 1$ GHz, were observed directly as well. Peculiarities of the microwave absorption spectra in magnetic fields above H_{c1} are discussed.

3.2 Experimental details

Single crystalline $\text{Ba}_3\text{Cr}_2\text{O}_8$ samples with typical size of $4 \times 2 \times 0.2$ mm³ were investigated. Crystals have been grown by the traveling solvent floating zone method [63]. ESR experiments have been performed by using tunable-frequency transmission-type spectrometers operating in combination with a 16 T superconducting magnet at the Dresden High Magnetic Field Laboratory [64], and a 25 T resistive magnet at the National High Magnetic Field Laboratory in Tallahassee [46] (Florida, USA). The magnetic field was applied along the c axis. BWOs and VDI microwave sources were used as tunable sources of sub-THz radiation. The ESR measurements at the National High Magnetic Field Laboratory in Tallahassee were done with the marker sample 2,2-diphenyl-1-picrylhydrazyl (DPPH) with $g = 2.0036$. The measurements were performed at 1.4 K, which is well below the maximal transition temperature $T_c \simeq 2.7$ K (see Fig. 3.2).

3.3 Results and discussion

Figure 3.4 shows ESR spectra for the frequencies 312 and 514 GHz obtained using the 16 T magnet at 1.4 K and $H \parallel c$. There are three absorption peaks for magnetic fields below H_{c1} at 312 GHz. Two of them are quite intensive (peaks E and B in Fig. 3.4a) and one is very weak (peak D). When the radiation frequency increases, the resonance field of mode E increases as well. The magnetic-field dependence of the modes B and D is different from that of mode E. The resonance fields of these modes decrease with increasing frequency. It is important to note, that the mode B* observed at frequency 514 GHz (Fig. 3.4b) is an artifact. There is an additional high-frequency harmonic generated by the multiplier which was used for this measurement in combination with the radiation source. This harmonic causes this line.

ESR spectra obtained at 180, 295, and 436 GHz in magnetic fields up to 25 T in Tallahassee are shown in Fig. 3.5. The modes B, C, D, and E have been observed in magnetic fields below $H_{c1} = 12.5$ T. The very narrow line in field

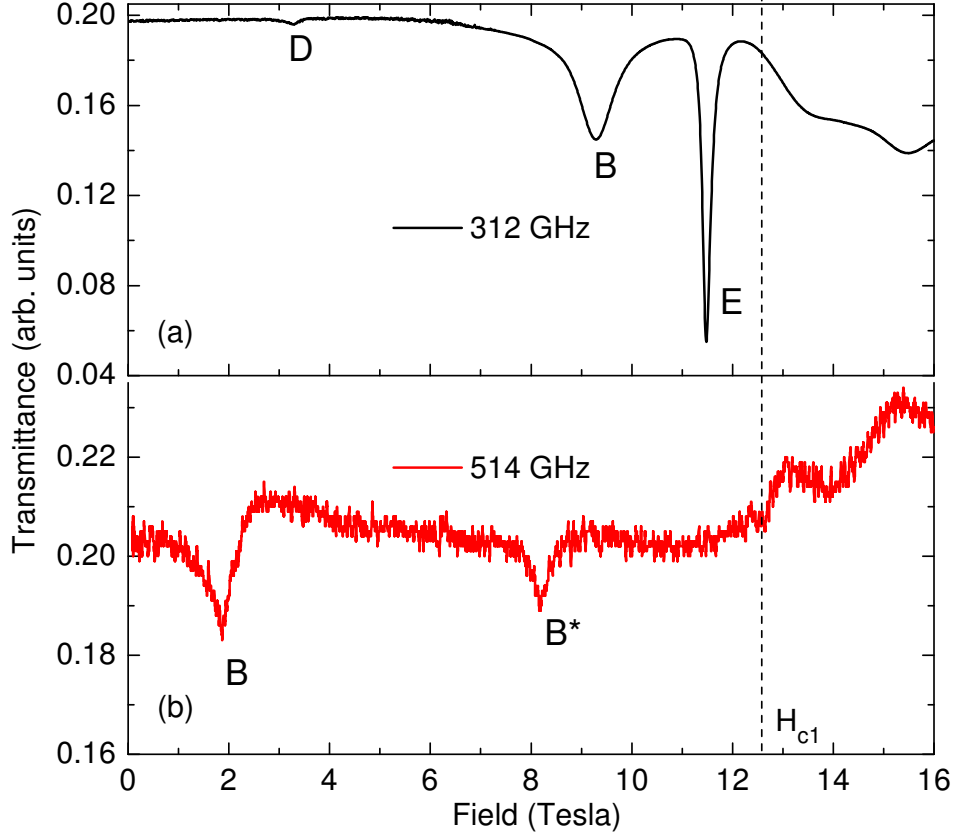


Figure 3.4: ESR absorption spectra of $Ba_3Cr_2O_8$ measured at the frequencies (a) 312 GHz and (b) 514 GHz at $T = 1.4$ K and $H \parallel c$. The dashed line indicates H_{c1} .

slightly below the mode E corresponds to the field marker DPPH (see subsection 2.2 for details). At magnetic fields above H_{c1} , the spectra show quite a complex structure. Later, I will discuss possible reasons for such a behavior.

The frequency-field dependence of the observed ESR modes is shown in Fig. 3.6. Two sets of ESR excitations with the gaps, $\Delta_{AB} = 563 \pm 1$ GHz (A and B modes) and $\Delta_{CD} = 399 \pm 1$ GHz (C and D modes), have been observed and studied in magnetic fields below H_{c1} in a broad range of frequencies. In addition, one gapless mode, E, was observed not only below H_{c1} but also above. The slope of the mode E is the same as the slopes of A, B, C, and D and

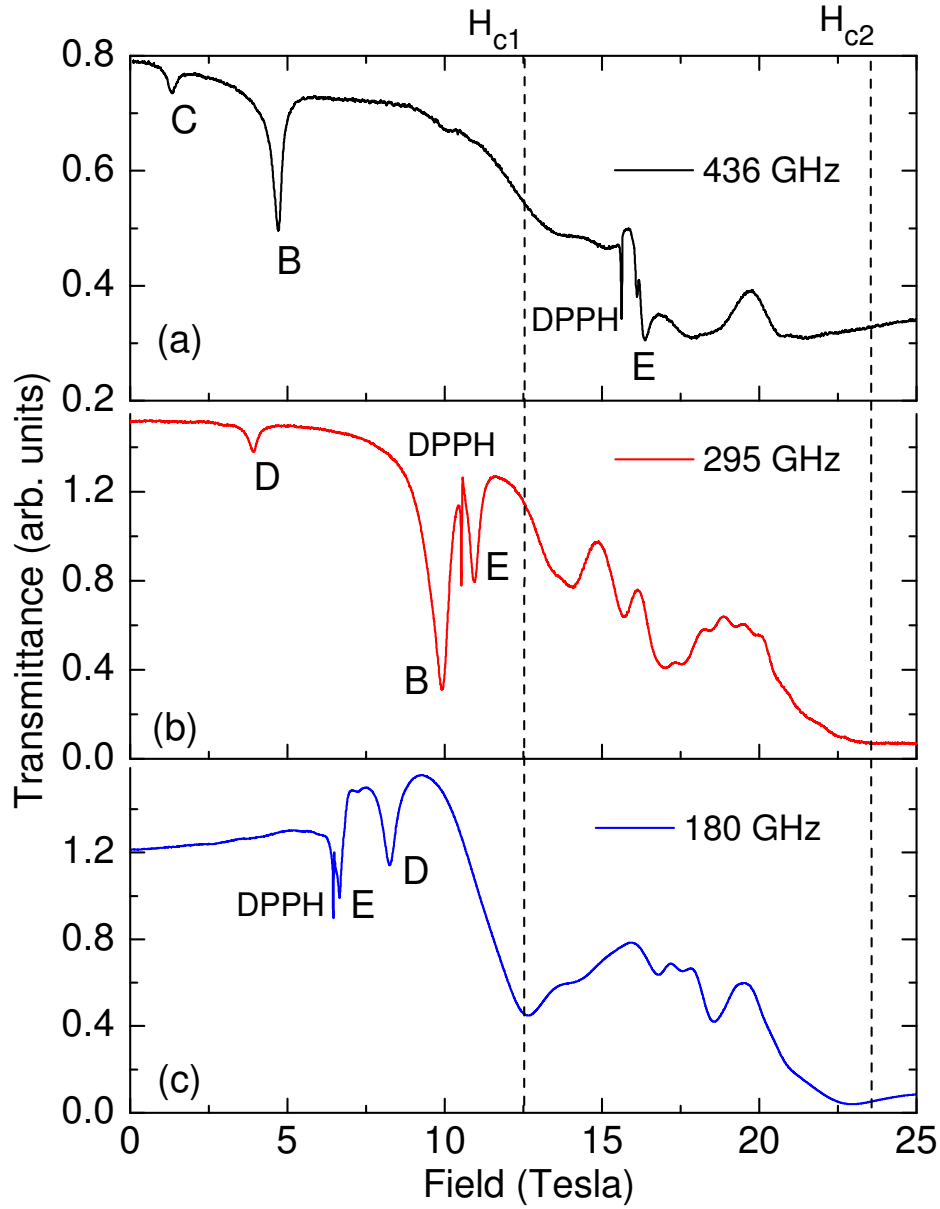


Figure 3.5: ESR absorption spectra of $\text{Ba}_3\text{Cr}_2\text{O}_8$ measured at the frequencies (a) 436 GHz, (b) 295 GHz, and (c) 180 GHz at $T = 1.4$ K and $H \parallel c$. Dashed lines indicate H_{c1} and H_{c2} .

corresponds to $g = 1.94$. This is a typical g -factor for the Cr^{5+} ion in a crystal field. These findings are in agreement with previous investigations [62].

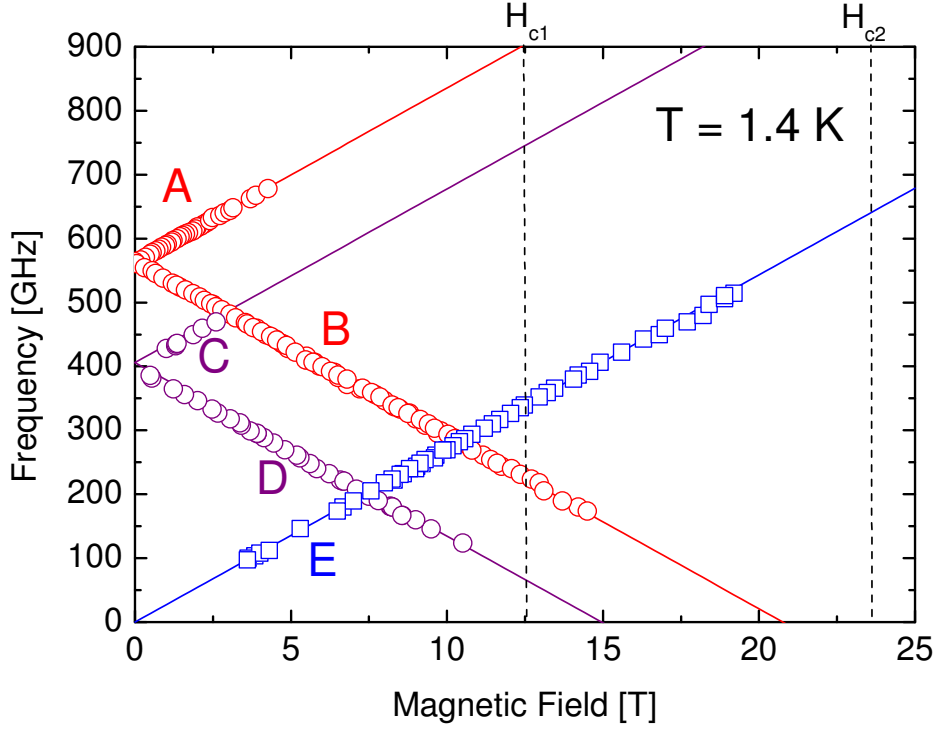


Figure 3.6: Frequency-field dependence of the ESR signal for $Ba_3Cr_2O_8$ at $T = 1.4$ K and $H \parallel c$. Solid lines are result of the fits (see text for details). Dashed lines indicate H_{c1} and H_{c2} .

I consider in detail the spin system to understand the obtained results. The spin-dimer system consists of two ions with spin s which are coupled by exchange interaction. For $s = 1/2$ ions, the maximal total spin S of such system is 1. There are two possible states for such a spin-dimer system, a spin-singlet state ($S = 0$) and a spin-triplet state ($S = 1$). The $S = 0$ state corresponds to antiparallel orientation of the spins in the dimer, the $S = 1$ state corresponds to parallel alignment of the spins. In case of antiferromagnetic exchange interaction between the spins, the singlet state ($S = 0$) is the ground state. Additionally, the $S = 1$ state has three possible spin-projections $S_z = -1, 0$, and 1 (see Fig 3.7a). Here, we introduce $|S, S_z\rangle$ as the

wave function with total spin S and spin projection S_z . As is well known, the transitions from the $|S, S_z\rangle = |0, 0\rangle$ ground state to the excited states $|S, S_z\rangle = |1, 0\rangle$, $|S, S_z\rangle = |1, 1\rangle$, and $|S, S_z\rangle = |1, -1\rangle$ are normally forbidden because of the conservation law for the total spin quantum number S [65] (these transitions are shown with red arrows in Fig. 3.7a). However, a non-secular term such as DM interactions or non-equivalent g -tensors can mix wave functions of the singlet ground state and triplet excited state. Thus, $|\psi\rangle_G = (1-f)|0, 0\rangle + f|1, 0\rangle$, where f is a mixing coefficient. This effect makes the observation of ESR transitions between singlet and triplet states possible. The expected frequency-field dependence of such transitions is shown in Fig. 3.7b. Evidently, we are able to observe transitions from $|0, 0\rangle$ to $|1, -1\rangle$ (mode B) and from $|0, 0\rangle$ to $|1, 1\rangle$ (mode A). Since the energy of the transitions from $|0, 0\rangle$ to $|1, 0\rangle$ does not change with magnetic field this mode cannot be observed in ESR experiments (silent mode).

If I introduce now inter-dimer coupling, the dispersion curve, $E(k)$, will deviate from linear behavior. This magnetic-excitation dispersion can be well explained within the random phase approximation giving [66]:

$$h\nu(k) = \sqrt{J_0^2 + J_0\gamma(k)}, \quad (3.1)$$

where $\gamma(k) = \sum J(R_i)e^{-ikR_i}$ and $J(R_i)$ represents the interdimer interactions. Kofu *et al.* performed calculations of the dispersion curves for $\text{Ba}_3\text{Cr}_2\text{O}_8$ shown in Fig 3.8.

In accordance with neutron-scattering results, the modes A and B correspond to excitations in the center of the Brillouin zone, at $k = 0$. These excitations are shown by the red arrow in Fig. 3.8. The modes C and D correspond to transitions at $k = \pi/c$ (shown by the violet arrow). It is noticeable that the observation of the excitations at $k = \pi/c$ should not be visible by means of ESR because of the conservation of energy. The observation of such excitations becomes possible in case of Brillouin-zone folding. We observed transitions between the singlet ground state ($S = 0$) and the excited triplet states ($S = 1$) (modes A, B, C, and D in Fig. 3.6). Very detailed investigations of the frequency-field dependence of these transitions allowed us to extract highly accurate values of the gaps, namely $\Delta_{AB} = 563 \pm 1$ GHz (27.0 K) and $\Delta_{CD} = 399 \pm 1$ GHz (19.1 K). These gap values are consistent with the dispersion curves obtained by means of inelastic neutron scattering (Fig. 3.3 and Ref. [59]). Transitions between singlet and triplet states have been also found in other systems of coupled spin dimers, for instance in $\text{SrCu}_2(\text{BO}_3)_2$ [54, 55] and KCuCl_3 [67].

The extrapolation of the modes D and B to zero frequency gives $H_{c1}^* = 14.7$ T and $H_{c2}^* = 20.7$ T (Fig. 3.6). These values obtained at 1.4 K are shifted from

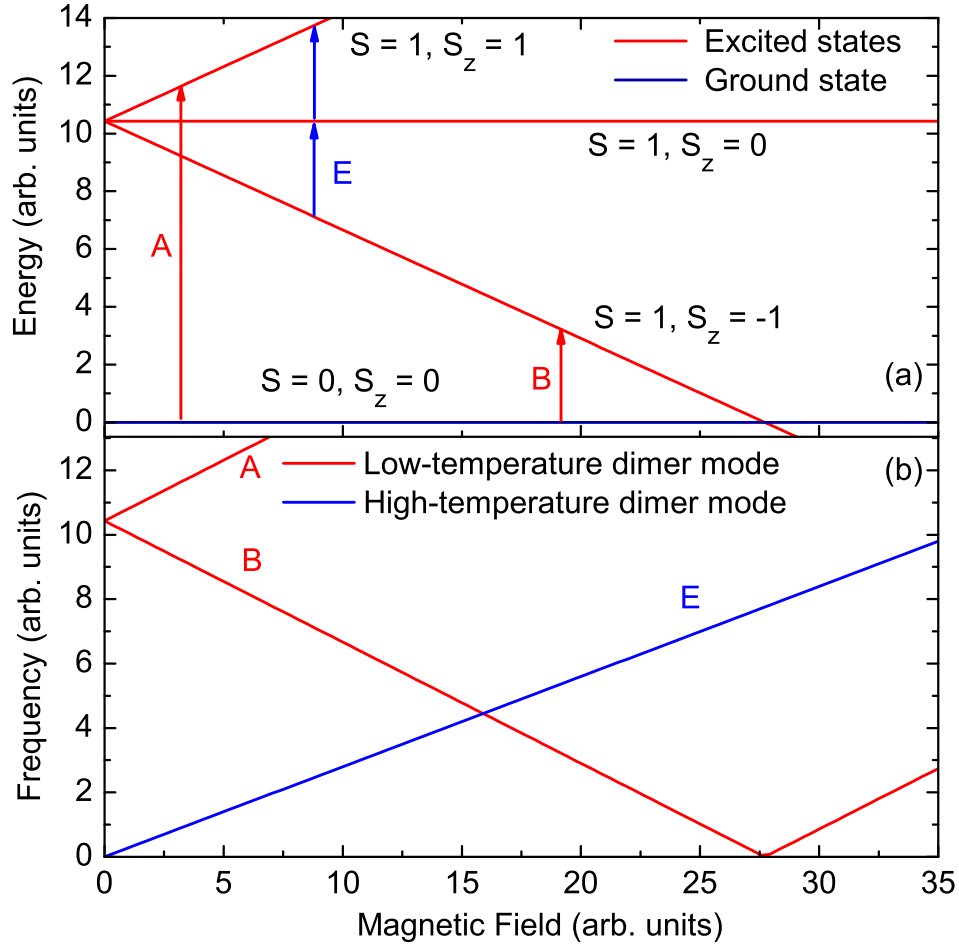


Figure 3.7: (a) Energy-level diagram for a spin-dimer system. Colors of arrows correspond to colors of the modes. (b) The expected frequency-field diagram of the magnetic excitations for a spin-dimer system.

the values H_{c1} and H_{c2} at zero temperature. We found $H_{c1}^* > H_{c1}$ and $H_{c2}^* < H_{c2}$. This finding is in qualitative agreement with the temperature-field phase diagram of $Ba_3Cr_2O_8$ studied before (Fig. 3.2) [61]. One should note, however, that the ESR modes are not directly related to the phase transition observed before (Fig. 3.2).

Mode E corresponds to transitions between the different S_z states inside $S = 1$. The slope of mode E is the same as the slopes of A, B, C, and D corresponding

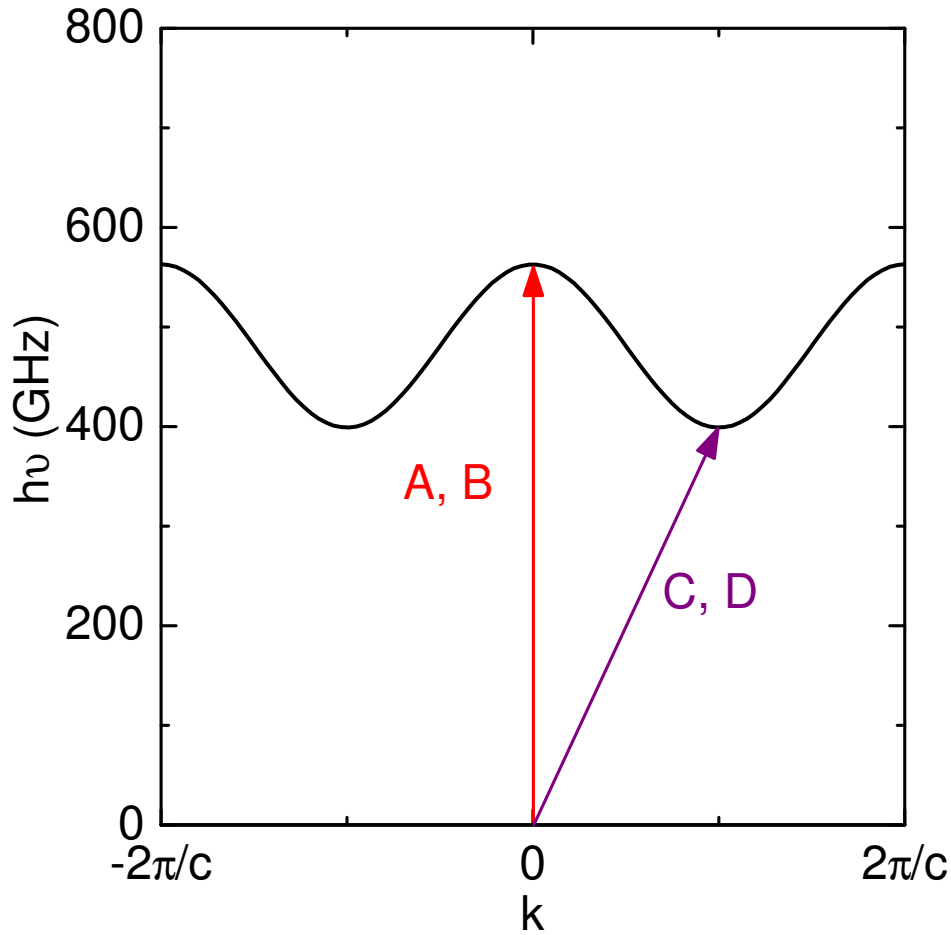


Figure 3.8: Dispersion of the triplet levels in a spin-dimer system. Arrows show transitions observed by ESR.

to $g = 1.94$. These findings are in agreement with the energy-level diagram in Fig. 3.7.

The temperature evolution of the ESR spectra has been studied as well. Figure 3.9 shows ESR spectra measured at 312 GHz and two different temperatures. As can be rationalized from Fig. 3.7, the ESR intensity of the modes D and B is large at low temperatures and decreases with increasing temperature because of the decreasing population difference between the $S = 0$ and $S = 1$ states.

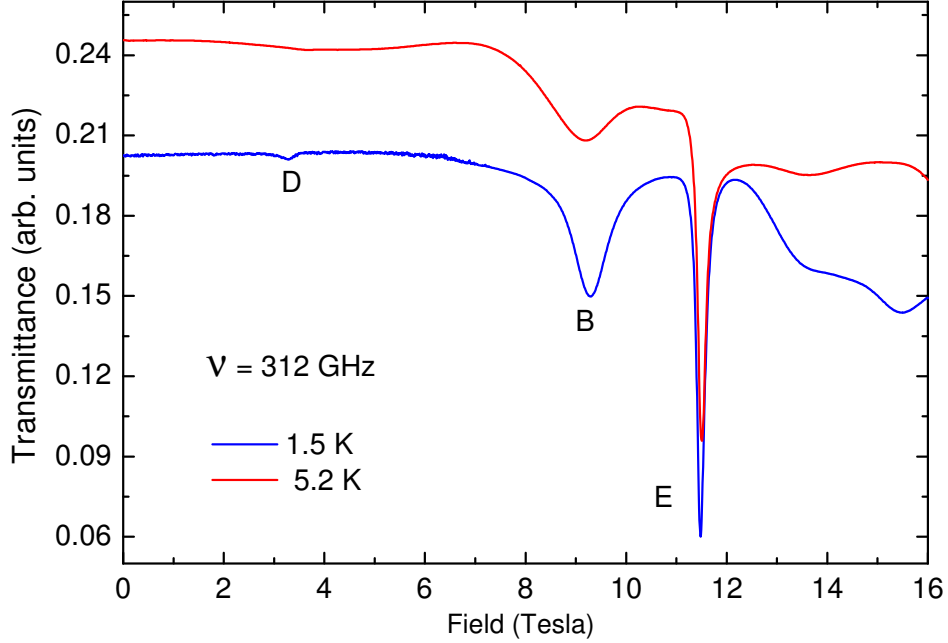


Figure 3.9: ESR absorption spectra of $Ba_3Cr_2O_8$ measured at 1.5 K (blue curve) and 5.2 K (red curve) at 312 GHz.

There is another important feature visible in the ESR spectrum at 5.2 K. The mode B is present at 5.2 K which is above the maximal transition temperature $T_c \simeq 2.7$ K. This indicates the presence of short-range ordering at temperatures above 2.7 K. This is a general property of systems with reduced dimensionality; the short-range ordering usually appears at temperatures well above T_N . The large intradimer coupling, $J_0 = 27.6$ K, in $Ba_3Cr_2O_8$ leads to short-range order in dimers. But the frustrated interdimer interaction leads to a suppression of 3D ordering. However, the magnetic excitations in the dimer subsystem are observable even in the disordered state.

The interpretation of the high-field ESR spectra (Fig. 3.5) above H_{c1} is more challenging. The transmissions exhibit a very complex structure, although being well reproducible for up- and down-field sweeps. Just mode E shows a continuous linear dependence up to maximum available frequencies (see Fig. 3.6). The presence of hysteresis found in the vicinity of H_{c2} by means of magnetization and magnetocaloric-effect measurements [61] suggests a more sophisticated picture

of the magnetic interactions in $\text{Ba}_3\text{Cr}_2\text{O}_8$, possibly involving a complex magnetic domain structure.

3.4 Conclusion

In conclusion, high-frequency ESR studies of the weakly coupled spin-dimer system $\text{Ba}_3\text{Cr}_2\text{O}_8$ were performed in magnetic fields up to 25 T. We observed transitions between the singlet ground state ($S = 0$) and excited triplet states ($S = 1$) (modes A, B, C, and D in Fig. 3.6) at 1.4 K. The detailed investigations of the frequency-field dependence of these transitions allowed us to extract highly accurate values of the gaps, namely $\Delta_{AB} = 563 \pm 1$ GHz (27.0 K) and $\Delta_{CD} = 399 \pm 1$ GHz (19.1 K). The observations of the transitions between singlet and triplet states clearly indicates the presence of a non-secular term allowing these transitions in this compound. The temperature dependence of the ESR spectra was studied as well. I hope that the present results (in particular, the observation of complex transmittance spectra above H_{c1}) will stimulate further theoretical and experimental investigations of spin-dimer systems.

4 Magnetic properties of the quasi-one-dimensional frustrated compound $\text{Cu}_3(\text{CO}_3)_2(\text{OH})_2$

4.1 Introduction

Geometrically frustrated systems are worthwhile to study, since it allows to investigate pure frustration effects on the physical properties, not worrying about randomness, which inevitable appears in a spin-glass system. One-dimensional (1D) quantum frustrated spin systems have the advantage that a precise comparison between experimental and theoretical results is possible.

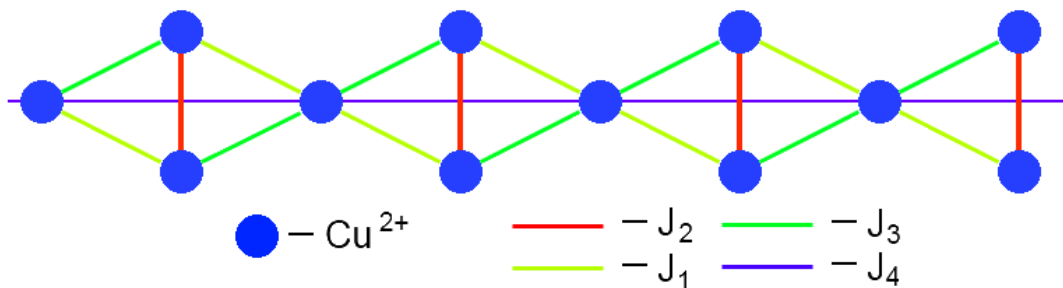


Figure 4.1: The magnetic structure of $\text{Cu}_3(\text{CO}_3)_2(\text{OH})_2$.

One important geometrically frustrated 1D quantum systems is the diamond chain in which diamond-shaped units compose a one-dimensional lattice (Fig. 4.1). K. Takano *et al.* [68] studied theoretically the ground state of a prototypical diamond chain ($J_1 = J_3$) and T. Tonegawa *et al.* [69, 70] investigated the ground state of the more general case in which the exchange coupling constants J_1 , J_2 , and J_3 between adjacent $S = 1/2$ spins are different from each

other (distorted diamond chain). They determined the phase diagram at $T = 0$ which is composed of a ferrimagnetic phase, a dimerized phase, and a spin-fluid (SF) phase. The distorted diamond chain is approximated to be a periodic array of J_2 -dimer and monomer spins if $J_2 \gg J_1, J_3$, or an alignment of linear trimer spins when J_1 (or J_3) $\gg J_2$. In these two extreme cases, a $1/3$ magnetization plateau is intuitively understood to be present.

However, experimental works concerning the magnetic properties on the diamond chain have not progressed because of a lack of suitable substances. Kikushi and his co-workers proposed $\text{Cu}_3(\text{CO}_3)_2(\text{OH})_2$ as a model substance for an $S = 1/2$ diamond chain in 2003 [71]. This compound has attracted great interest after H. Kikushi and co-authors found a plateau in the magnetization curve [72].

$\text{Cu}_3(\text{CO}_3)_2(\text{OH})_2$ is the well-known natural mineral azurite. Azurite is a soft, deep-blue copper mineral produced by weathering of copper ore deposits. Azurite was used as a blue pigment for centuries. First investigations of the physical properties of azurite are dated back to the middle of the twentieth century [73–78].

The crystallographic structure of azurite was first determined by G. Gattow and J. Zeeman (1958) [73], refined using single-crystal neutron-diffraction data by F. Zigan and H. Schuster (1972) [74], and using X-ray diffraction data by E. Belokoneva *et al.* (2003) [79]. The crystal structure of $\text{Cu}_3(\text{CO}_3)_2(\text{OH})_2$ (Fig. 4.2) has the space group $P2_1/c$ with the lattice constants $a = 501.09$ pm, $b = 584.85$ pm, $c = 1034.5$ pm, and $\beta = 92.43^\circ$ [74]. The magnetic structure of $\text{Cu}_3(\text{CO}_3)_2(\text{OH})_2$ corresponds to the scheme shown in Fig. 4.1. The diamond spin-chain direction is aligned along the b direction. The magnetic exchange pathways for the J_1 , J_2 , and J_3 couplings are along the Cu-O-Cu bonds with angles of 113.7° , 97° , and 113.4° , respectively. Hence, the Goodenough-Kanamori-Anderson rules for superexchange predict weakly antiferromagnetic couplings [80]. Magnetic long-range order was reported to occur at about 1.85 K [75, 76]. The axis of easy magnetization was found to be $55 \pm 5^\circ$ from the c axis toward the a axis [76, 77]. Love *et al.* performed a detailed investigation of the temperature-field phase diagram of this compound by adiabatic magnetizations measurements in combination with a specific-heat study [77]. For the magnetic fields applied parallel to the easy axis, they reported a spin-flop transition at about 1.6 – 1.95 T for temperatures below 1.6 K.

More detailed investigations of azurite were done by H. Kikushi *et al.* [71, 72], H. Ohta *et al.* [82–84], and K. Rule *et al.* [85–88] at the beginning of the twenty-first century. The specific heat (Fig. 4.3a) has a sharp peak at 1.8 K (lambda-type anomaly). This anomaly is reflecting the occurrence of long-range antiferromagnetic order. In addition, the authors found two rounded humps at tem-

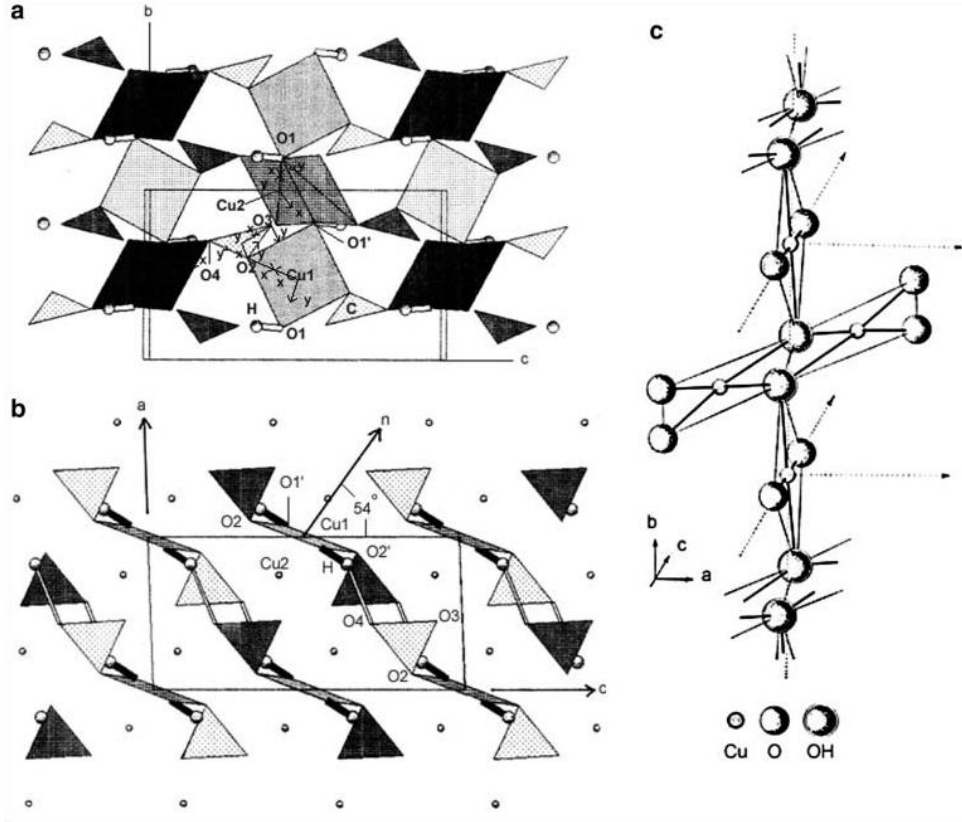


Figure 4.2: The crystallographic structure of $\text{Cu}_3(\text{CO}_3)_2(\text{OH})_2$ [79].

peratures around 4 and 18 K. These temperatures coincide closely with those where the magnetic susceptibilities also show rounded anomalies (Fig. 4.3b) [72].

The main finding of the investigations of Kikuchi *et al.* (Ref. [72]) is a plateau in the magnetization curve. Figure 4.4a shows the magnetization curves of $\text{Cu}_3(\text{CO}_3)_2(\text{OH})_2$ at magnetic fields aligned along the spin-chain direction ($H \parallel b$). The magnetization plateau starts at $H_{c1} = 16$ T. The magnetization stays at an approximately constant value of $0.3\mu_B$, which is almost $1/3$ of M_s up to $H_{c2} = 26$ T. The magnetization is nearly saturated at $H_{c3} = 32.5$ T with a magnetization of $M = 0.95\mu_B/\text{Cu}^{2+}$. The observed M is slightly smaller than the expected saturation value for Cu^{2+} ($g\mu_B S = 1\mu_B$, for $g = 2$). When the magnetic field is perpendicular to the chains ($H \perp b$): $H_{c1} = 11$ T, $H_{c2} = 30$ T, and $H_{c3} = 32.5$ T. The critical fields become more distinct at low temperatures.

The exchange interactions J_1 , J_2 , and J_3 were calculated applying the density matrix renormalization group method for the magnetization and high temper-

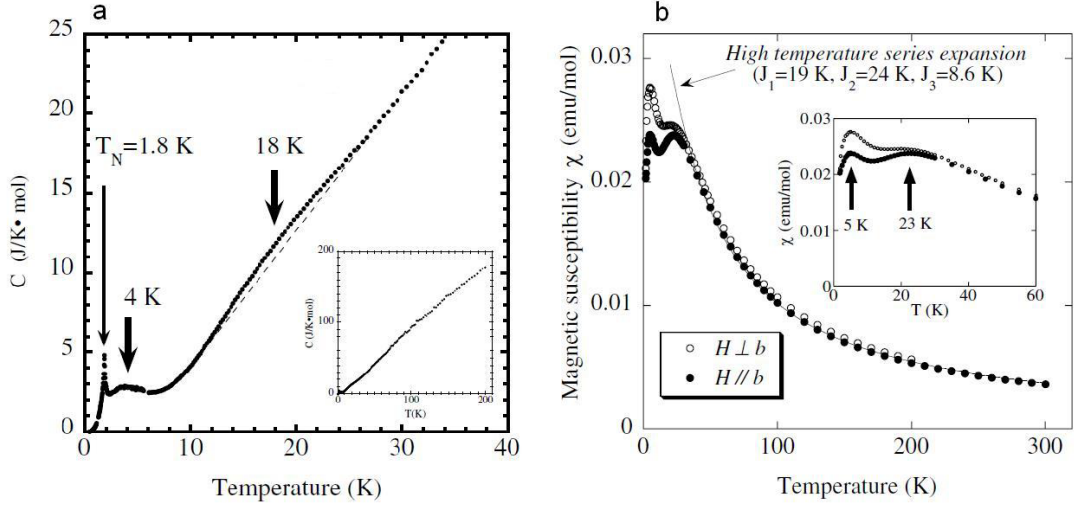


Figure 4.3: (a) Temperature dependence of the low-temperature specific heat. The inset shows the specific heat for the entire temperature range. The broken line is a guide for the eyes to make an anomaly at around 18 K clearer. Note, that a lattice contribution is not subtracted. (b) Temperature dependence of the magnetic susceptibilities for $H \parallel b$ and $H \perp b$. The solid line is a fit by use of a high-temperature series expansion using the parameters shown in the figure. The inset shows the low-temperature part of the magnetic susceptibilities. The diamagnetic contribution from core electrons is subtracted in this figure [72].

ature series expansion for the magnetic susceptibility. The best fit result was obtained for $J_1 = 19$ K, $J_2 = 24$ K, and $J_3 = 8.6$ K.

The magnetic properties of azurite were investigated by means of electron spin resonance (ESR) as well. First investigations were performed in 1981 by Reddy and Sarma [81] at room temperature and 80 K. More detailed investigations were done by the group of H. Ohta [82–84]. In Ref. [82], the authors report ESR measurements at 90 K and estimated the g -values of azurite for the paramagnetic region, which are $g = 2.098$, 2.128 , and 2.110 for the magnetic field parallel to the a , b , and c axis, respectively. Measurements from 1.8 to 265 K revealed a characteristic temperature dependence of the linewidth and a shift of the g -factor below 23 K, which corresponds to the first maximum observed in the temperature dependence of the magnetic susceptibility.

In Ref. [83], high-field ESR measurements in the frequency region from 50 to 900 GHz at $T = 1.8$ K are reported. Results of the investigations are shown in the left panel Fig. 4.5. The obtained frequency-field dependence shows a num-

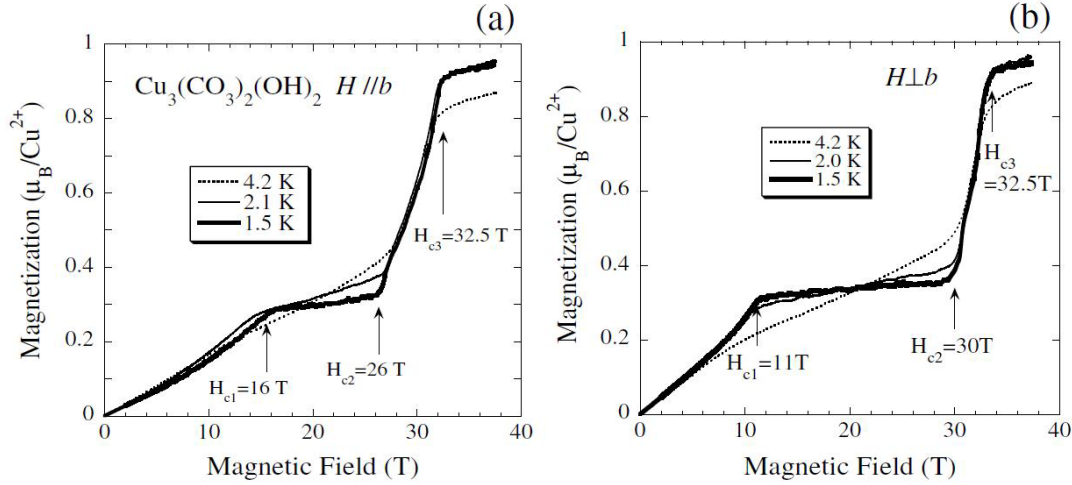


Figure 4.4: High-field magnetization curves. The magnetic field was applied along (a) and perpendicular (b) to the b axis, respectively [72].

ber of excitation modes. The most important result is the observation of resonance modes labeled C and D. The mode D has a gap of $\Delta_D = 1050$ GHz and at fields around H_{c1} it switches to the mode C. Moreover, the intensities of the modes C and D at 1.83 K are clearly stronger than those at 4.2 K. Therefore, the authors concluded that these are transitions arising from the ground state.

Results of ESR measurements at $T = 0.5$ K were published in Ref. [84]. These results are shown in the right panel of Fig. 4.5. At low-temperatures, the spectrum is significantly changed. Mode B is gapless at 1.8 K (Fig. 4.5 left), but has a gap of $\Delta = 37$ GHz at 0.5 K. In addition to the modes found at 1.8 K, a new mode (labeled C in Fig. 4.5 right) appears. The energy of this mode decreases with increasing magnetic fields, and the gap is closed slightly above H_{c1} .

Azurite also was investigated by inelastic neutron scattering (INS) [85–87] and neutron diffraction [88]. Figure 4.6 shows results of the INS study published in Ref. [85]. There are a few broad peaks in the spectra above 3.5 meV. The lowest peak at around 4.5 meV (1088 GHz) corresponds to mode D found by means of ESR (Fig. 4.5 a). When an external magnetic field is applied, the peak is shifted to lower energy (Fig. 4.6 right) in agreement with the ESR results. The dispersion, $E(k)$, of this peak is clearly visible in Fig. 4.6 right. The other branches above 3.5 meV are superimposed and yield a broad distribution of scattering intensity, prohibiting a precise determination of peak positions.

The peaks at energies below 2 meV were investigated in Ref. [87]. There is evidence for two gaps at the AFM Brillouin-zone center located at $\Delta_1 = 0.4$ meV

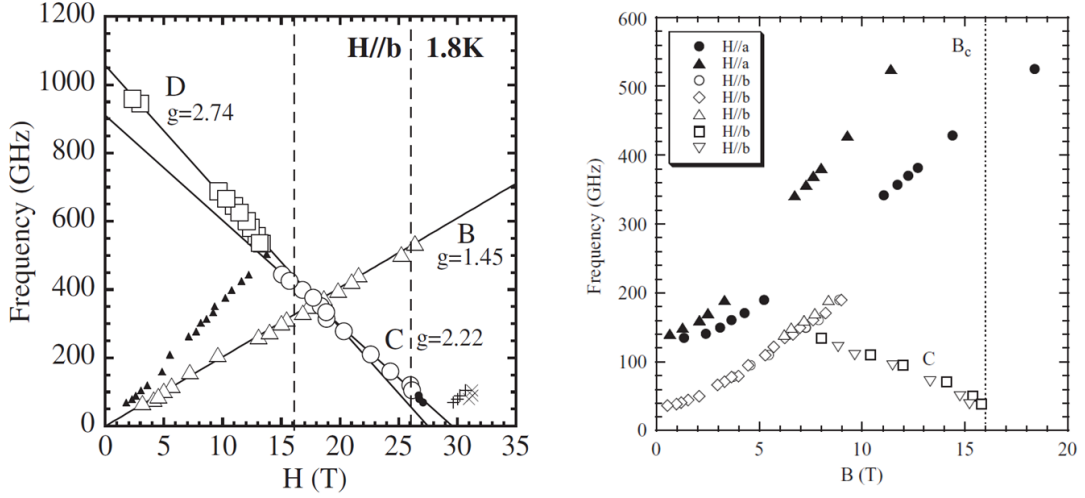


Figure 4.5: (Left) Frequency-field diagram of $\text{Cu}_3(\text{CO}_3)_2(\text{OH})_2$ observed at 1.8 K for $H \parallel b$. The major resonances B, C and D are represented by large symbols, while the minor resonances are shown by small symbols. The field range between 16 and 26 T corresponds to the $1/3$ magnetization-plateau region observed in the magnetization measurement at 1.5 K [83]. (Right) The frequency-field diagram at 0.5 K. Solid symbols correspond to $H \parallel a$. Open symbols correspond to $H \parallel b$ [84].

and $\Delta_2 = 0.6$ meV (see Fig. 4.7). While the dispersion resembles the scattering from a 1D Heisenberg antiferromagnetic chain (HAFC) with a spinon continuum, this model is gapless as demonstrated in the simulation of Fig. 4.7(c).

Thus, INS results have shown that the low-energy spectra of azurite are not well described by the 1D HAFC model. Instead, more complex interaction pathways are a necessary addition to the spin-chain Hamiltonian to describe the observed features.

There have been a number of attempts to derive a microscopic model for the complex magnetic properties of $\text{Cu}_3(\text{CO}_3)_2(\text{OH})_2$ [72, 85, 89–91]. However, the results are contradictory and up to now none of these models was able to yield a fully consistent picture of the experimentally observed behavior. It is interesting that very different sets of J_1, J_2, J_3 , and additional (interchain) J_i or monomer-monomer J_m parameters can describe the data of the magnetization, magnetic susceptibility, and specific heat. However, these models cannot describe the excitation spectrum of azurite.

In this chapter, I discuss our systematic studies of the magnetic excitation spectrum of $\text{Cu}_3(\text{CO}_3)_2(\text{OH})_2$ by tunable-frequency ESR experiments in magnetic fields up to 50 T. I studied the magnetic properties of this system near

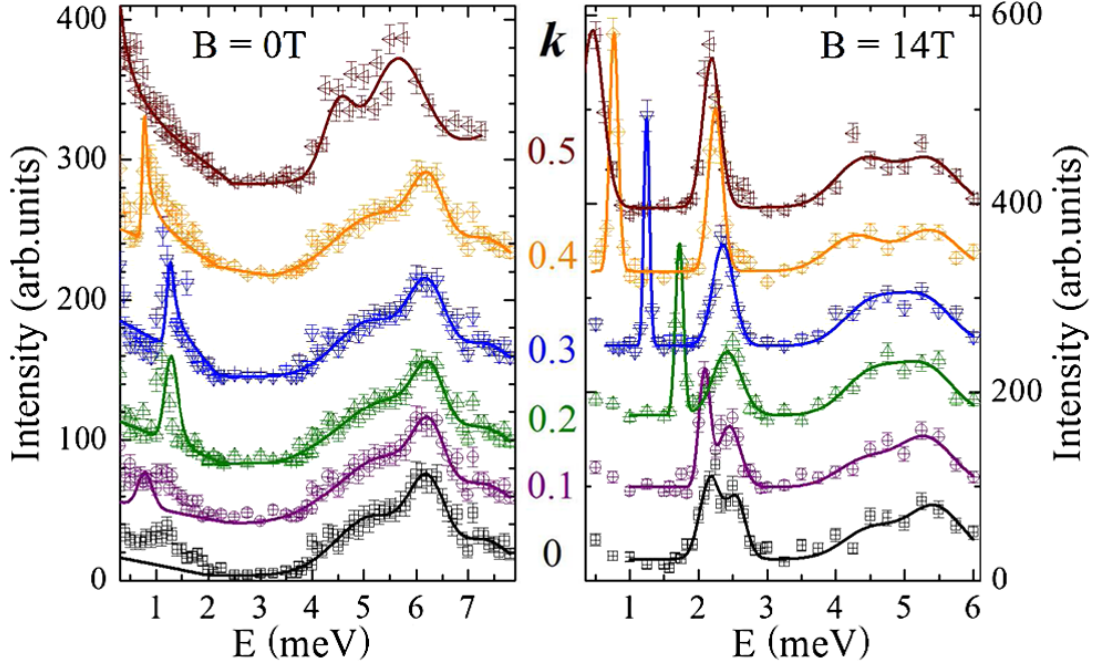


Figure 4.6: Energy dependence of the INS spectra of azurite at $\mathbf{q} = (1, k, 0)$, $k = 0$ to 0.5 , in zero field (left) and at a field of $14 \text{ T} \perp b^*$ (right) at $T = 1.5 \text{ K}$. Lines indicate fits to the data, which are shifted for clarity; for details see text (from Ref. [85]).

the ground state trying to obtain the correct microscopic model able to describe the magnetic properties of azurite.

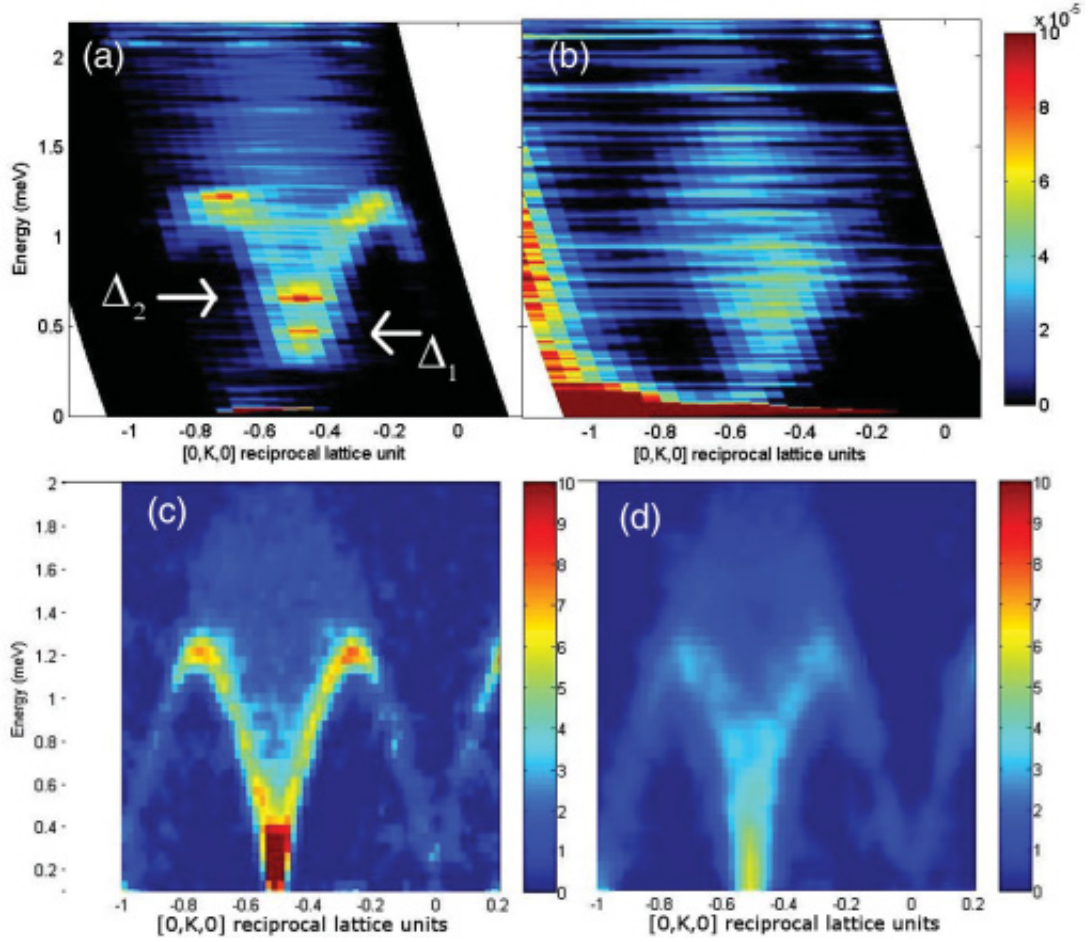


Figure 4.7: INS data from azurite along the Cu-chain direction shown at 0.04 K (a) and 2.5 K (b). The dispersion at 40 mK resembles the 1D HAFC with a spinon continuum. However, this model does not account for the energy gaps, Δ_1 and Δ_2 , clearly observed in the experimental data (indicated by the arrows). The lower plots show the expected scattering from a 1D HAFC at 0.04 K (c) and 2.5 K (d) from Ref. 4.7.

4.2 Experimental details

Natural single crystals of the $\text{Cu}_3(\text{CO}_3)_2(\text{OH})_2$ were used. The samples were cut from a large high-quality crystal. The sample was polished perpendicular to the principle axes. The size of the sample is $2 \times 3 \times 7 \text{ mm}^3$. The obtained results were verified by measurements of other samples. Here, I should point out that malachite $\text{Cu}_2(\text{CO}_3)_2(\text{OH})$ easily aggregates with azurite $\text{Cu}_3(\text{CO}_3)_2(\text{OH})_2$. Azurite

is unstable in open air and often is replaced by malachite. This weathering process involves the replacement of the carbon dioxide (CO_2) units with water (H_2O), changing the carbonate: $2\text{Cu}_3(\text{CO}_3)_2(\text{OH})_2 + \text{H}_2\text{O} \rightarrow 3\text{Cu}_2(\text{CO}_3)(\text{OH})_2 + \text{CO}_2$. The quality of the used samples and precise orientation of the axes were confirmed by X-ray diffraction.

ESR experiments have been done using the described tunable-frequency ESR spectrometers operating in combination with a 16 T superconducting magnet [46] and 50 T pulsed magnet [64] at the Dresden High Magnetic Field Laboratory [92]. The magnetic field was applied along the k vector of the radiation (Faraday geometry). BWOs and VDI microwave sources were used as tunable sources for the sub-THz radiation. Measurements were performed at frequencies from 50 up to 1000 GHz.

Measurements at frequencies above 1 THz have been done at the High Field Magnetic Laboratory in Nijmegen (the Netherlands). For that a far-infrared Bruker spectrometer in combination with a 33 T resistive magnet has been used.

High-field magnetization data have been measured in pulsed magnetic fields up to about 60 T at different temperatures using an induction method. Details of the measurements are described in Ref. [93]. The pulsed magnets used for the ESR and magnetization experiments have been described elsewhere [43].

4.3 Results

The measurements of the ESR spectra have been done for magnetic fields applied parallel to all principle crystallographic axes. The most interesting and important results were obtained for magnetic field aligned parallel to b (spin-chain direction). We investigated the ESR properties up to 50 T using pulsed magnetic fields. Examples of the obtained ESR spectra are shown in Fig. 4.8. We observed several excitation modes for $H \parallel b$ at 1.5 K. There are a two modes, J and F, at low fields. The energies of these modes increase with magnetic field. The energy of mode C decreases with increasing applied field. These modes have been reported before by Ohta *et al.* [84] (Fig. 4.5 left). Additionally, we was able to observe the mode E at fields above H_{c3} . The resonance frequency of this mode increases linearly with field.

Since modes F, J, and C appear at low magnetic fields, we performed detailed investigations of this modes using our superconducting 16 Tesla magnet. Figure 4.9 shows an example of the transmission signal at a high microwave frequency ($\nu = 853$ GHz) and low temperature ($T = 1.5$ K). The two lines in the graph correspond to the up and down sweep of the magnetic field.

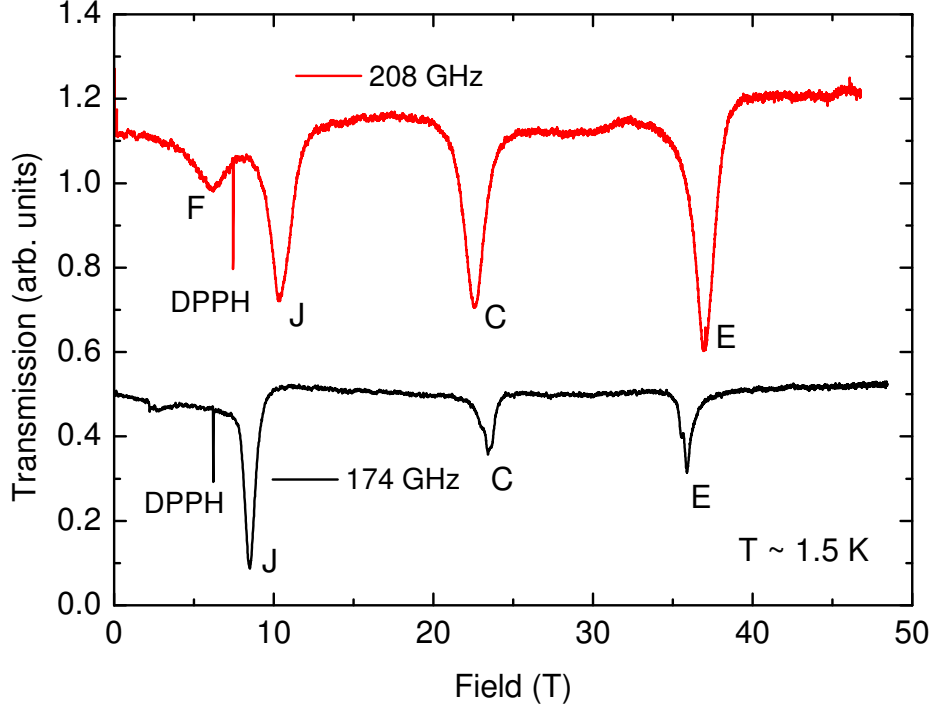


Figure 4.8: Transmission signal of $\text{Cu}_3(\text{CO}_3)_2(\text{OH})_2$ at $T = 1.5$ K and $H \parallel b$. DPPH is a magnetic-field marker.

Detailed investigations of the mode A in a broad range of frequencies and magnetic fields have been performed. At zero field, the mode A has a frequency of $\Delta_A = 1043$ GHz (4.31 meV). The mode A in Fig. 4.9 is the same as mode D found by Ohta (Fig. 4.5). However, we resolved that this mode is split into two modes denoted A and B (Fig. 4.9). This observation is in agreement with the dispersion of the mode reported by Rule *et al.* (see Fig. 4.6 and Ref. [85]). They report a dispersion of this mode between 2.5 – 2.2 meV (72.5 GHz) in 14 Tesla. The modes A and B correspond to transitions in the center and at the border of the Brillouin zone. We found a frequency difference between the A and B modes of 75 GHz in the field range from 1 to 11 T (Fig. 4.11). In addition, for modes A and B deviations from linear behavior at fields below 3 T have been found.

Figure 4.10 shows an ESR spectrum obtained at 73 GHz and 1.5 K using the superconducting magnet. One of the two modes observed is mode J which

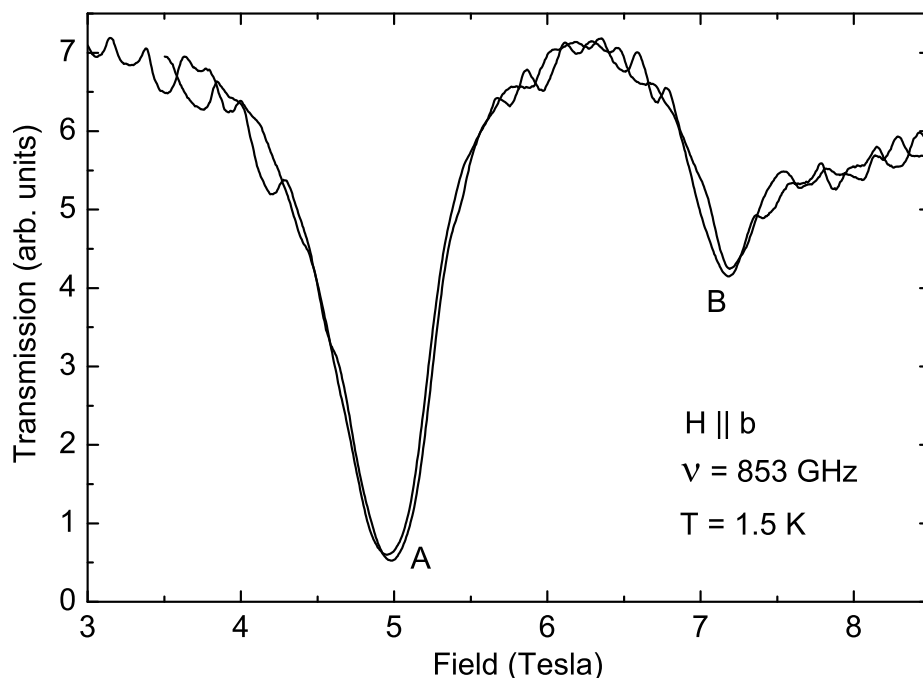


Figure 4.9: Transmission signal of $\text{Cu}_3(\text{CO}_3)_2(\text{OH})_2$ at 853 GHz, $T = 1.5$ K, and $H \parallel b$.

was seen at higher frequencies also in pulsed-field experiments. At about 13 T mode, O appears. This mode corresponds to mode C reported by Okubo *et al.* (Fig. 4.5 right). Remarkably, we observed this mode at 1.5 K while Okubo *et al.* found this mode at 0.5 K.

The results of our ESR investigations at low temperature are summarized in Fig. 4.11. Figure 4.11 shows the field dependence of the ESR modes at $T = 1.5$ K and $H \parallel b$. Azurite exhibits a very rich excitation spectrum. There are a lot of features in the excitation spectrum which have not been reported before. Mode A changes to mode C between 13 and 14 T, which is slightly below H_{c3} . The modes F, J, A, C, and O were observed before [83, 84], the modes B, D, E, and H have not been reported before. The modes have the following slopes: $g_J = 1.42$, $g_A = g_B = 2.69$, $g_C = 2.08$, $g_E = 1.96$, $g_D = 1.79$, and $g_F = 2.64$. These values have been obtained by linear regression of the experimental points.

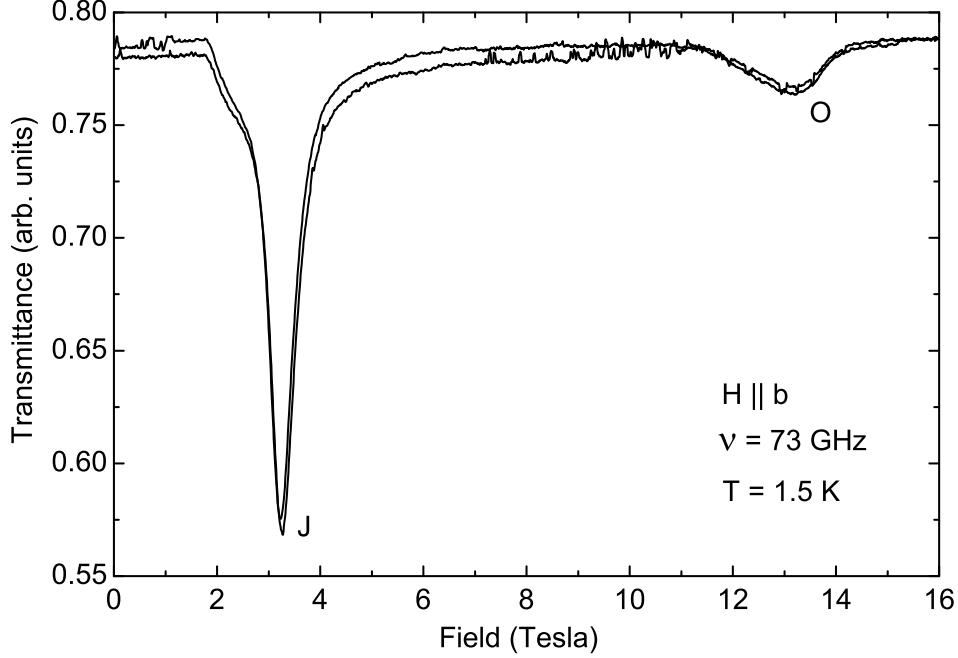


Figure 4.10: Transmission signal of $\text{Cu}_3(\text{CO}_3)_2(\text{OH})_2$ at 73 GHz, $T = 1.5$ K, and $H \parallel b$.

The slopes of the modes J, A, and C are in agreement with previous investigations [84]. Mode F shows a very interesting behavior. Okubo *et al.* found a gapless mode F at 1.8 K (closed triangles in Fig. 4.5 left), but did not find this mode at 0.5 K. One can estimate a gap of $\Delta_F \approx 160$ GHz of this mode at 1.4 K. We investigated the temperature dependence of mode F and found the gap opening at around $T_N = 1.8$ K.

We studied the evolution of the ESR spectra between 1.4 and 15 K. Field-dependent ESR absorption data of $\text{Cu}_3(\text{CO}_3)_2(\text{OH})_2$ at 300 GHz for different temperatures are shown in Fig. 4.12. In agreement with results obtained in pulsed field, there are two absorption peaks (F and J) at the lowest temperature ($T = 1.4$ K). When the temperature increases, the intensities of these peaks decrease and a new resonance peak, labeled G, appears (Fig. 4.12). The mode G shows the typical behavior for a resonance absorption in the paramagnetic phase. The resonance field of this mode increases linearly with frequency. The mode G is gapless with a slope of $g_G = 2.27$ at 40 K.

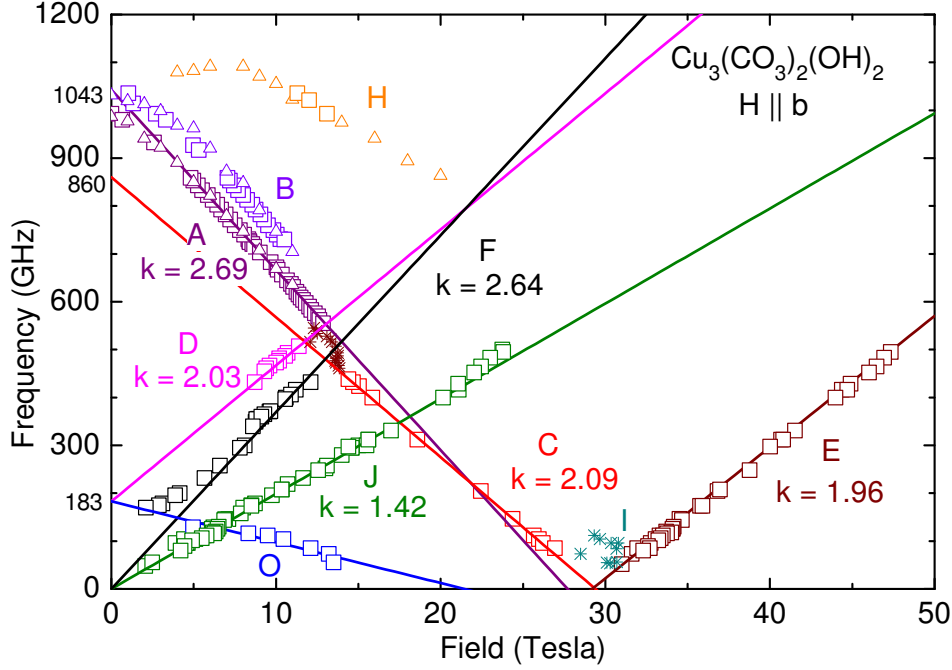


Figure 4.11: The frequency-field diagram for $H \parallel b$ at $T = 1.5$ K. Square symbols are obtained by use of the ESR setup at the HLD. Triangular symbols are obtained by the FIR experiment at the HMFL in Nijmegen. The solid lines are the result of calculations based on the energy diagram (Fig. 4.22). Stars mark experimental points which cannot be associated with observed modes.

The INS data measured by Rule *et al.* [85] reveal a broad peak structure at energies above 4 meV (970 GHz) in zero magnetic field (left panel of Fig. 4.6). For detailed investigations of this peak at different magnetic fields FIR experiments at frequencies above 1 THz at the HFML in Nijmegen have been performed. Figure 4.13 shows examples of the obtained spectra at different magnetic fields. We found a few absorption peaks which depend on the magnetic field. Two of them correspond to the modes A and B found by means of ESR. In addition, we found the very broad absorption peak H. Mode H shows a non-monotonic dependence on magnetic field. Most probably, this mode corresponds to the broad absorption peak reported by Rule *et al.* at energies of about 4.5 meV at 14 T (see Fig. 4.6). There are additional periodic fringes in the FIR spectra

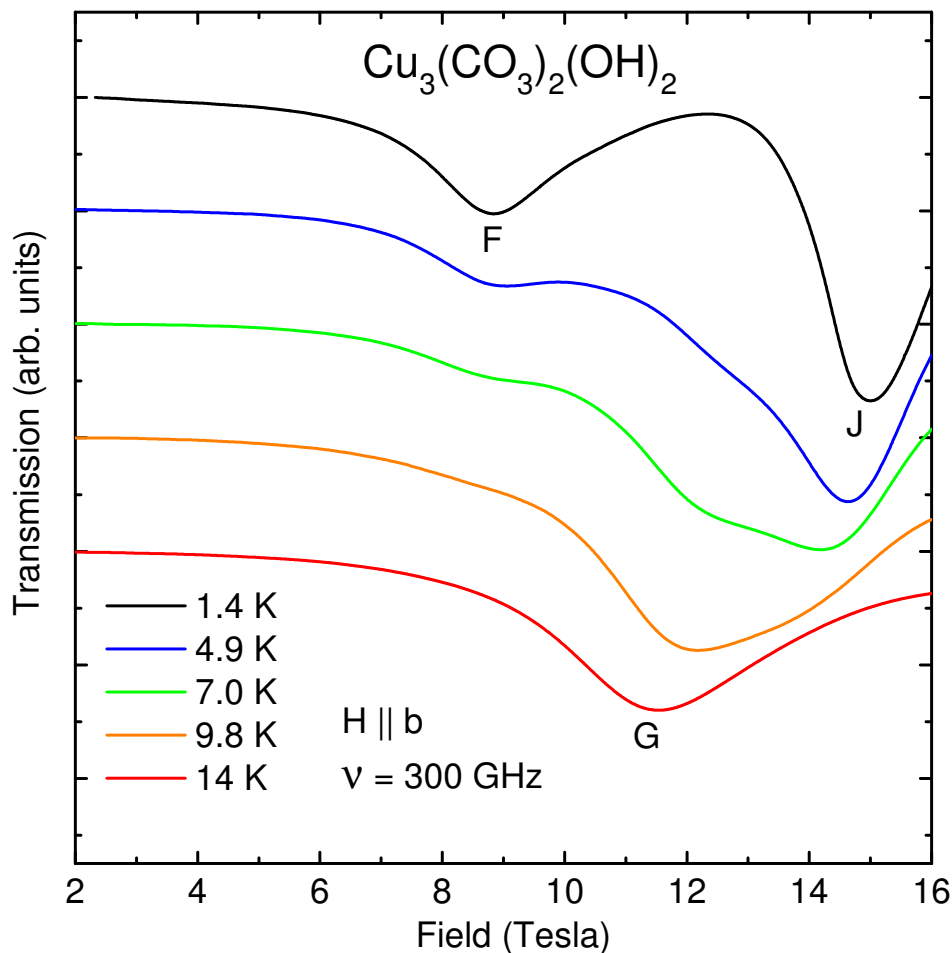


Figure 4.12: Temperature evolution of the field-dependent transmission for $H \parallel b$ at 300 GHz.

with a period of about 1 cm^{-1} . These fringes are induced by standing waves in the sample as well as in the optical system.

The FIR absorption peaks are shown by open triangles in Fig. 4.11. Modes A and B correspond perfectly to the results of our ESR measurements. For some frequencies, the mode H has been found by means of our ESR technique as well (orange squares in Fig. 4.11). In magnetic fields above 8 T, the frequency of this mode decreases with increasing magnetic field. The slope of this mode above

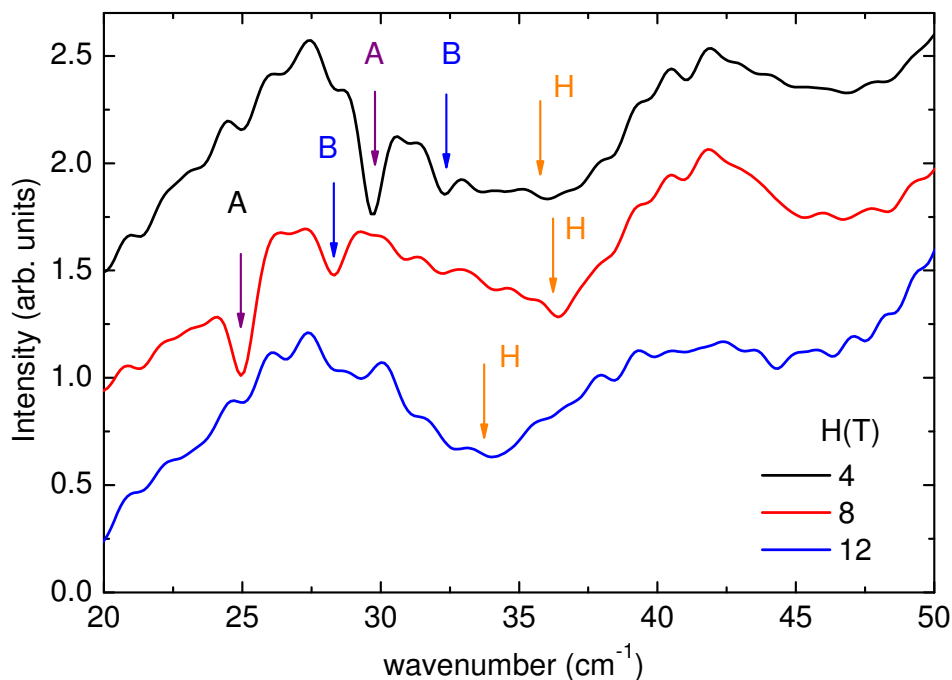


Figure 4.13: FIR spectra of $\text{Cu}_3(\text{CO}_3)_2(\text{OH})_2$ at different magnetic fields, $T = 1.4$ K and $H \parallel b$.

8 T is about 1.4. The deviation of this mode as function of magnetic field is important. I am discussing this finding in the following.

We as well measured the magnetization of the sample for $H \parallel b$ in pulsed magnetic fields at $T = 1.5, 18,$ and 50 K. The results are shown in Fig. 4.14. We found full agreement with the results of Kikushi *et al.* [72], but confirmed that the full saturation of the magnetization in $\text{Cu}_3(\text{CO}_3)_2(\text{OH})_2$ indeed appears towards 60 T.

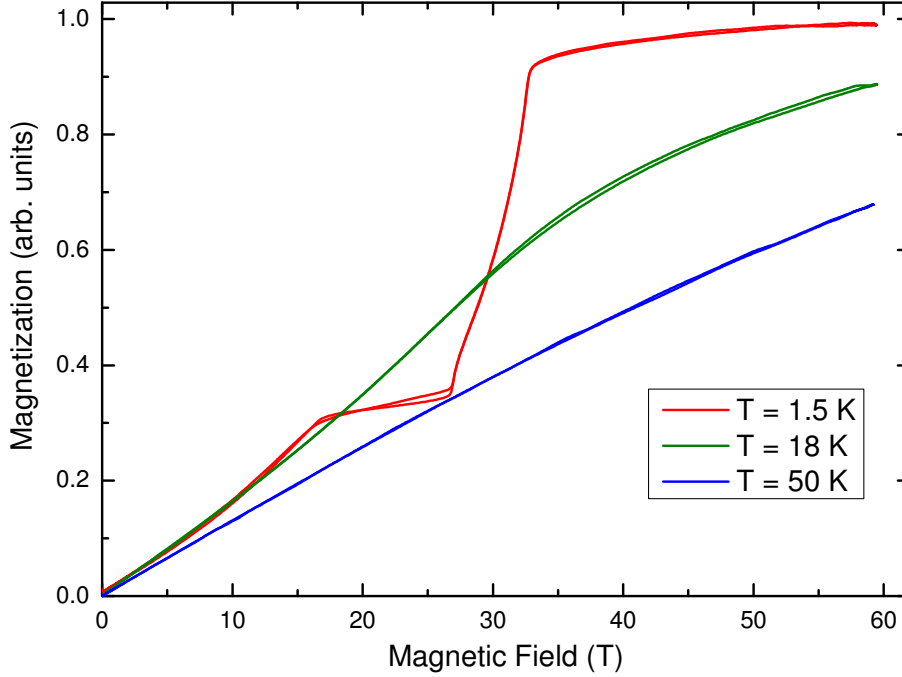


Figure 4.14: High-field magnetization curves at $T = 1.5, 18,$ and 50 K.

4.4 Discussion

4.4.1 Dimer-Monomer model

In a number of previous papers [72, 90, 91], the authors suggested a dimer-monomer model to describe the magnetic properties of azurite. This model can be easily understood on a qualitative level. Two thirds of the Cu^{2+} spins are strongly bound by the large exchange interaction J_2 into dimer singlets, while the other third remains as monomer spins which interact weakly by J_m and additional effective monomer-monomer interactions which are affected by integration with the dimers. In an applied magnetic field, the monomer spins are polarized first while the dimer spins remain in the singlet state, giving rise to the $1/3$ plateau (Figs. 4.4 and 4.14).

J. Kang *et al.* compared several different models to describe the magnetic properties of azurite [90]. The authors concluded: “Since $J_2 \gg J_1, J_3, J_4$, an isolated

dimer model would be reasonable for azurite at high temperatures. At low temperatures, the dimer-monomer exchanges J_1 , J_3 and J_4 cannot be neglected.” H. Ohta *et al.* made an attempt to describe their ESR data by the dimer-monomer model [83].

In the framework of the dimer-monomer description, it is believed that effective monomer spins of Cu^{2+} are responsible for the low-energy part of the excitation spectra, while the dimerized spin pairs primarily contribute to excitations at higher energies [87].

First, I consider a dimer subsystem. A detailed description of spin-dimer systems is given in the previous chapter on $\text{Ba}_3\text{Cr}_2\text{O}_8$. There is a spin-singlet ground state ($S = 0$) and spin-triplet first excited states ($S = 1$) (see Fig 3.7 a). The mode A at low fields and mode C at high fields (Fig. 4.11) most probably can be ascribed to transitions from the singlet ground state to the first excited triplet state. When the temperature increases, the intensity of the gapless ESR transitions between the levels with $S = 1$ increase. Mode G is gapless and exhibits such kind of temperature dependence (see Fig. 4.12). The expected frequency-field dependence of mode G is shown by the blue line in Fig. 3.7b. Thus, we may associate mode G with transitions between the levels with a total spin of 1.

The ESR signal from the monomer subsystem is expected to be a linear gapless mode [83]. Since the mode J is gapless and very intensive we can associate this mode with excitations from the monomers.

The Mode A associated with transitions in the dimer subsystem switches to mode C at about 12 T. This effect can be explained by introducing dimer-monomer interaction. Using mean-field approximation one can be parameterize the ESR excitations by

$$h\nu = \Delta_A - g\mu_B H + \mu_B H_{eff}, \quad (4.1)$$

where H_{eff} accounts for the internal field shift at the dimer site due to the alignment of neighboring monomers. In mean-field approximation H_{eff} should be a monotonic function of the monomer magnetization. The mode A, associated with transitions in the dimer subsystem, switches to mode C at about 12 T, which is slightly lower than the saturation field of the monomer subsystem. This effect cannot be described by the simple dimer model. Another important point is the difference between the slopes of modes A and G. From the energy-level diagram of a dimer system (Fig 3.7 a) the same slope for the modes A and G would be expected. However, the slope of mode A is significantly larger. There is a similar behavior seen for the modes C and E. These modes should have the same slope as well. As shown in Fig. 3.7a, these modes correspond

to transition between the same levels. Consequently, the dimer model is not sufficient to describe the obtained experimental data.

The dimer model has a few more drawbacks. The dimer subsystem should also show a mode which corresponds to transitions between the levels $|0, 0\rangle$ and $|1, 1\rangle$. As was found for $\text{Ba}_3\text{Cr}_2\text{O}_8$, this mode should have the same gap and slope as mode A. However, such mode has not been found. We instead observed the very broad mode H with a significantly different slope and non-linear field dependence. Furthermore, the dimer-monomer model cannot explain the modes F, D, and L.

Thus, the results of our ESR investigations confirm the statement of J. Kang that the dimer-monomer model cannot fully describe all magnetic properties of azurite at low temperatures. H. Ohta *et. al.* [83] indicated that the dimer-monomer model is sufficient only for a qualitative description of the magnetic properties of azurite.

4.4.2 Triangular model

As was shown in the previous subsection, the obtained frequency-field dependence (Fig. 4.11) cannot be described by the dimer-monomer model. I will try to explain the obtained results using a simple model.

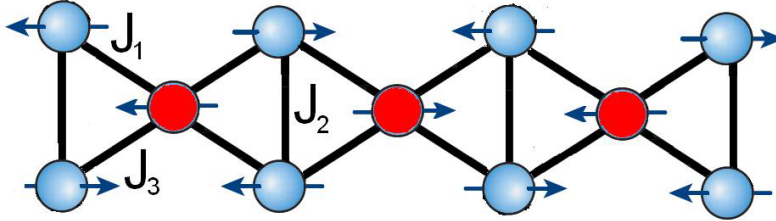


Figure 4.15: Simplified spin arrangement in $\text{Cu}_3(\text{CO}_3)_2(\text{OH})_2$ at low temperatures. Dimer sites are shown with blue color, monomer sites by red.

The arrangement of the Cu^{2+} ions in azurite is shown schematically in Fig. 4.15. There are a two possible excitations in the chain. The dimer excitation corresponds to flipping one of the spins interacting via J_2 (marked in blue in Fig. 4.15) and the monomer excitation corresponds to flipping a spin interacting via J_1 and J_3 (marked in red in Fig. 4.15). I will consider first the exchange model of the triangular building block with the highly anisotropic Cu^{2+} ions. The triangles consist of a dimer with the strong Heisenberg exchange coupling J_2 and a single Cu^{2+} ion. The interactions between the Cu^{2+} ions are shown in Fig. 4.16.

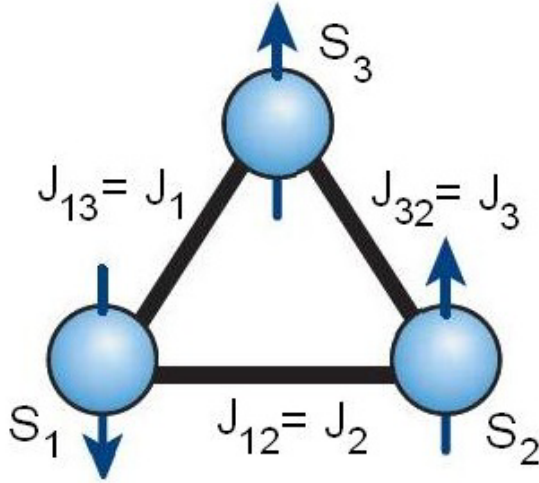


Figure 4.16: Assigned exchange interactions in the triangle.

The triangular spin system with antiferromagnetic exchange interactions (Fig. 4.16) has been studied experimentally [94] and theoretically [95]. There are eight possible states for such a system (Fig. 4.17). The ground state will be realized by one of the $S = 1/2$ states. There are six such states (three Kramers doublets) (Fig. 4.17 b, c, d). These configurations are degenerated in case of equal exchange interactions between the spins. But, if these interactions are different the degeneracy is removed. The state with parallel alignment of the spins (Fig. 4.17a) has the maximal energy. The total spin in this state is $S = 3/2$. Thus, such system will have at least two gaps at zero magnetic field.

The Hamiltonian of the system without antisymmetric interactions is

$$\mathcal{H} = -1/2 \sum_{ij} J_{ij} \mathbf{S}_i \cdot \mathbf{S}_j + \sum_i \mu_b \mathbf{S}_i g_i H. \quad (4.2)$$

There are eight possible states which are pairwise degenerated in zero field (Fig. 4.17 shows one orientation of the spins). The ground state (GS) (Fig. 4.17 b, c or d configuration) is determined by the exchange interactions J_1, J_2, J_3 . The excited state (ES) corresponds to the state with parallel alignment of all spins (Fig. 4.17a). The total spin in the excited state is $S = 3/2$. The energy spectrum of the scalene triangular clusters was described in detail by B. Tsukerblat and M. Belinsky [95]. The exchange interaction J_2 is much

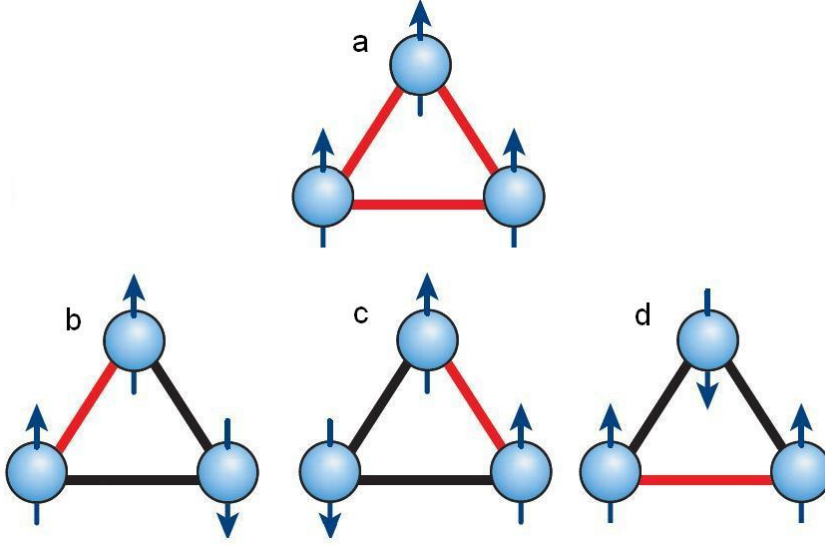


Figure 4.17: Possible configurations of the triangular-spin system. Pairwise interactions not satisfied are marked by red lines.

larger than J_1 and J_3 in azurite. In such a case, the energies of the different levels are given by [96]:

$$\begin{aligned}
 E_{ES} &= 1/2(J_2 + J_1 + J_3) + 1/3(2g_2 + g_3)\mu_B M_S H, \\
 E_{ED} &= 1/4\sqrt{(2J_2 - (J_1 + J_3))^2 + 3(J_1 - J_3)^2} + 1/2g_B\mu_B H, \\
 E_{GS} &= -1/4\sqrt{(2J_2 - (J_1 + J_3))^2 + 3(J_1 - J_3)^2} + 1/2g_A\mu_B H.
 \end{aligned} \tag{4.3}$$

The ground state is realized by the configuration *b* or *c* shown in Fig. 4.17, because $J_2 > J_1, J_3$. The energy gaps in zero field can be calculated from Eq. (4.3):

$$\begin{aligned}
 \Delta_{ES} &= 1/2(J_2 + J_1 + J_3) + 1/4\sqrt{(2J_2 - (J_1 + J_3))^2 + 3(J_1 - J_3)^2}, \\
 \Delta_{ED} &= 1/2\sqrt{(2J_2 - (J_1 + J_3))^2 + 3(J_1 - J_3)^2}.
 \end{aligned} \tag{4.4}$$

I discuss now the behavior of the triangular spin system with applied magnetic field. We as well as Ohta [83, 84] found two gaps in the frequency-field diagram (Fig. 4.11). The large gap, $\Delta_A = 1043$ GHz, should correspond to transitions between the GS and the ES (Fig. 4.17). The gap $\Delta_{ED} = 183$ GHz (Fig. 4.11)

corresponds to transitions from the GS to the state with the spin configuration in Fig. 4.17d.

Above formulas (Eq. 4.4) are just useable for a qualitative analysis of the energy spectra. There is no unique solution for our case. As an example, the estimated gaps $\Delta_A = 50$ K and $\Delta_F = 7$ K can be satisfied by $J_2 = 80$ K, $J_1 = 6$ K, and $J_3 = 5$ K. As well, we should admit that the ion S_3 (Fig. 4.16) is interacting with another dimer. This interaction can significantly shift the energy levels.

Here it is important to note, that even in case of an isosceles triangle ($J_1 = J_3$) the two lowest doublets are not degenerated. This important feature has been observed experimentally on a Cu_3 nanomagnet, where antiferromagnetically coupled Cu^{2+} ions form a slightly distorted triangle [94]. In the previous section, I discussed the dimer-monomer model. Since $J_1 \approx J_3$, dimer and monomer sites behave quasi independently in a magnetization process. The influence of one subsystem on the other can be described by mean-field approximation. Since a magnetic field can just move energy levels, this cannot lead to the appearance of new modes in the excitation spectra which has been found experimentally. However, the presence of the exchanges J_1 and J_3 lead to qualitatively new states of the system, kind of bound dimer-monomer states. These states are located between the monomer and dimer states on the energy scale. Thus, our results show that a full description of the spectroscopic properties of azurite may only be realized by taking into account the complete system with all exchanges.

4.4.3 Energy-level diagram

One of the main advantages of ESR measurements is the possibility to reconstruct a possible energy-level diagram from the obtained frequency-field dependence. Now, I am apply this standard procedure to the obtained results.

First of all, to avoid confusion, we introduce a labeling. Symbol g designates g -factors of the energy levels. The slope of the levels in the field-dependent diagram is gs_z . Symbol k corresponds to the slope of a mode in the frequency-field diagram.

Modes A and J. At low temperatures, these modes are the most intensive absorption peaks (more than 50 percent of the radiation power). The temperature evolution of the mode J is shown in Fig. 4.12. Its intensity decreases when the temperature increases. Okubo *et al.* have shown that the temperature dependence of mode A is the same [84]. Therefore, we can conclude that both modes correspond to transitions from the GS. Since, the Cu^{2+} ion has $s = 1/2$ with two possible projections, $s_z = \pm 1/2$, the huge absorption and gapless behavior of the mode J (green mode in Fig. 4.18a) suggest transitions inside the GS doublet. The mode J has a slope of 1.42. Thus, the GS can

be a doublet with g -factor $g_{GS} = 1.42$. We assign the two levels of this doublet as $|GS, -1/2\rangle$ and $|GS, +1/2\rangle$ (|State, spin projection>). These levels are marked by green lines in the energy diagram of Fig. 4.18b. Thus,

$$g_{GS} = 1.42.$$

The mode A has a gap of $\Delta_A = 1043$ GHz and an unusual slope of $k_A = -2.69$ (fit of the experimental data below 10 T). Taking into account the slope of the lowest $|GS, -1/2\rangle$ level, we can calculate the slope of the ES as:

$$k_{es} = k_A + g_{gs}s_z = -2.69 - 0.71 = -3.4.$$

This slope may correspond to the lowest level of a quadruplet $|ES, -3/2\rangle$ ($S = 3/2, s_z = -3/2$) with g -factor $g_{ES} = 2.27$. The levels of the $S = 3/2$ quadruplet are shown as violet lines in Fig. 4.18b. Thus, the mode A corresponds to transitions between $|GS, -1/2\rangle$ and $|ES, -3/2\rangle$ (marked with a violet arrow in Fig. 4.18b).

Mode C and E. Near the critical field, $H_{c1} = 16$ T [72], the mode A ($k_A = -2.69$) gradually crosses over to the mode C ($k_C = -2.08$). The intensity of this mode is strongest at magnetic fields above 20 T (frequencies below 250 GHz). Okubo *et al.* have shown that the intensity of mode C is maximal at low temperatures and decreases when the temperature increases. Such behavior means that this transitions stems from the GS as well as mode A. Because the intensity of mode C behaves similar as the intensity of mode A, and the plateau in the magnetization suggests a new phase, we can conclude that there is a change of the ground state. This change can be accomplished in one way only: by a crossing of the $|GS, -1/2\rangle$ level and the $m_S = -1/2$ level from an excited doublet (ED) denoted as $|ED, -1/2\rangle$ with a higher g -factor. The g -factor of this level is

$$g_{ED} = 2(k_A - k_C + k_{GS}) = 2.64.$$

Thus, mode C corresponds to the transitions from $|ED, -1/2\rangle$ to $|ES, -3/2\rangle$ (red arrow in Fig. 4.18b). One can calculate the energy of the ED at zero field (the gap) by extrapolation of the frequency of mode C to zero field:

$$\Delta_{ED} = \Delta_{ES} - \Delta_C = 183 \text{ GHz}.$$

Having the slope and the gap value of the ED, one can draw it in the energy diagram (red lines in Fig. 4.18b). Now, we can assign the mode F (black line and data in Fig. 4.11 a) to the transitions between the ED levels $|ED, -1/2\rangle$ and $|ED, 1/2\rangle$.

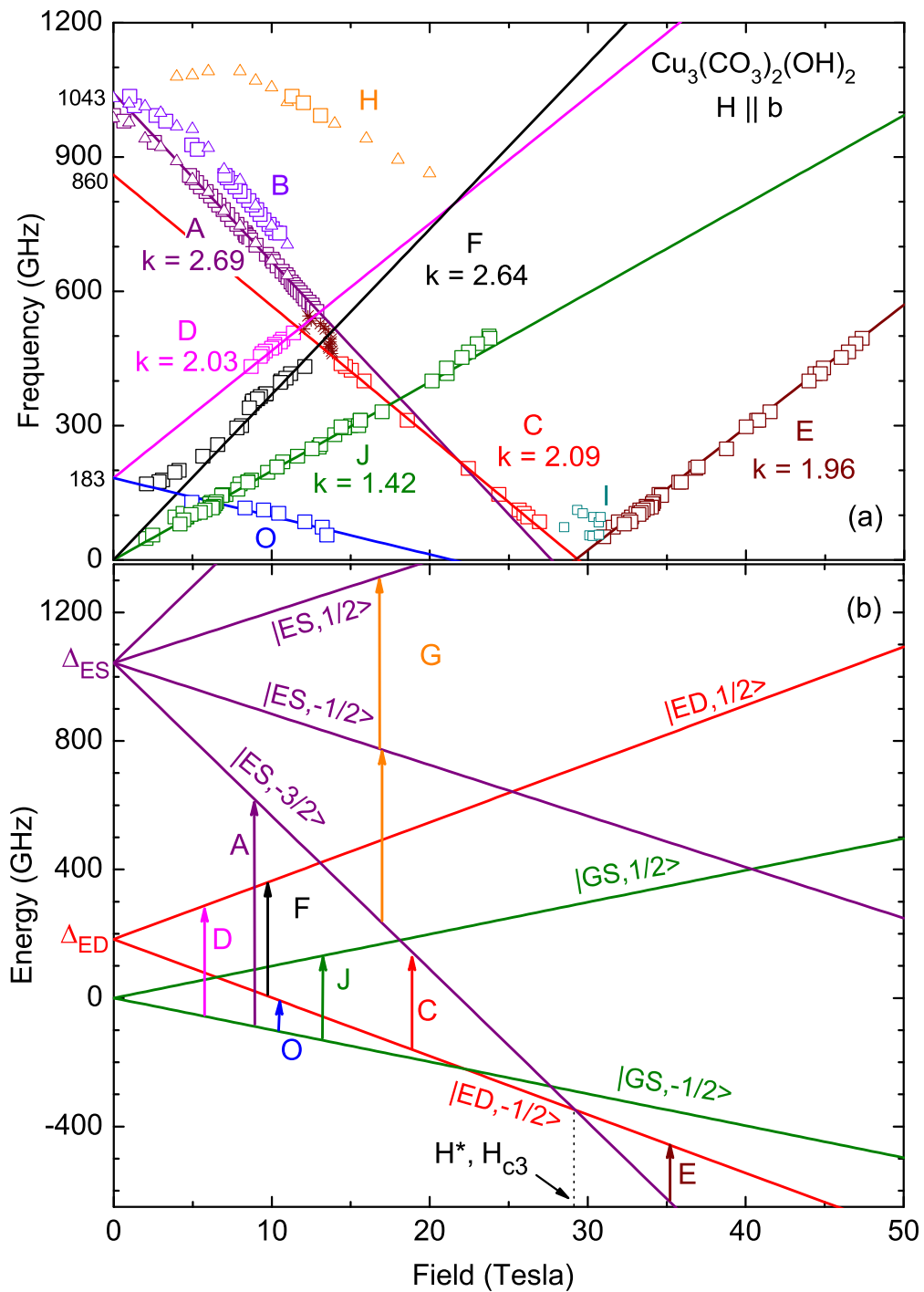


Figure 4.18: (a) Frequency-field diagram for $H \parallel b$ at $T = 1.5$ K. The solid lines are calculations based on the energy diagram (b). The colors of the arrows in (b) correspond to the colors of the modes in (a).

The mode E appears in fields above 30 T only. This can be immediately understood from the energy diagram (Fig. 4.18b). At H^* , the levels $|ES, -3/2\rangle$ and $|ED, -1/2\rangle$ cross each other. Thus, while the transitions from $|ED, -1/2\rangle$ to $|ES, -3/2\rangle$ are responsible for the mode C at $H < H^*$, the inverse transitions from $|ES, -3/2\rangle$ to $|ED, -1/2\rangle$ above H^* form the mode E (brown arrow in Fig. 4.18b). An important result is that the field H^* , where the levels $|ES, -3/2\rangle$ and $|ED, -1/2\rangle$ cross perfectly coincides with the metamagnetic transition from the $1/3$ plateau to saturation.

Mode F. For the mode F, our findings contradict the results of Ohta *et al.* [83]. For the static-field measurements, our data give $K_F = 2.35$ and a small gap (around 16 GHz). For the pulsed-field measurements, we, however, obtain a larger slope and a clear gap. Ohta *et al.* [83] found $g = 2.64$ (open points in Fig. 4.11). Probably, this contradiction is caused by a small misalignment and a large anisotropy of this mode. As we note above, we will associate mode F with transitions from $|ES, -1/2\rangle$ to $|ES, +1/2\rangle$ (red lines in the Fig. (4.18b)).

Mode D. In addition to the described modes, we have observed a very weak mode D. This mode exists only in a small magnetic-field interval. Based on our energy-level diagram, mode D can be assigned to the transitions from $|GS, -1/2\rangle$ to $|ED, 1/2\rangle$ (marked with a magenta arrow in Fig. 4.11b). This allows us to predict the slope of this mode

$$k_D = 1/2g_{ED} + 1/2g_{GS} = 1.32 + 0.71 = 2.03,$$

and the gap

$$\Delta_{ED} = 183 \text{ GHz.}$$

The experimental parameters of mode D are in agreement with this assignment. The calculated frequency-field dependence of this transition is shown with a magenta line in the Figs. 4.11 and 4.18a. The intensity of this mode is strongly field dependent. The intensity increases when the level $|ED, +1/2\rangle$ approaches $|ES, -3/2\rangle$. Such behavior and the difference between the experimental and estimated data (magenta dots and line in Fig. 4.11 and 4.18a) may be explained by avoided crossing of the levels $|ED, +1/2\rangle$ and $|ES, -3/2\rangle$ levels [97–99].

Mode O. Remarkably, from the calculated energy diagram (Fig 4.18b) we are able to describe the mode O obtained by Ohta *et al.* at 0.5 K [83] and by us at 1.5 K. The open triangles in Fig. 4.18a correspond to a transition from $|GS, -1/2\rangle$ to $|ED, -1/2\rangle$ (mode O shown by the blue arrow in Fig. 4.18b).

Mode G. At increasing temperatures, the mode G appears in the spectra (see Fig. 4.12). Mode G becomes more and more pronounced with temperature reaching a maximum at around 40 K. Such a temperature dependence is

typical for transitions between excited levels. The populations of these levels are very small at low temperatures and thus the probability of transitions is very small as well. When the temperature increases, the population of the excited levels increases also. The probability of the transitions becomes larger and the absorption intensity increases. The maximum of the mode intensity appears at temperatures equivalent to the zero-field energy gap. The intensity of the mode G exhibits exactly this behavior. Thus, we can conclude that mode G corresponds to the transitions between the spin levels in the excited quadruplet $|ES, -3/2\rangle$, $|ES, -1/2\rangle$, $|ES, 1/2\rangle$, and $|ES, 3/2\rangle$. These transitions are marked by orange arrows in Fig. 4.18b. We obtain $g_{ES} = 2.25$ at 40 K.

The perfect agreement between the g -factor of the G mode measured directly ($g_{ES} = 2.25$), and the g -factor of ES levels calculated from the slope of mode A ($g_{ES} = 2.27$, see calculations above) is remarkable. This agreement strongly supports the assumption that the excited state has a spin degeneracy higher than triplet as claimed in the dimer-monomer model.

The mode B has a gap of $\Delta'_{ES} = 1134$ GHz, the same slope as mode A (Fig. 4.11a), and weak intensity (Fig. 4.9). I assume that the mode B belongs to the same dispersion branch, $E(k)$, as the mode A. I putatively associate the mode B with excitations of this branch at the border of the Brillouin zone. As I mentioned in chapter 3, such transitions are possible when the translational symmetry is broken by some additional (weak) interaction. The intensity of such transitions is usually weak as experimentally observed. A similar mode was found in the spin-dimer system $\text{Ba}_3\text{Cr}_2\text{O}_8$ and discussed in the previous chapter. Thus, $E(0) - E(k) = 90$ GHz at zero field. This value is in agreement with calculations [100] and neutron-scattering results [85] obtained at 14 T where a dispersion of about $\simeq 0.3$ meV = 74 GHz was found.

The experimentally observed ESR spectra (Figs. 4.11 and 4.18a) are described satisfactorily by the energy diagram shown in Fig. 4.18b. The values of the g -factors and gaps are in good agreement with the experimental data.

Next, I will discuss the magnetization and specific heat of azurite in frame of the obtained energy-level diagram (Fig. 4.18b). The magnetization process is going in three steps. First, the doublets GS and ED is split by the magnetic field. The population of the two lowest levels increase and reach a maximum at about H_{c1} . The following increase of the field cannot change the magnetization because only the two lowest levels ($|GS, -1/2\rangle$ and $|ED, -1/2\rangle$) are populated. At H_{c2} , the population of $|ES, -3/2\rangle$ starts to increase. $|ES, -3/2\rangle$ becomes the ground state above H_{c3} and the magnetization reaches saturation. This scenario is in agreement with experiment [72] (Figs. 4.4 and 4.14) and explains the absence of the 2/3 plateau (see also Ref. [101]). The result of our calculations based on the obtained energy-level diagram is shown in Fig. 4.19. Better

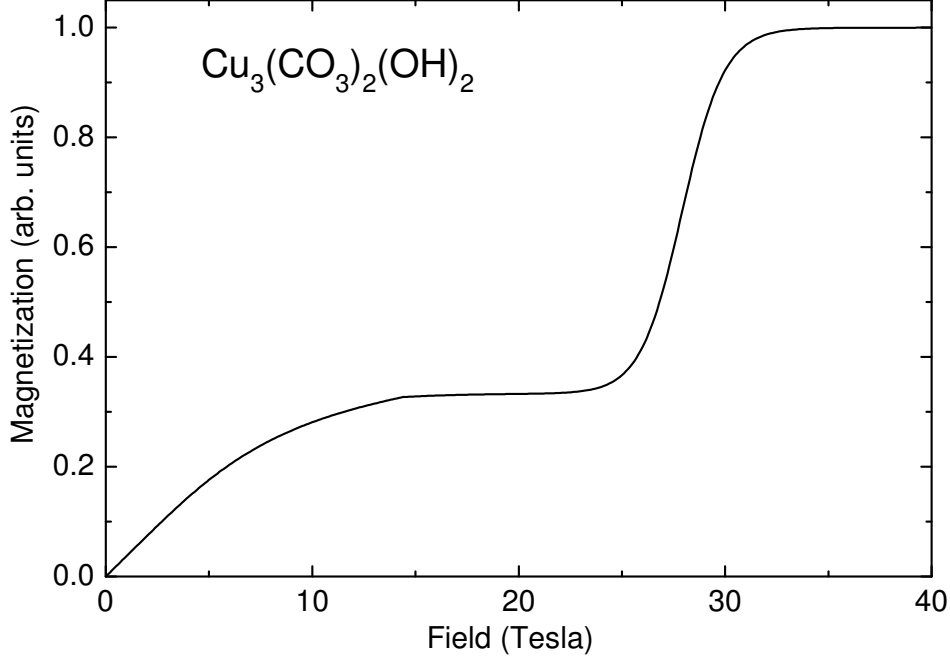


Figure 4.19: Calculated magnetization curve at $T = 1.5$ K.

agreement with the experimental data could be obtained by including additional interactions (J_{dd} , J_m , interchain interaction, DM interactions). As I noted above, largely different sets of J_1 , J_2 , J_3 , and additional J_i parameters can describe the experimental data successfully.

The specific heat as well as the magnetization was measured by Kikuchi *et al.* [72]. The specific-heat data are shown in Fig. 4.20a. The energy-level diagram (Fig. 4.18b) allows to calculate the magnetic contribution to the specific heat [102]. The result of the calculation is shown in Fig. 4.20. Two Schottky anomalies appear at 4 and 18 K. The gap $\Delta_{ED} = 183$ GHz is responsible for the broad maximum at 4 K, the gap $\Delta_{ES} = 1043$ GHz for the maximum at 18 K. In the experiment [72], indeed two anomalies appear at 4 and 18 K. In the calculation, the long-range ordering at $T_N = 1.8$ K and the corresponding fluctuation contribution to the specific heat could not be taken into account.

I should note some drawbacks of such a description. The triangular description explains the crossing from mode A to mode C, but just qualitatively.

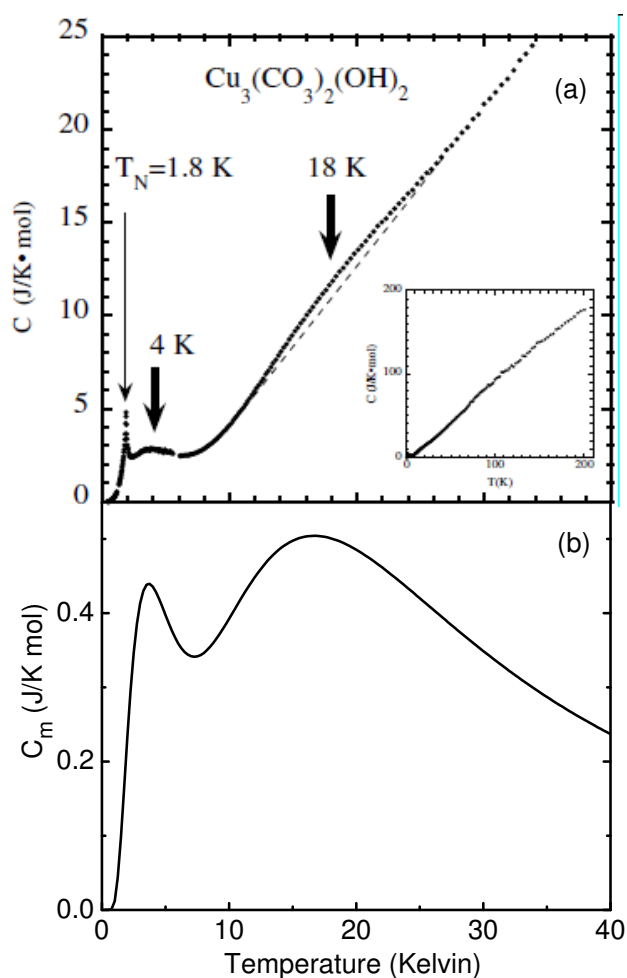


Figure 4.20: Temperature dependence of the specific heat. (a) Experimental data of Kikushi *et al.* [72]. The broken line is a guide for the eyes to better emphasize the anomaly at about 18 K. (b) Calculation of the magnetic contribution to the specific heat based on the proposed energy-level diagram (Fig. 4.18b).

The obtained energy-level diagram would predict such a feature only above 20 T (Fig. 4.18b). However, we observed this feature at 12 T. Also the triangular description cannot explain the different slopes of modes C and E. As well as the dimer-monomer model, the triangular model predicts the same slope for these modes. The main problem is the ground state. The triangular cell itself has a doublet ground state, which contradicts results of magnetic-susceptibility data [72]. This experimental features can qualitatively be explained by including

antiferromagnetic interactions between the triangles. But, for the quantitative explanation additional calculations would be needed.

4.4.4 Six-spin model

Motivated by the good agreement of the calculations with the experimental results one can improve the model. Actually, in the previous subsections, I performed the calculations of the excitation spectra by an exact diagonalization method. I calculated the energy level-diagram for three spins in the azurite network. However, as I already noted, the triangular model cannot reproduce all experimental details. The triangular cell has a doublet ground state. To explain the magnetic-susceptibility results [72], the antiferromagnetic exchange between the triangles should be introduced. However, analysis of the crystallographic structure suggests the value of this interaction to be similar to the interactions inside the triangles. Therefore, introducing such an effective interaction seems somewhat artificial. In this subsection, I make an attempt to provide a more general consideration.

One can consider a six-spin systems in the azurite network (see Fig. 4.1). First of all, such a description has the advantage that the ground state is a singlet which is in agreement with the results of previous investigations [72]. On the other hand, a system of six interacting spins becomes much more complicated and needs sophisticated calculations. I will not concentrate here on the detailed quantum-mechanical solution of this task. I just consider possible states and transitions in the system. I want to show that the method of exact diagonalization may clarify the unusual magnetic properties of azurite.

Taking into account magnetic-susceptibility data [72] and the antiferromagnetic exchange interactions between the spins it could be shown that the ground state has a total spin of $S = 0$. The spin-zero state can be realized by a few spin configurations. Due to the geometric frustration in the network, all pairwise interactions cannot be satisfied. Therefore, the lowest energy corresponds to the spin configuration with unsatisfied lowest exchange interaction J_1 . The ground-state spin configuration is shown in Fig. 4.21a. This state has a total spin $S = 0$ and just one possible spin projection $s_z = 0$. This level is shown by a blue line in Fig. 4.22. Other $S = 0$ configurations have a higher energy.

The first excited state corresponds to the flipping of one spin. Since the exchange interaction J_2 is the strongest, flipping of spins coupled by J_2 costs more energy than flipping other spins. Thus, the first excited state corresponds to the parallel alignment of the spins coupled by J_1 and J_3 . This spins are shown by red in Fig. 4.21. The spin configuration of the first excited state is shown in (Fig. 4.21b). This state has a total spin 1 and, therefore, 3 possible

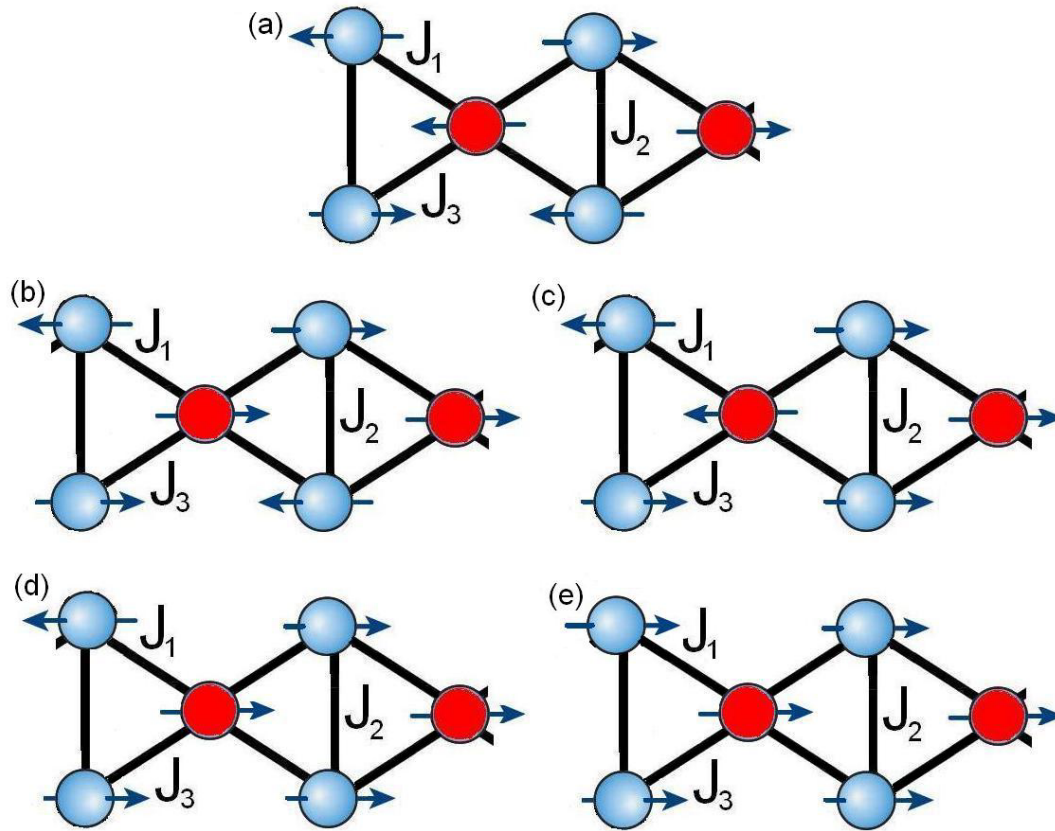


Figure 4.21: Possible spin-configurations of the six-spin diamond-chain system. See text for details.

spin-projection. The levels of this state are shown by green lines in Fig. 4.22. The same total spin has the configuration shown in Fig. 4.21c, but the energy of this state is higher than that shown in Fig. 4.21b because the strongest exchange interaction J_2 is unsatisfied. There are a number of other spin configurations with $S = 1$, but all these configurations have higher energies. Figure 4.22 shows the energy-level diagram of the discussed states. Configuration 4.21b shown by green color, 4.21c shown by red.

The state with $S = 2$ can be realized by a number of configurations as well. The lowest energy has the configuration shown in Fig. 4.21d. In the energy-level diagram, these states with $S = 2$ are shown by purple (Fig. 4.22). Other levels with $S = 2$ are neglected. The state with $S = 3$ corresponds to the alignment of all spins (Fig. 4.21e). These states are shown by brown color in the energy-level diagram (Fig. 4.22).

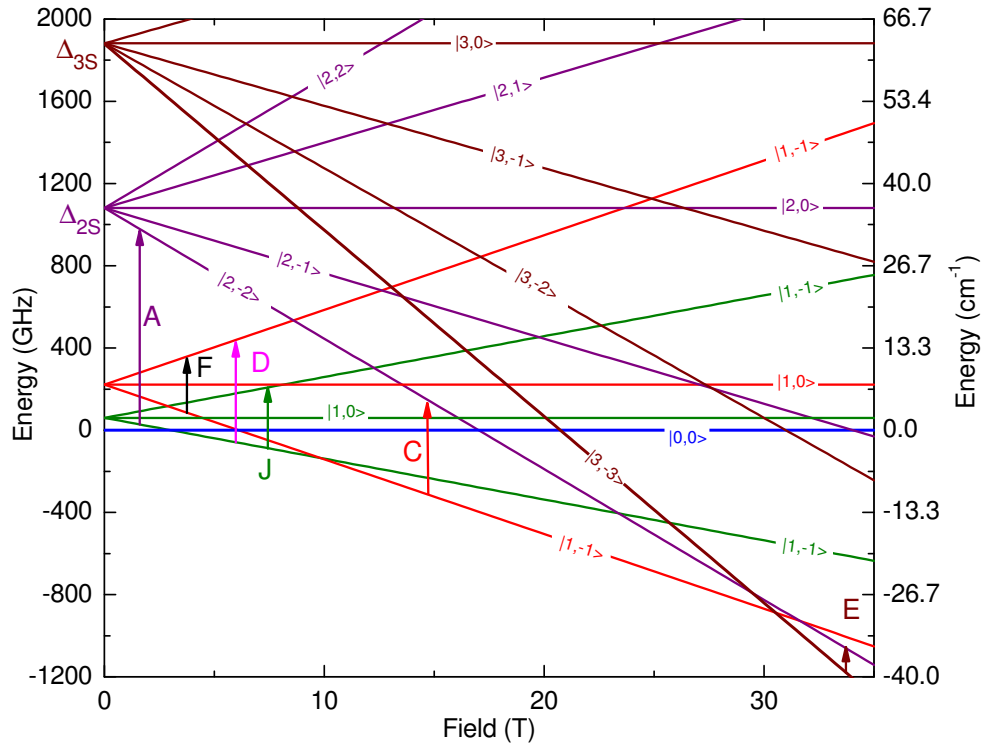


Figure 4.22: Energy-level diagram of the six-spin system. The colors of the arrows correspond to the colors of the modes shown in Fig. 4.11.

Now, possible transitions between these levels shall be discussed. Generally speaking, transitions with a change of the total spin S are forbidden. However, they can be observed under special conditions as discussed previously. By means of ESR, we are able to observe single-particle processes only. For instance, transitions from $S = 0$ to $S = 3$ are not observable. Thus, we can observe transitions with $\Delta S = 1$. Possible transitions are shown by arrows in Fig. 4.22.

It is possible to apply the procedure used for the calculation of the energy-level diagram in subsection 4.4.2 by just changing doublets by triplets. If we consider $\Delta S = 1$ transitions, the expected frequency-field diagram is similar as obtained before. There are a few important features which, however, create differences between the triangular and six-spin model. First, the ground state is a singlet in agreement with the susceptibility data. Second, the crossing of the

field-dependent ground states happens at about 10 T, which better agrees with the observation (12 Tesla). Modes C and E correspond to transitions between different levels. This fact would explain the different slopes of these modes. The broad absorption at frequencies around 1.1 - 1.2 THz observed by means of FIR experiments is caused by a number of level crossings between $S = 2$ and $S = 3$ levels. Thus, we can calculate the parameters for the $S = 3$ states by the procedure as described above. The fit of mode E gives $k_e = 1.95$ and $\Delta = 799$ GHz. Thus,

$$k_E = k_{3S} - k_{2S} = 3g_{3S} - 2g_{es} = 3g_{3S} - 4.52 = 1.95,$$

$$g_{3S} = 2.17,$$

$$\Delta_{3S} = \Delta_{2S} + 799 = 1875 \text{ GHz}.$$

I should admit, the Fig. 4.22 shows a very simplified picture of the energy levels. There are a number of levels with $S = 0$ and $S = 1$ which are not shown in Fig. 4.22. There is also one additional quintet with $S = 2$ in the six-spin system. Since all pairwise exchange interactions are antiferromagnetic, the second quintet has a zero-field energy larger than Δ_{2S} but less than Δ_{3S} . Thus, there are a lot of energy levels between 1 and 2 THz (4.15 – 8 meV). In addition to two quintets with $S = 2$ and seven $S = 3$ levels, there are more singlets, $S = 0$, and triplets, $S = 1$. These levels form broad absorption bands at corresponding frequencies. In my opinion signs of such broad absorptions have been observed by Rule *et al.* by means of INS (Fig. 4.6).

The obtained energy-level diagram shows a high concentration of energy levels between H_{c2} and H_{c3} . This may lead to the large magnetocaloric effect at fields between H_{c2} and H_{c3} . This prediction is in agreement with results of numerical calculations performed by A. Honecker *et al.* [100].

4.5 Conclusion

Detailed investigations of $\text{Cu}_3(\text{CO}_3)_2(\text{OH})_2$ have been performed by means of ESR and FIR spectroscopy over a broad range of frequencies and magnetic fields. I was able to find a number of new modes in the magnetic excitation spectrum. The temperature evolution of the ESR spectra has been studied. The magnetization curve has been measured up to 60 T at different temperatures.

I have shown that the simplified microscopic model of dimers and monomers cannot fully describe all magnetic properties of $\text{Cu}_3(\text{CO}_3)_2(\text{OH})_2$. The rich excitation spectra at low frequencies (two gaps at 0.4 and 0.6 meV shown in Fig. 4.7)

may be caused by the interaction between the dimers and monomers. The influence of such interaction is demonstrated in frame of the triangular and six-spin model description. It can be concluded that the modes F and D are related to bound states of dimers and monomers.

I have calculated the energy-level diagram using the frequency-field dependence of the ESR absorptions and the temperature dependence of the spectra. The obtained energy-level diagram successfully describes not only results of our ESR investigations, but also the results obtained by S. Okubo *et al.* [84]. Additionally, I calculated the magnetic contribution to the specific heat and can explain the origin of the two maxima occurring at 4 and 18 K in the specific heat.

However, as shown by INS experiments, azurite exhibits a much more complicated behavior. This years belongs a few paper discussed 3D behavior [100, 101]. I hope that the results obtained here will motivate further theoretical efforts to find a microscopic model able to fully describe the magnetic properties of azurite.

5 Magnetic excitations in the two-dimensional triangular frustrated spin-system Cs_2CuBr_4

5.1 Introduction

Frustration of magnetic interactions can lead to exotic phenomena in solids as discussed in the introduction. Field-induced phase transitions are an example of such phenomena. Such transitions were observed in a number of quantum magnets with a large diversity of magnetic structures, ranging, for instance, from the simple weakly isolated dimers (TlCuCl_3) [52, 53, 104, 105] to highly frustrated three-dimensional systems with pyrochlore structure ($\text{Ho}_2\text{Ti}_2\text{O}_7$) [40]. Field-induced phase transitions in quantum magnets have recently received a considerable amount of attention, particularly in the context of quantum criticality. In the framework of this thesis we touched this problem already, in previous chapters. Now, I discuss magnetic properties of quasi-two-dimensional triangular spin systems.

Over the last two decades, triangular antiferromagnetic (TAF) systems have been studied extensively for hexagonal ABX_3 -type antiferromagnet (where A is an alkali metal, B is a transition metal, and X is a halogen atom). A number of phases, including field-induced ones, due to the frustration have been found [106]. Within the classical model, the spin structure of a two-dimensional Heisenberg TAF in a magnetic field cannot be determined uniquely, because the number of the parameters that are given by the equilibrium conditions is insufficient for the determination of the spin configuration, and, thus, there remains a non-trivial continuous degeneracy at the ground state [107].

In this chapter, I focus on the magnetic-resonance properties of the $S = 1/2$ TAF Cs_2CuBr_4 . I will compare the obtained results for this compound with the published results for the isostructural compound Cs_2CuCl_4 . Both of these compounds are $S = 1/2$ TAFs, with magnetic Cu^{2+} ions. The crystallographic structures were studied in the middle of the last century [108, 109]. Cesium tetrabromocuprate (II), Cs_2CuBr_4 , has an orthorhombic structure with space

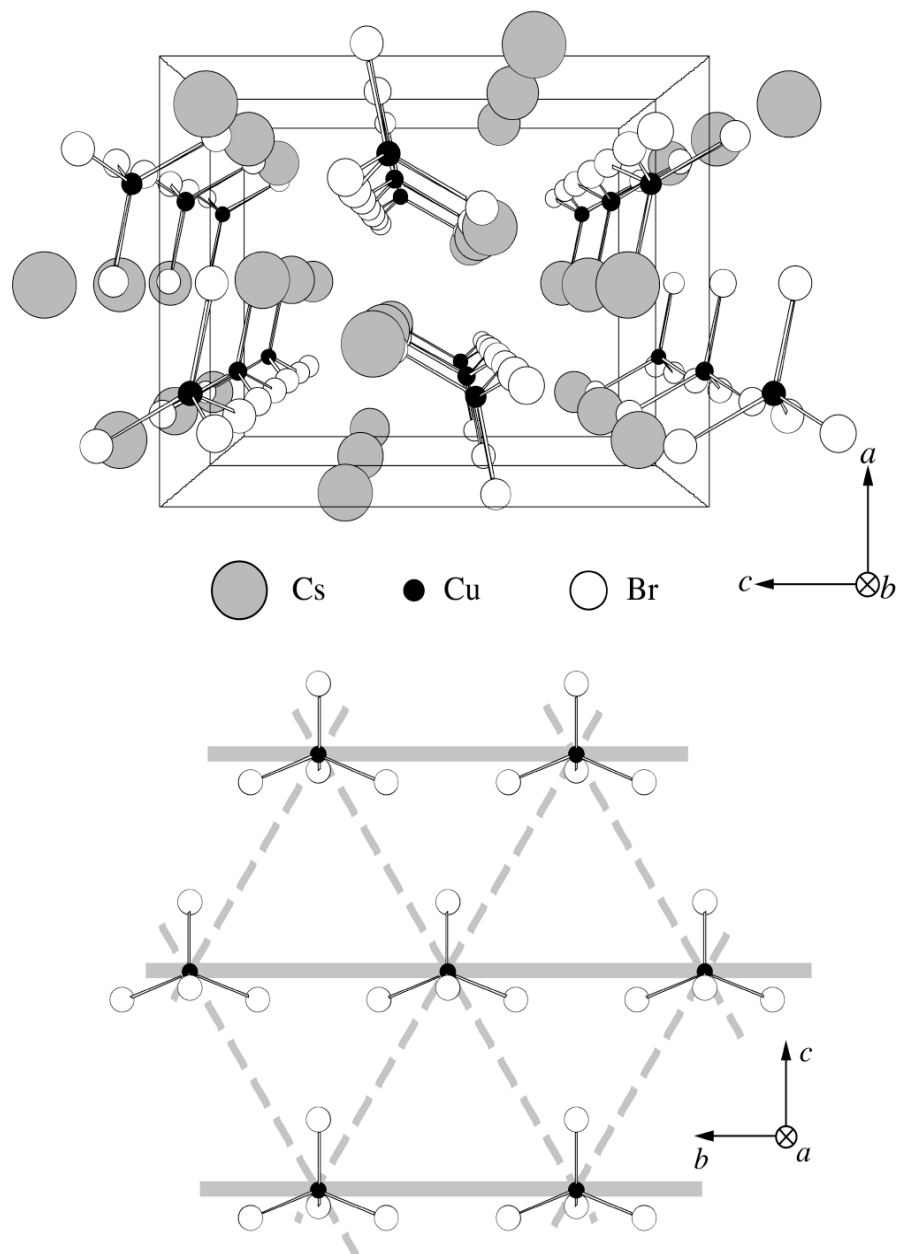


Figure 5.1: (a) Perspective view of the crystal structure of Cs_2CuBr_4 along the b axis. Shaded, closed, and open circles denote Cs^+ , Cu^{2+} , and Br^- ions, respectively. (b) Arrangement of the CuBr_4^{2-} octahedra in the bc plane. Cs^+ ions are omitted. From Ref. [108]

group P_{nma} (D_{16}^{2h}). The lattice constants at room temperature are $a = 10.195 \text{ \AA}$, $b = 7.965 \text{ \AA}$, and $c = 12.936 \text{ \AA}$, with the number of chemical units in the unit cell $Z = 4$ [108]. Figure 5.1a shows a perspective view of the crystal structure along the b axis [110]. Cs_2CuCl_4 has essentially the same structure with somewhat different lattice parameters, namely $a = 9.70 \text{ \AA}$, $b = 7.60 \text{ \AA}$, and $c = 12.35 \text{ \AA}$ [109] at room temperature, and $a = 9.65 \text{ \AA}$, $b = 7.48 \text{ \AA}$, and $c = 12.35 \text{ \AA}$ at $T = 0.3 \text{ K}$ [113, 114].

The magnetic properties of these isostructural compounds have been investigated extensively [110–120]. Cs_2CuCl_4 undergoes a magnetic phase transition at $T_N = 0.62 \text{ K}$. T_N is far below the Curie-Weiss temperature, $\Theta_{CW} = 4 \text{ K}$ [113]. In the ordered phase below T_N , the spins lie in a plane that is almost parallel to the bc plane. The spins form a helical incommensurate structure with ordering vector $\mathbf{Q}_0 = (0, 0.528, 0)$. The incommensurate spin structure arises from the spin frustration on the distorted triangular lattice in the bc plane (Fig. 5.1b). By means of inelastic neutron scattering, it was demonstrated that the exchange interactions J_1 and J_2 are dominant and that the interlayer coupling is significantly smaller than J_1 [114, 116, 117]. Thus, Cs_2CuCl_4 was characterized as a two-dimensional (2D) TAF. Cs_2CuCl_4 realizes a distorted triangular lattice with a strong exchange interaction J_1 along the base of the triangular unit (shown by the solid line in Fig. 5.1b) and a weaker exchange integral, $J_2 = 0.34J_1$, along the lateral sides of the triangle (dashed lines in Fig. 5.1b). The parameters of the Hamiltonian for Cs_2CuCl_4 were determined from measurements of the magnon dispersion in the saturated ferromagnetic phase, $J_1 = 4.3 \text{ K}$, $J_2 = 1.49 \text{ K}$, $J_3 = 0.2 \text{ K}$ (interplane interactions), and $D = 0.23 \text{ K}$ (DM interaction) [117].

It is expected that Cs_2CuBr_4 can be considered as an $S = 1/2$ 2D TAF as well. This was confirmed by means of elastic neutron scattering. Ono *et al.* found the magnetic structure to be incommensurate, with an ordering vector $\mathbf{Q}_O = (0, 0.575, 0)$ at zero field [115]. The exchange constants were found by Tsujii *et al.* to be $J_1 = 11.3 \text{ K}$ and $J_2 = 8.3 \text{ K}$ [118]. This indicates that the spin structure in the ordered phase of Cs_2CuBr_4 is similar to Cs_2CuCl_4 .

In previous investigations on Cs_2CuBr_4 [110, 112, 115], magnetic ordering was found at $T_N = 1.4 \text{ K}$, which is more than a factor of two higher than $T_N = 0.62 \text{ K}$ in Cs_2CuCl_4 . The magnetic susceptibilities of both compounds exhibit similar temperature dependences. Figure 5.2 shows the magnetic susceptibility and the inverse susceptibility of Cs_2CuBr_4 as a function of temperature measured at $H = 1.0 \text{ T}$ for $H \parallel b$. The value of $T_{max} = 9 \text{ K}$ for Cs_2CuBr_4 is three times as large as $T_{max} = 3 \text{ K}$ for the isostructural Cs_2CuCl_4 [111]. This confirms that the exchange interactions in Cs_2CuBr_4 are larger than those in Cs_2CuCl_4 . The broad maximum in the susceptibility is characteristic of the low-dimensional antiferromagnetic spin system. However, the inverse susceptibility of Cs_2CuBr_4 is a con-

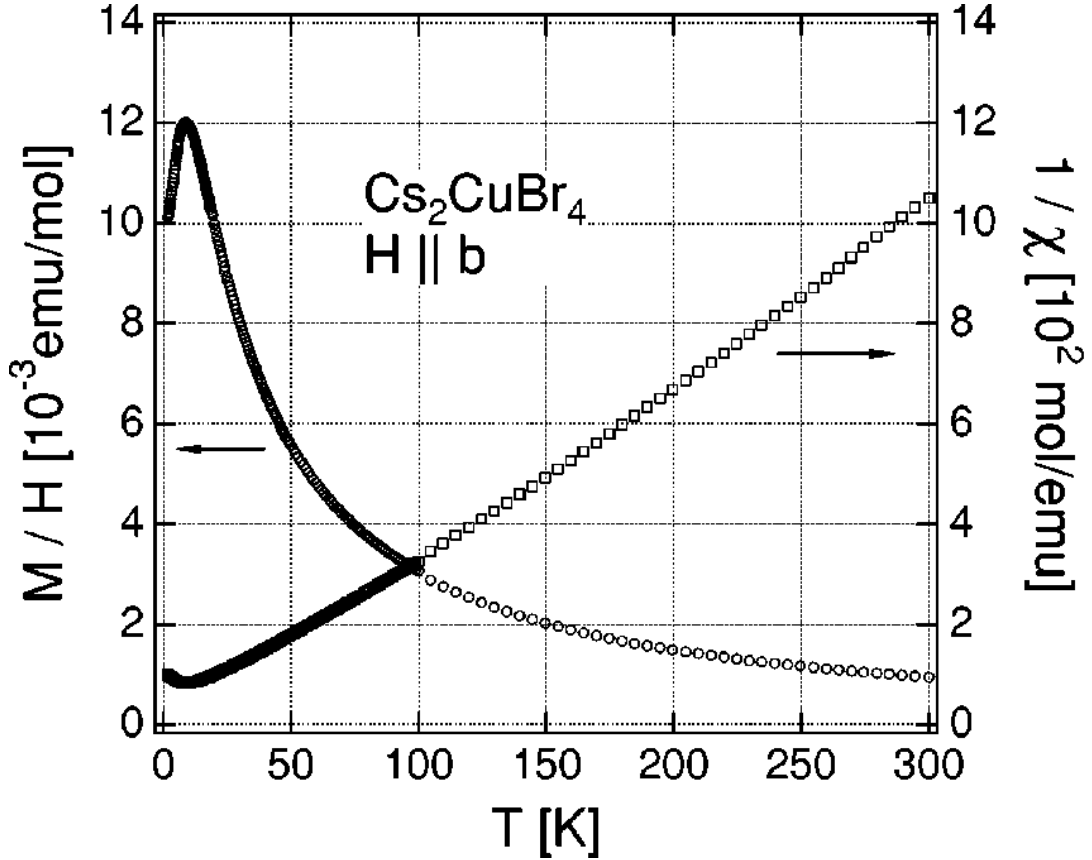


Figure 5.2: Magnetic susceptibility and inverse susceptibility of Cs_2CuBr_4 as a function of temperature for $H \parallel b$. From Ref. [110].

vex function of temperature and has no linear part obeying the Curie-Weiss law. This susceptibility behavior was also observed for $H \parallel a$ and $H \parallel c$ [110]. It was shown before that this effect arises from the contribution of the excited orbital states of Cu^{2+} ions which suppresses the effective magnetic moment [110].

However, one can compare the degree of frustration in Cs_2CuBr_4 and Cs_2CuCl_4 by an other way. The degree of frustration for a 2D triangular lattice is maximum in case $J_2/J_1 = 1$ and there is no frustration in case $J_2/J_1 = 0$ (for a $S = 1/2$ AFM chain). Thus, one can use ratio J_2/J_1 as frustration parameter for the 2D TAFs. Since the relation J_2/J_1 is smaller for Cs_2CuBr_4 , this compound is more frustrated. Detailed theoretical investigations of the temperature dependence of the magnetic susceptibility for TAFs have been done by Zheng *et al.* [119].

The interesting feature of Cs_2CuBr_4 is the $1/3$ magnetization plateau observed for magnetic fields aligned along the b and c axes at temperatures below $T_N =$

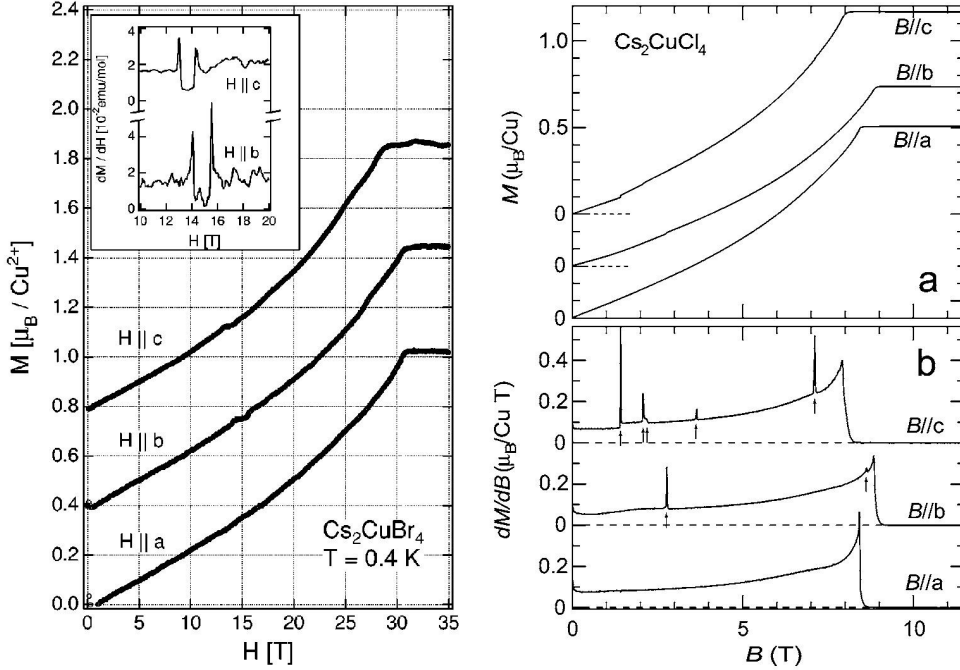


Figure 5.3: Left: Magnetization of Cs_2CuBr_4 as a function of external field applied along the a , b , and c axes. Measurements were performed at $T = 400$ mK. The magnetization curves are consecutively shifted by $0.4\mu_B$. The inset shows dM/dH vs H around the magnetization plateaus for $H \parallel b$ and $H \parallel c$ [110]. Right: (a) Magnetization curves for Cs_2CuCl_4 measured at the base temperature for the field applied along the three crystallographic axes. The curves for $H \parallel b$ and $H \parallel c$ are shifted by 0.3 and $0.6 \mu_B/\text{Cu}$, respectively. (b) Susceptibility dM/dB vs field [120].

1.4 K, while no plateau is observed for $H \parallel a$. The magnetization data obtained at $T = 400$ mK in magnetic fields up to 35 T by Ono *et al.* are shown in the left panel of Fig. 5.3. On the other hand, no plateau is observed for Cs_2CuCl_4 (Fig. 5.3, right panel) [120].

Four critical fields can be extracted from the magnetization curves of Cs_2CuBr_4 . $H_{c1} \simeq 13.1$ T, $H_{c2} \simeq 14.4$ T for $H \parallel c$ and $H_{c1} \simeq 14.0$ T, $H_{c2} \simeq 15.3$ T for $H \parallel b$. Slightly lower critical fields of $H_{c1} \simeq 12.9$ T, $H_{c2} \simeq 14.4$ T for $H \parallel c$ were obtained from magnetocaloric-effect data [118].

Numerical diagonalization of finite-size $S = 1/2$ Heisenberg systems predicts that the geometric frustration is sufficient to stabilize the UUD plateau phase

only in the range $0.7 \leq J_2/J_1 \leq 1.3$ [121] explaining its presence in Cs₂CuBr₄ and absence in Cs₂CuCl₄.

Recently, the temperature-field phase diagram of Cs₂CuBr₄ has been studied by means of magnetization, magnetic susceptibility, specific heat [110], elastic neutron scattering [115], and magnetocaloric-effect measurements [118, 122].

In 2009, Fortune *et al.* reported a phase diagram of Cs₂CuBr₄ with a cascade of field-induced quantum phase transitions [122]. The phase diagram was determined by precise measurements of the magnetocaloric effect and the magnetic torque. Figure 5.4 shows the results of these investigations.

ESR measurements of Cs₂CuCl₄ at high temperatures (77 – 300 K) have been reported by Sharnoff [123, 124]. The g -values were estimated to be 2.08, 2.11, and 2.38 for the c , b , and a directions, respectively. The magnetic excitations in Cs₂CuCl₄ at low-temperatures were studied by means of ESR very recently [125–127].

Povarov *et al.* reported the opening of a zero-field gap in the excitation spectra at temperatures well above T_N [126]. The evolution of the ESR spectra at low temperatures is a result of the influence of uniform DM interaction.

Systematic studies of the magnetic-excitation spectra of Cs₂CuBr₄ by tunable-frequency ESR measurements in the frequency range up to 500 GHz have been performed over a broad range of temperatures. I used the results of these measurements to analyze the DM interaction. I also compare the obtained results with ESR data of M. Sharnoff [123, 124], J. M. Schrama [125], K. Povarov, and A. Smirnov *et al.* [126, 127].

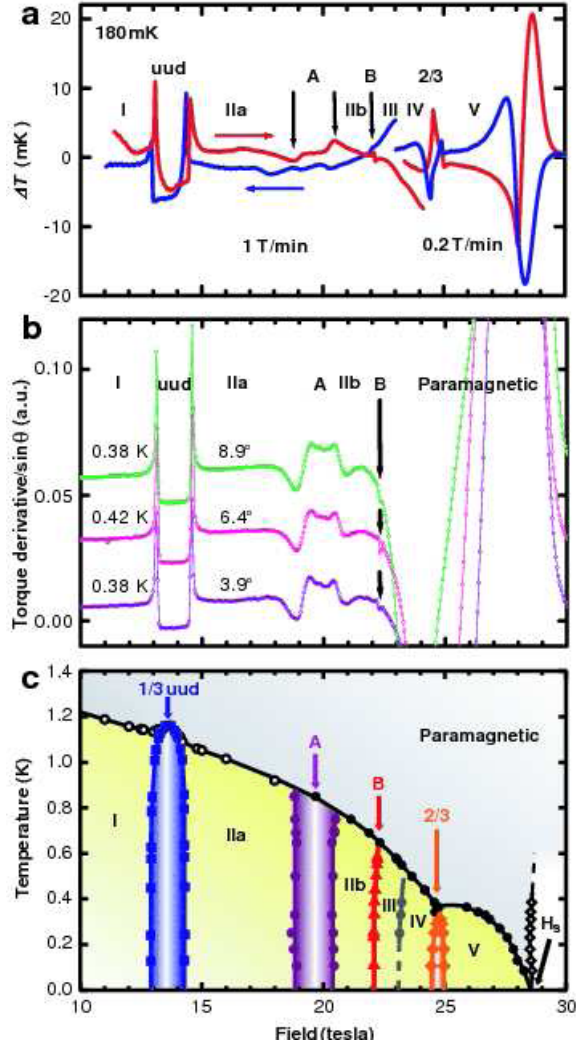


Figure 5.4: (a) Evolution of the temperature difference between Cs_2CuBr_4 sample and thermal reservoir due to the magnetocaloric effect at 180 mK, with arrows indicating the field-sweep directions. (b) Derivative of the magnetic torque with respect to H at temperatures near 400 mK. To produce a torque, the magnetic field was tilted away from the c towards the b axis, by the angle indicated for each curve. (c) Magnetic phase diagram for Cs_2CuBr_4 deduced from the magnetocaloric-effect data. Circles indicate second-order phase boundaries, whereas other symbols except the open diamonds indicate first-order boundaries. Open diamonds are the positions of the large features near H_s and do not indicate a phase boundary. Lines are guides to the eye. Data for $H \leq 18$ T are from Ref. [118], where open circles are from specific heat. From Ref. [122].

5.2 Experimental details

Cs₂CuBr₄ single-crystals with typical sizes of 0.5 mm³ were used. The crystals were synthesized by the slow evaporation of aqueous solution of CsBr and CuBr₂ [110]. Powder X-ray diffraction spectra of the ground samples were taken with Cu K_α radiation of a Rigaku Miniflex X-ray machine. Samples with a typical sizes 2 × 2 × 1 mm³ were oriented and cut with accuracy better than ±3°. ESR experiments have been done over a broad range of temperatures (1.35 – 80 K) using the tunable-frequency spectrometer operating in combination with the 16 T superconducting magnet as described in Chapter 2. The magnetic field was applied along the *a*, *b*, and *c* axes in Faraday geometry (propagation vector $\mathbf{k} \parallel H$). Backward wave oscillators and VDI microwave sources were used to generate the sub-THz radiation.

5.3 Results and discussion

At low temperatures, the ESR spectra of Cs₂CuBr₄ are strongly dependent from the microwave frequency and the magnetic-field orientation. For magnetic fields aligned along the *c* axis (perpendicular to the base of the triangular unit), two resonance modes have been found at 1.35 K. A significant temperature evolution of the ESR spectrum has been observed. There is a single resonance line at temperatures above 20 K. On cooling below 10 K, a second resonance mode appears. The observed temperature evolution of the ESR spectra between 1.3 and 9.2 K at the microwave frequency of 259 GHz is shown in Fig. 5.5. A similar temperature dependence of ESR spectra was reported by Schrama [125] and Povarov [126] for Cs₂CuCl₄. The additional mode in the ESR spectra of Cs₂CuCl₄ appears at temperatures below 2 K ($T_N = 0.62$ K).

The frequency-field dependence of the ESR spectra has been investigated at 1.4 K. The results obtained for $H \parallel c$ are shown in Fig. 5.6. There are two modes in the excitation spectrum. The mode labeled B in Fig. 5.6 shows a linear field dependence. The linear fit of the experimental data, constrained to run through the origin, results in $g = 2.2$ (black line in Fig. 5.6).

The mode labeled A in Fig. 5.6 has a zero-field gap of $\Delta = 200$ GHz (9.6 K). At low magnetic fields, this mode deviates from linearity which is quite uncommon. To make this feature clearer, the dashed red line with the same slope as for mode B is plotted in Fig. 5.6. The observed curvature, at low fields may be due to a single-ion or other kind of anisotropy. As I discussed in the introduction, any small perturbation can lead to different magnetic properties of frustrated systems.

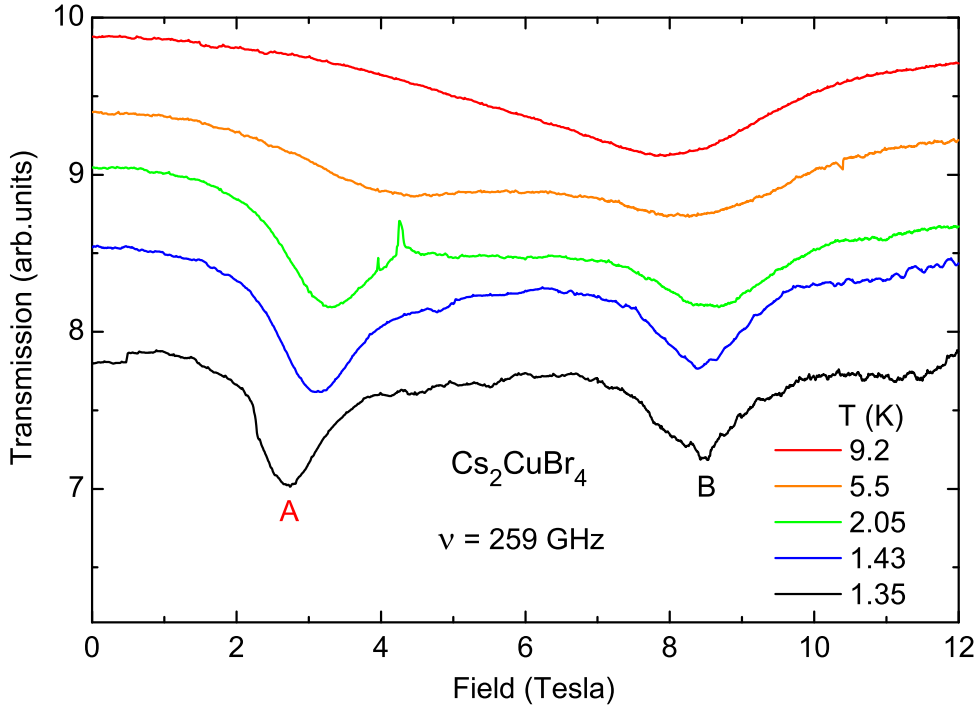


Figure 5.5: ESR spectra of Cs_2CuBr_4 at different temperatures for $H \parallel c$ and $\nu = 259$ GHz.

When the external magnetic field is aligned parallel to the b axis (along the base line of the triangle), a single resonance peak has been observed at temperatures up to 80 K. This line shifts upon cooling to lower fields. The measured frequency-field diagram for $H \parallel b$ at 1.4 K is shown in Fig. 5.7. At this temperature, the mode has a zero-field gap of $\Delta = 200$ GHz in agreement with the results for $H \parallel c$. The magnetic-field dependence of this mode is similar to the mode A for $H \parallel c$. With increasing field the mode approaches a linear field dependence above about 7 T. However, the slope of the linear dependence, corresponding to $g = 1.6$ (red line in Fig. 5.7) is considerably smaller than $g = 2.2$ for the mode A at $H \parallel c$. Remarkably, the linear extrapolations of the gapped mode A for $H \parallel b$ and $H \parallel c$ to zero field leads to the same value of $\Delta' = 135$ GHz.

When the external magnetic field is aligned parallel to the a axis (perpendicular to the plane of the triangular unit), two modes in the excitation spectra appear (Fig. 5.8). The mode labeled A in Fig. 5.8 has a gap of $\Delta = 200$ GHz in agreement with the data for the other orientations. But, at $H \parallel a$ the mode A

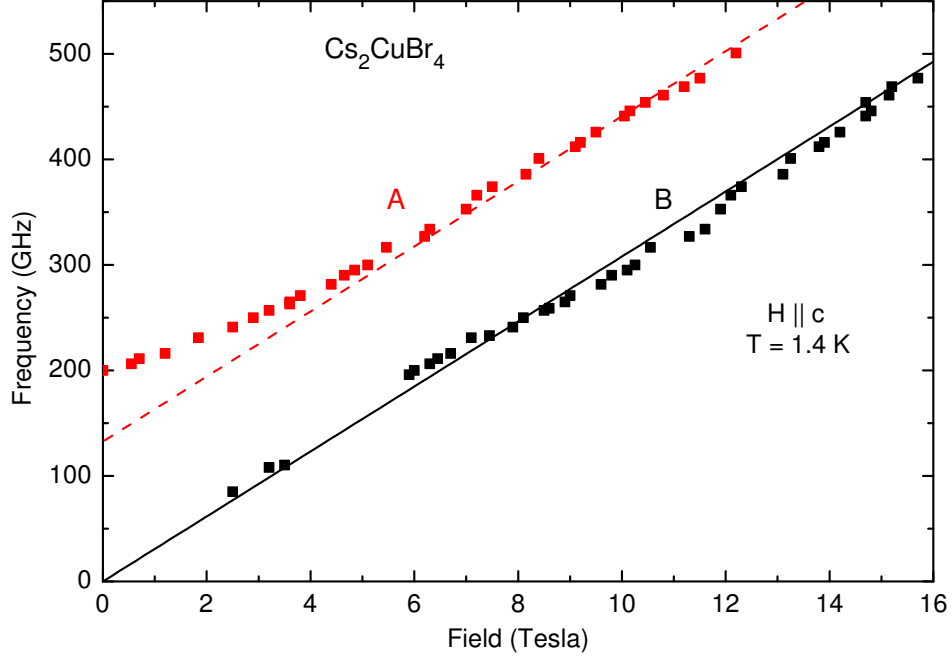


Figure 5.6: The frequency-field diagram for $H \parallel c$ at $T = 1.4$ K. The solid black line is a linear fit to the data of mode B. The red line is a guide for the eyes to make a feature at low fields clearer. The slope of both lines is identical.

does not show any deviation from a linear behavior, unlike the modes A for $H \parallel c$ and b . The slope corresponds to $g = 1.8$.

The mode B shows a very unusual behavior. This mode appears at high magnetic fields only and has a slope which corresponds to effective $g_{eff} = 2.5$.

The gap in the excitation spectra of the mode A was observed in Cs_2CuCl_4 as well [125, 126]. In the case of Cs_2CuCl_4 , the zero-field gap ($\Delta \approx 25$ GHz) was explained by the presence of uniform DM interaction [126, 127]. The value of the gap induced by DM interaction is given by the formula [126]:

$$\Delta/(2\pi\hbar) = \sqrt{D_a^2 + D_c^2}/(4\hbar). \quad (5.1)$$

Performing the same analysis for Cs_2CuBr_4 results in a DM interaction strength larger than J_1 . The DM interaction is the second term of the expansion and according to (Eq. 1.8) should be one order of magnitude smaller

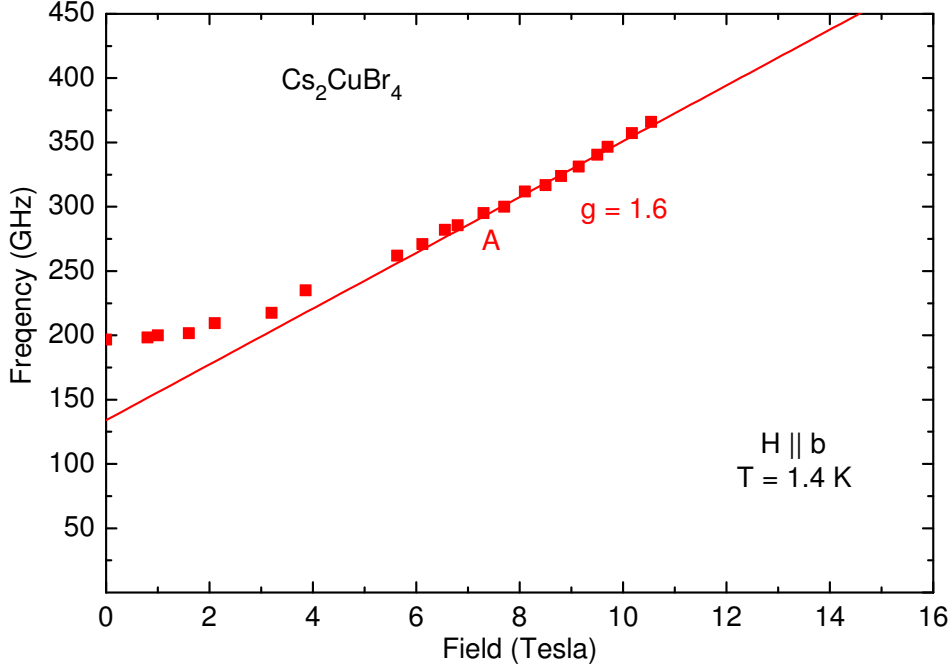


Figure 5.7: Frequency-field diagram for $H \parallel b$ at $T = 1.4$ K.

than the main exchange interaction J_1 . Thus, in case of Cs_2CuBr_4 some other interactions play an important role in the formation of the zero-field gap.

The temperature dependence of the ESR spectra for $H \parallel b$ has been studied. The resonance peak positions and the linewidth have been investigated at a microwave frequency of 295.2 GHz. The obtained results are shown in Fig. 5.9. The temperature dependence of the absorption peak for $H \parallel b$ is comparable to the behavior observed for the mode A for $H \parallel c$ (see Fig. 5.6). At temperatures below 20 K, the ESR absorption line shifts rapidly to lower fields (Fig. 5.9a). The temperature dependence of the linewidth shows a maximum at around 10 K (Fig. 5.9a). It is known, that ESR lines undergo critical broadening at temperatures near phase transitions. For low-dimensional systems without frustration, the maximum of the linewidth coincides with the Neel temperature [128]. However, for Cs_2CuBr_4 frustrations suppresses ordering. Remarkably, the temper-

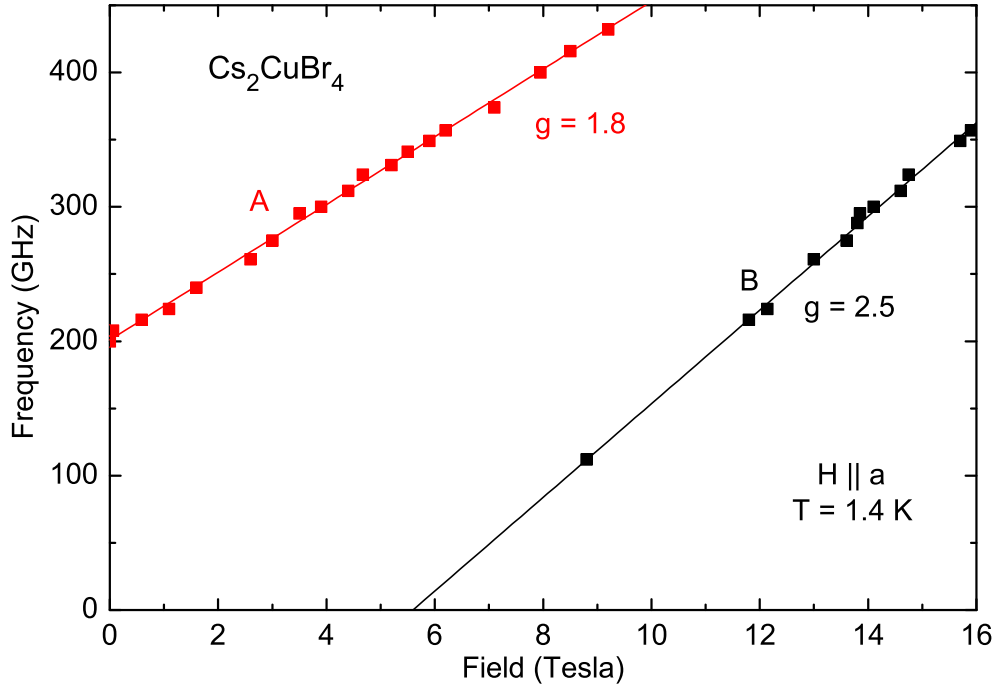


Figure 5.8: The frequency-field diagram for $H \parallel a$ at $T = 1.4 \text{ K}$. The solid red and black lines are linear fits to the data for mode A and mode B, respectively.

ature of the maximal linewidth is close to the maximum of the susceptibility ($T_{max} = 9 \text{ K}$, see Fig. 5.2).

At temperatures above 50 K, ESR signals with single lines corresponding to g -factors values $g_a = 2.2$, $g_b = 2.11$, and $g_c = 2.25$ were detected for magnetic fields applied parallel to the a , b and c axes respectively. At temperatures above 80 K, the intensity of the ESR absorption is diminishes and resonance peaks become unobservable.

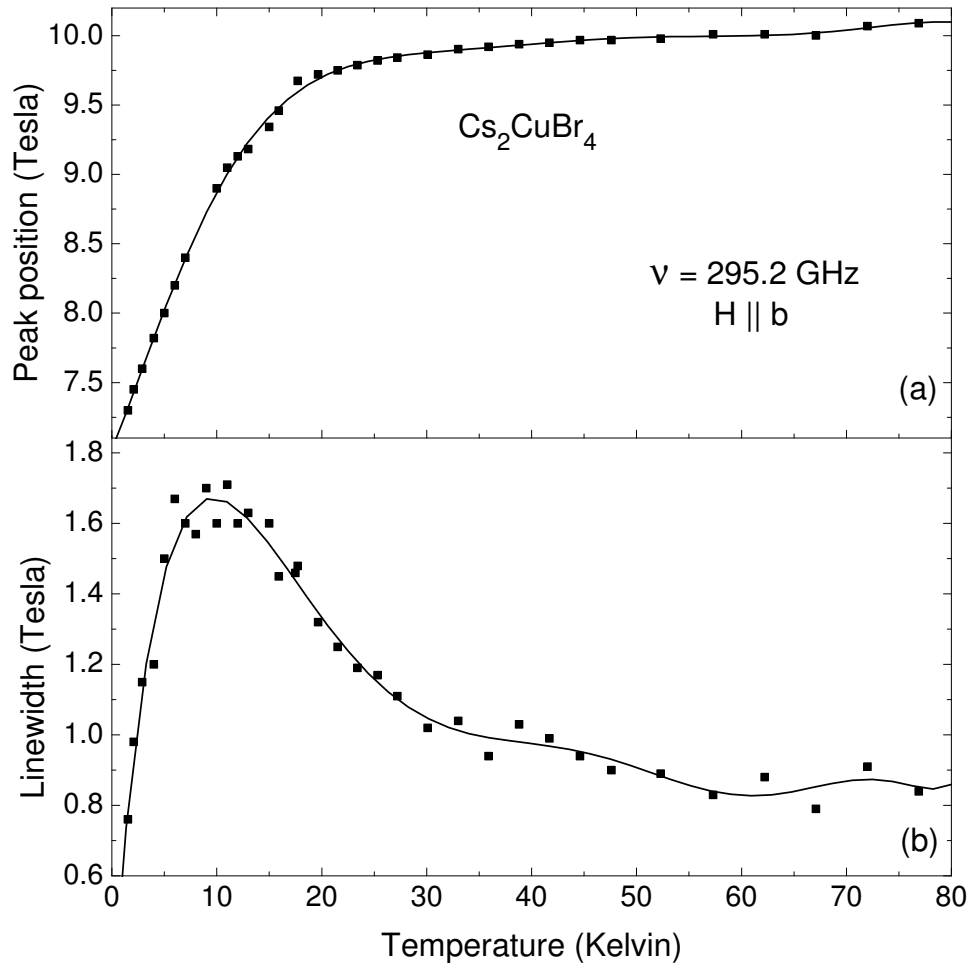


Figure 5.9: (a) Temperature dependence of the resonance field and (b) of the linewidth for $H \parallel b$ and $\nu = 295.2$ GHz. The solid lines are guides for the eyes.

5.4 Conclusions

The results of the ESR measurements of Cs₂CuBr₄ can be summarized as follows. Detailed investigations of ESR spectra of Cs₂CuBr₄ over a broad range of frequencies, magnetic fields, and temperatures have been performed. So far not reported zero-field gap in the excitation spectra of 200 GHz has been found at 1.4 K. At temperatures approaching (but still above) the ordering temperature ($T_N = 1.4$ K), clear indications for short-range-order correlations could be observed. Starting at about 20 K, the peak position shifts to lower fields (gap opening). At about 10 K, the linewidth of the ESR absorption peak for $H \parallel b$ shows a maximum.

The temperature at which the additional gapped mode appears is close to the maxima in the magnetic susceptibility for both systems (10 K for Cs₂CuBr₄ and 3 K for Cs₂CuCl₄). Both features indicate the increasing role of spin-spin correlations and short-range order. Additionally, critical broadening of the ESR absorptions has been observed at 10 K for Cs₂CuBr₄. Thus, we can conclude that short-range-order correlations arise at about 10 K in Cs₂CuBr₄. The short-range-ordered phase exists over a quite broad temperature region of $\approx 7 T_N$, which is larger than typically for quasi-2D systems ($2 - 3 T_c$ [129]). Thus, the system undergoes an additional suppression of T_N due to frustration of exchange interactions.

In case of Cs₂CuCl₄, the opening of the gap above T_N was explained by the presence of a uniform DM interactions [126]. However, application of the same analysis as in Ref. [126] for Cs₂CuBr₄ gives a value of the DM interaction close to J_1 . Since the DM interaction is a second-order term in the magnetic-exchange interaction it should be significantly smaller than the highest exchange interaction J_1 (Eq. 1.8). Thus, in case of Cs₂CuBr₄, some other mechanism is supposed to be responsible for the formation of the measured zero-field gap.

6 Summary

This thesis is devoted to the study of magnetic-excitation spectra of geometrically frustrated spin systems by means of high-field electron spin resonance. Three different frustrated systems with reduced dimensionality have been studied; namely, the weakly coupled spin-dimer system $\text{Ba}_3\text{Cr}_2\text{O}_8$, the spin-1/2 chain material with distorted diamond structure $\text{Cu}_3(\text{CO}_3)_2(\text{OH})_2$ (natural mineral azurite), and the quasi-two-dimensional antiferromagnet with triangular spin structure Cs_2CuBr_4 .

After an introduction to the basic concepts of frustrated systems, some general magnetic properties of systems with competing interactions are discussed. Magnetically frustrated systems on a regular lattice, or geometrically frustrated magnets are worthwhile to study, since we can investigate the influence of frustration on the physical properties, not being worried by the effect of randomness, which is inevitable in a spin-glass systems. Frustrated systems may have degenerated ground states. In the most extreme cases, a system can have a disordered ground state with macroscopic degeneracy. Thus, any small perturbation may have a strong effect on the ground-state properties. As an example of such a perturbation, the Dzyaloshinskii-Moriya interaction is briefly introduced.

The following chapter describes the basic concepts of ESR absorption and different experimental realizations of ESR measurements. Multi-frequency ESR techniques combined with high magnetic fields allow detailed studies of low-energy excitation spectra. ESR is one of the most powerful methods to study magnetic excitations in the low-energy region (10–1000 GHz or 0.3–33.3 cm^{-1}). I report on the development of a cantilever-based spectrometer for the torque detection of ESR absorption. Other kinds of ESR spectrometers available at HLD, including high-field spectrometers, are discussed as well.

In chapter 3, the resonance properties of the spin-dimer system $\text{Ba}_3\text{Cr}_2\text{O}_8$ are discussed. Two pairs of gapped modes corresponding to transitions from a spin-singlet ground state to the first excited triplet state with zero-field energy gaps, 19.1 and 27 K, were observed. The observation of the ground-state excitations clearly indicates the presence of a non-secular term allowing these transitions to occur. These findings are of crucial importance for a possible interpretation of the field-induced transitions in this material (with critical fields $H_{c1} = 12.5$ T and $H_{c2} = 23.6$ T) in terms of the magnon Bose-Einstein condensation.

In chapter 4, the magnetic properties of the copper mineral azurite with diamond-chain structure are discussed. The natural mineral azurite, $\text{Cu}_3(\text{CO}_3)_2(\text{OH})_2$, has been studied in magnetic fields up to 50 T, revealing several modes, not observed previously. This compound has attracted great interest after Kikushi and co-authors reported a plateau in the magnetization curve [72]. Detailed investigations have been performed by means of ESR and FIR spectroscopy in a broad range of frequencies and magnetic fields (up to 50 T). I observed a few new modes in the magnetic excitation spectrum. The temperature evolution of the ESR spectra has been studied as well. Based on the obtained results, I discuss different microscopic models which are able to describe the magnetic properties.

Chapter 5 is devoted to the systematic studies of the $S = 1/2$ system Cs_2CuBr_4 with triangular 2D spin structure. A substantial zero-field energy gap, $\Delta = 9.6$ K, has been observed in Cs_2CuBr_4 well above the ordering temperature, $T_N = 1.4$ K. It is argued that contrary to the case of the isostructural Cs_2CuCl_4 , the size of the gap cannot be explained solely by the uniform Dzyaloshinskii-Moriya interaction, but it is rather the result of the geometric frustration stabilizing the spin-disordered state in Cs_2CuBr_4 in close vicinity to a quantum phase transition between a spiral magnetically ordered state and a 2D quantum spin liquid.

A few general features of frustrated systems with reduced dimensionality have been observed. First of all, gapped modes in the ESR spectra which are connected with the short-range order have been observed in all studied compounds; such modes are present at temperatures well above T_N . It was shown that short-range-ordered phases exist over broad temperature ranges. The temperature range of short-range ordering is larger than typically for quasi-low-dimensional systems without frustrations. Also the linewidth of the ESR absorption lines for frustrated system are typically larger than for classical paramagnetic compounds. For instance, the linewidth for the typical paramagnet $\text{CuSO}_4 \cdot 5\text{H}_2\text{O}$ is about 0.05 T (see Fig. 2.10) while the linewidth of the ESR absorption in $\text{Ba}_3\text{Cr}_2\text{O}_8$ is about 1 T for the gapped mode.

Bibliography

- [1] S. T. Bramwell and M. J. P. Gingras, *Science* **254**, 1495 (2001).
- [2] L. Balents, *Nature* **464**, 199 (2010).
- [3] S. Sachdev, *Nature Phys.* **4**, 173-185 (2008).
- [4] A. P. Ramirez, *Annu. Rev. Mater. Sci.* **24**, 453 (1994).
- [5] G. H. Wannier, *Phys. Rev.* **79**, 357-364 (1950).
- [6] G. Toulouse, *Commun. Phys.* **2**, 115 (1977).
- [7] P. W. Anderson, *Phys. Rev.* **102**, 1008 (1956).
- [8] D. Harshman, G. Aeppli, G. P. Espinosa, A. S Cooper, J. P. Remeika, E. J. Ansaldo, T. M. Riseman, D. L. Williams, D. R. Noakes, B. Ellman, and T. F. Rosenbaum, *Phys. Rev. B* **38**, 852-55 (1988).
- [9] J. S. Smart, *Effective Field Theories of Magnetism*, W. B. Saunders (1966).
- [10] J. B. Goodenough, J. M. Longo, *Crystallographic and Magnetic Properties of Perovskite and Perovskite – related Compounds, Landolt – Borstein III/4a*, Springer-Verlag, Berlin, p.228 (1970).
- [11] R. Moessner and J. T. Chalker, *Phys. Rev. B* **58**, 12049 (1998).
- [12] L. J. Dejongh and A. R. Miedema, *Advances in Physics* **23**, 1-260 (1974).
- [13] N. D. Mermin and H. Wagner, *Phys. Rev. Lett.* **17**, 1133-1136 (1966).
- [14] J. Villain, *Z. Phys. B*, **33**, 31 (1979).
- [15] J. E. Greedan, *J. Mater. Chem.* **11**, 37-53 (2001).
- [16] D. G. Tomuta, S. Ramakrishnan, G. J. Nieuwehuys, and J. A. Mydosh, *Jour. Phys. Cond. Matt.* **13**, 4543 (2001).
- [17] T. A. Kaplan and N. Menyuk, *Philosophical Magazine*, **87**, 3711 (2007).
- [18] A. Tauber, W. M. Moller, and E. Banks, *J. Solid. State Chem.* **4**, 138 (1972).
- [19] A. P. Ramirez, G. P. Espinosa, and A. S. Cooper, *Phys. Rev. B* **45**, 2005 (1992).

- [20] J. S. Helton, K. Matan, M. P. Shores, E. A. Nytko, B. M. Bartlett, Y. Yoshida, Y. Takano, A. Suslov, Y. Qiu, J.-H. Chung, D. G. Nocera, and Y. S. Lee, *Phys. Rev. Lett.* **98**, 107204 (2007).
- [21] S. Vilminot, G. Andre, and M. Kurmoo, *Inorg. Chem.* **48**, 2687-2692 (2009).
- [22] H. Martinho, N. O. Moreno, J. A. Sanjurjo, C. Rettori, A. J. García-Adeva, D. L. Huber, S. B. Oseroff, W. Ratcliff, S.-W. Cheong, P. G. Pagliuso, J. L. Sarrao, and G. B. Martins, *Phys. Rev. B* **64**, 024408 (2001).
- [23] A. V. Pronin, M. Uhlarz, R. Beyer, T. Fischer, J. Wosnitza, B. P. Gorshunov, G. A. Komandin, A. S. Prokhorov, M. Dressel, A. A. Bush, and V. I. Torgashev, *Phys. Rev. B* **85**, 012101 (2012).
- [24] V. Fritsch, J. Hemberger, N. Büttgen, E.-W. Scheidt, H.-A. Krug von Nidda, A. Loidl, and V. Tsurkan, *Phys. Rev. Lett.* **92**, 116401 (2004).
- [25] O. Tchernyshyov, R. Moessner, and S. L. Sondhi, *Phys. Rev. Lett.* **88**, 067203 (2002).
- [26] M. Alba, J. Hammann, C. Jacoboni, C. Pappa, *Phys. Lett.* **89**, 423 (1982).
- [27] S. Hov, H. Bratsberg, and A.T. Skjeltorp, *J. Magn. Magn. Mat.* **15-18**, 455 (1980).
- [28] R. Liebmann, *Statistical Mechanics of Periodic Frustrated Ising Systems*, Springer-Verlag, Berlin/New York (1986).
- [29] L. Neel, *Annales de Physique*, **3**, 137 (1948).
- [30] X. Obradors, A. Labarta, A. Isalgue, J. Tejada, J. Rodriguez, and M. Pernet, *Solid State Comm.* **65**, 189-192 (1988).
- [31] B. Martinez, F. Sandiumenge, A. Rouco, A. Labarta, J. Rodríguez-Carvajal, M. Tovar, M. T. Causa, S. Galí, and X. Obradors, *Phys. Rev. B* **46**, 10786-92 (1992).
- [32] A. P. Ramirez, G. P. Espinosa, and A. S. Cooper, *Phys. Rev. Lett.* **64**, 2070 (1990).
- [33] A. P. Ramirez, B. Hessen, and M. Winkelman, *Phys. Rev. Lett.* **84**, 2957 (2000).
- [34] T. Moriya, *Phys. Rev.* **120**, 91 (1960).
- [35] I. Dzyaloshinskii, *Sov. Phys. JETP* **5**, 1259 (1957).
- [36] A. P. Ramirez, A. Hayashi, R. J. Cava, R. Siddharthan, and B. S. Shastry, *J. Appl. Phys.* **399**, 333 (1999).
- [37] M. Elhajal, B. Canals, and C. Lacroix, *Phys. Rev. B* **66**, 014462 (2002).
- [38] C. Broholm, G. Aeppli, G.P. Espinosa and A.S. Cooper, *Phys. Rev. Lett.* **65**, 3173 (1990).
- [39] A. Zorko, S. Nellutla, J. van Tol, L.C. Brunel, F. Bert, F. Duc, J.-C. Trombe, M. A. de Vries, A. Harrison, and P. Mendels, and D. Arcon, *Phys. Rev. Lett.* **101**, 026405 (2008).

-
- [40] J. S. Gardner, M. J. P. Gingras, and J. E. Gridan, *Rev. Mod. Phys.* **82**, 53 (2010).
- [41] R. P. Feynman and R. B. Leighton, M. Sands, *The Feynman Lectures on Physics* Vol. 3, Addison-Wesley (1965).
- [42] A. Abraham and B. Blini, *Electron Paramagnetic Resonance of Transition Ions*, Dover publications inc., New York (1986).
- [43] S. Zherlitsyn, A. Bianchi, T. Herrmannsdörfer, F. Pobell, Y. Skourski, A. Sytcheva, S. A. Zvyagin, and J. Wosnitzer, *IEEE Trans. Appl. Supercond.* **16**, 1660 (2006).
- [44] M. M. Mola, S. Hill, P. Goy, and M. Gross, *Rev. Scien. Instr.*, **71**, 103903 (2008).
- [45] H. H. Meinke and F. W. Gundlach, *Taschenbuch der Hochfrequenztechnik Band II : Komponenten*, Springer Berlin Heidelberg, Berlin (1992).
- [46] S. A. Zvyagin, J. Krzystek, P. H. M. van Loosdrecht, G. Dhalenne, and A. Revcolevschi, *Physica B* **346-347**, 1 (2004).
- [47] E. Ohmichi, N. Mizuno, M. Kimata, and H. Ohta, *Rev. Sci. Instr.* **79**, 103903 (2008).
- [48] E. Ohmichi, N. Mizuno, M. Kimata, H. Ohta, and T. Osada, *Rev. Sci. Instr.* **84**, 013904 (2009).
- [49] D. M. S. Bagguley, J. H. E. Griffiths, *Nature*, **162**, 538 (1948).
- [50] M. H. L. Pryce, *Nature*, **162**, 539 (1948).
- [51] A. Dankert, *ESR – Messungen niedrigdimensionaler Systeme mithilfe der Drehmomentmethode*, Diploma thesis, TU Dresden (2010).
- [52] A. Oosawa, M. Ishii, and H. Tanaka, *J. Phys. Condens. Matter* **11**, 265 (1999).
- [53] T. Nikuni, M. Oshikawa, A. Oosawa, and H. Tanaka, *Phys. Rev. Lett.* **84**, 5868 (2000).
- [54] H. Nojiri, H. Kageyama, Y. Ueda, K. Onizuka, and M. Motokawa, *J. Phys. Soc. Jpn.* **68**, 2906 (1999).
- [55] H. Nojiri, H. Kageyama, Y. Ueda, and M. Motokawa, *J. Phys. Soc. Jpn.* **72**, 3243 (2003).
- [56] M. Jaime, V. F. Correa, N. Harrison, C. D. Batista, N. Kawashima, Y. Kazuma, G. A. Jorge, R. Stein, I. Heinmaa, S. A. Zvyagin, Y. Sasago, and K. Uchinokura, *Phys. Rev. Lett.* **93**, 087203 (2004).
- [57] V. S. Zapf, D. Zocco, B. R. Hansen, M. Jaime, N. Harrison, C. D. Batista, M. Kenzelmann, C. Niedermayer, A. Lacerda, and A. Paduan-Filho, *Phys. Rev. Lett.* **96**, 077204 (2006).
- [58] A. A. Aczel, Y. Kohama, C. Marcenat, F. Weickert, M. Jaime, O. E. Ayala-Valenzuela, R. D. McDonald, S. D. Selesnic, H. A. Dabkowska and G. M. Luke, *Phys. Rev. Lett.* **103**, 207203 (2009).

- [59] M. Kofu, J.-H. Kim, S. Li, S.-H. Lee, H. Ueda, Y. Qiu, H.-J. Kang, M.A. Green, and Y. Ueda, *Phys. Rev. Lett* **102**, 037206 (2009).
- [60] T. Nakajima, H. Mitamura, and Y. Ueda, *J. Phys. Soc. Jpn.* **75**, 054706 (2006).
- [61] A. A. Aczel, Y. Kohama, M. Jaime, K. Ninios, H. B. Chan, L. Balicas, H. A. Dabkowska, and G. M. Luke, *Phys. Rev. B* **79**, 100409(R) (2009).
- [62] M. Kofu, H. Ueda, H. Najiri, Y. Oshima, T. Zenmoto, K. C. Rule, S. Gerischer, B. Lake, C. D. Batista, Y. Ueda, and S.-H. Lee, *Phys. Rev. Lett.* **102**, 177204 (2009).
- [63] A. A. Aczel, P. R. Provencher, H. A. Dabkowska, and G. M. Luke, *Jour. of Cryst. Growth* **310**, 870 (2008).
- [64] S. A. Zvyagin, M. Ozerov, E. Čizmar, D. Kamenskyi, S. Zherlitsyn, T. Herrmannsdörfer, J. Wosnitza, R. Wünsch and W. Seidel, *Rev. Sci. Instr.*, **80**, 073102 (2009).
- [65] O. Cepas, T. Sakai, and T. Ziman, *Prog. Theor. Suppl.* **145**, 43 (2002).
- [66] B. Leuenberger, A. Stebler, H. U. Güdel, A. Furrer, R. Feile, and J. K. Kjems, *Phys. Rev. B* **30**, 6300 (1984).
- [67] H. Tanaka *et al.* *Physica (Amsterdam)* **246-247B**, 545 (1998).
- [68] K. Takano, K. Kubo, and H. Sakamoto, *J. Phys. Condens. Matter* **8**, 6405 (1996).
- [69] T. Tonegawa, K. Okamoto, T. Hikihara, Y. Takahashi, and M. Kaburagi, *J. Phys. Soc. Jpn.* **69**, 332 (2000).
- [70] K. Okamoto, T. Tonegawa, and M. Kaburagi, *J. Phys. Condens. Matter* **15**, 5979 (2003).
- [71] H. Kikuchi, Y. Fujii, M. Chiba, S. Mitsudo, and T. Idehara, *Physica B* **329**, 967-968 (2003).
- [72] H. Kikuchi, Y. Fujii, M. Chiba, S. Mitsudo, T. Idehara, T. Tonegawa, K. Okamoto, T. Sakai, T. Kuwai, and H. Ohta, *Phys. Rev. Lett* **94**, 227201 (2005).
- [73] G. Gattow and J. Zeeman, *Acta Kristallogr.* **11**, 866-872 (1958).
- [74] F. Zigan and H. D. Schuster, *Z. Kristallogr.* **135**, 416 (1972).
- [75] R. D. Spence and R. D. Ewing, *Phys. Rev.* **112**, 1544 (1958).
- [76] M. Garber and R. Wagner, *Physica* **26**, 777 (1960).
- [77] N. D. Love, T. K. Duncan, P. T. Bailey, and H. Forstat, *Phys. Lett. A* **33**, 290 (1970).
- [78] P. F. Sullivan and G. Seidel, *Phys. Rev.* **173**, 679 (1968).
- [79] E. L. Belokoneva, Yu. K. Gubina, and J. B. Forsyth, *Phys. Chem. Minerals* **28**, 498-507 (2001).

-
- [80] P.W. Anderson, Phys. Rev. **115**, 2 (1959).
- [81] B. J. Reddy and K. B. N. Sarma, Solid State Commun. **38**, 547-549 (1981).
- [82] T. Kamikawa, S. Okubo, T. Kunimoto, H. Ohta, Y. Inagaki, H. Kikuchi, T. Saito, M. Azuma, and M. Takano, J. Magn. Magn. Mat. **272-276**, pp. 912-913 (2004).
- [83] H. Ohta, S. Okubo, T. Kamikawa, T. Kunimoto, Y. Inagaki, H. Kikuchi, T. Saito, M. Azuma, and M. Takano, J. Phys. Soc. Japan **72**, 2464-2467 (2003).
- [84] S. Okubo, T. Kamikawa, T. Kunimoto, Y. Inagaki, H. Ohta, H. Nojiri, and H. Kikuchi, J. Magn. Magn. Mat. **272-276**, 912-913 (2004).
- [85] K. C. Rule, A. U. B. Wolter, S. Süllow, D. A. Tennant, A. Brühl, S. Köhler, B. Wolf, M. Lang, and J. Schreuer, Phys. Rev. Lett. **100**, 117202 (2008).
- [86] M. Gibson, K. C. Rule, A. U. B. Wolter, J.-U. Hoffmann, O. Prokhnenko, D. A. Tennant, S. Gerischer, M. Kraken, F. J. Litterst, S. Süllow, J. Schreuer, H. Luetkens, A. Brühl, B. Wolf, and M. Lang, Phys. Rev. B **81**, 140406 (2010).
- [87] K. C. Rule, D. A. Tennant, J.-S. Caux, M. C. R. Gibson, M. T. F. Telling, S. Gerischer, S. Süllow, and M. Lang, Phys. Rev. B **84**, 184419 (2011).
- [88] K. C. Rule, M. Reehuis, M. C. R. Gibson, B. Ouladdiaf, M. J. Gutmann, J.-U. Hoffmann, S. Gerischer, D. A. Tennant, S. Süllow, and M. Lang, Phys. Rev. B **83**, 104401 (2011).
- [89] H.-J. Mikeska and C. Luckmann, Phys. Rev. B **77**, 054405 (2008).
- [90] J. Kang, C. Lee, R. K. Kremer, and M.-H. Whangbo, J. Phys. Condens. Matter **21**, 392201 (2009).
- [91] H. Jeschke, I. Opahle, H. Kandpal, R. Valenti, H. Das, T. Saha-Dasgupta, O. Janson, H. Rosner, A. Brühl, B. Wolf, M. Lang, J. Richter, S. Hu, X. Wang, R. Peters, T. Pruschke, and A. Honecker, Phys. Rev. Lett **106**, 217201 (2011).
- [92] J. Wosnitza, T. Herrmannsdörfer, Y. Skourski, S. Zherlitsyn, S. A. Zvyagin, O. Drachenko, H. Schneider, and M. Helm, AIP Conf. Proc. **1003**, 311-315, (2008).
- [93] Y. Skourski, M. D. Kuz'min, K. P. Skokov, A. V. Andreev, and J. Wosnitza, Phys. Rev. B **83**, 214420 (2011).
- [94] K.-Y. Choi, Y. H. Matsuda, and H. Nojiri, Phys. Rev. Lett. **96**, 107202 (2006).
- [95] B. S. Tsukerblat and M. I. Belinsky, *Magnetochemistry and Radiospectroscopy of Exchange Clusters*, Shtiintsa: Kishinev, USSR, (1983).
- [96] M. I. Belinsky, private communication.
- [97] B. Tsukerblat, A. Tarantul, and A. Müller, J. of Chem. Phys. **125**, 054714 (2006).
- [98] B. Tsukerblat, A. Tarantul, and A. Müller, Solid State Sciences **10**, 1814-1819 (2006).

- [99] M. Hagiwara, Z. Honda, K. Katsumata, A. K. Kolezhuk, and H.-J. Mikeska, Phys. Rev. Lett. **91**, 177601 (2003).
- [100] A. Honecker, S. Hu, R. Peters, and J. Richter, J. Phys. Condens. Matter **23**, 164211 (2011).
- [101] F. Aimo, S. Krämer, M. Klanjšek, M. Horvatić, and C. Berthier, Phys. Rev. B **84**, 012401 (2011).
- [102] E.S.R. Gopal, *Specific heats at low temperature*, Heywood books, London (1966), p. 102.
- [103] F. Aimo, S. Krämer, M. Klanjšek, M. Horvatić, C. Berthier, and H. Kikuchi, Phys. Rev. Lett. **102**, 127205 (2009).
- [104] Ch. Rüegg, N. Cavadini, A. Furrer, H.-U. Güdel, K. Krämer, H. Mutka, A. Wildes, K. Habicht, and P. Vorderwisch, Nature, **423**, 62, (2003).
- [105] T. Nikuni, M. Oshikawa, A. Oosawa, H. Tanaka, Phys. Rev. Lett. **84**, 5869 (2000).
- [106] M. Collins and O. A. Petrenko, Can. J. Phys. **75** 605 (1997).
- [107] A. V. Chubukov and D. I. Golosov, J. Phys.: Condens. Matter, **3**, 69 (1991).
- [108] B. Morosin and E. C. Lingafelter, Acta Crystallogr. **13**, 807 (1960).
- [109] L. Helmholz and R. F. Kruh, J. Am. Chem. Soc. **74** (5), pp 1176-1181, (1952).
- [110] T. Ono, H. Tanaka, H. Aruga Katori, F. Ishikawa, H. Mitamura, and T. Goto, Phys. Rev. B **67**, 104431 (2003).
- [111] R. L. Carlin, R. Burriel, F. Palacio, R. A. Carlin, S. F. Keij, and D. W. Carnegie, J. Appl. Phys. **57**, 3351 (1985).
- [112] H. Tanaka et al., Prog. Theor. Phys. Suppl. **145**, 101 (2002).
- [113] R. Coldea, D. A. Tennant, R. A. Cowley, D. F. McMorrow, B. Dorner, and Z. Tylczynski, J. Phys. Condens. Matter **8**, 7473 (1997).
- [114] R. Coldea, D. A. Tennant, R. A. Cowley, D. F. McMorrow, B. Dorner, and Z. Tylczynski, Phys. Rev. Lett. **79**, 151 (1997).
- [115] T. Ono, H. Tanaka, O. Kolomiyets, H. Mitamura, T. Goto, K. Nakajima, A. Oosawa, Y. Koike, K. Kakurai, J. Klenke, P. Smeibidl, and M. Meissner, J. Phys. Condens. Matter, **16**, 773778 (2004).
- [116] R. Coldea, D. A. Tennant, A. M. Tsvetik, and Z. Tylczynski, Phys. Rev. Lett. **86**, 1335 (2001).
- [117] R. Coldea, D. A. Tennant, K. Habicht, P. Smeibidl, C. Wolters, and Z. Tylczynski, Phys. Rev. Lett **88**, 137203 (2002).

- [118] H. Tsujii, C. R. Rotundu, T. Ono, H. Tanaka, B. Andraka, K. Ingersent, and Y. Takano, *Phys. Rev. B* **76**, 060406(R) (2007).
- [119] W. Zheng, R. R. P. Singh, R. H. McKenzie, and R. Coldea, *Phys. Rev. B* **71**, 134422 (2005).
- [120] Y. Tokiwa, T. Radu, R. Coldea, H. Wilhelm, Z. Tylczynski, and F. Steglich, *Phys. Rev. Lett* **73**, 134414 (2002).
- [121] S. Miyahara, K. Ogino, and N. Furukawa, *Physica B* **378-380**, 587 (2006).
- [122] N. A. Fortune, S. T. Hannahs, Y. Yoshida, T. E. Sherline, T. Ono, H. Tanaka, and Y. Takano, *Phys. Rev. Lett.* **102**, 257201 (2009).
- [123] M. Sharnoff, *J. Chem. Phys.* **41**, 2203 (1964).
- [124] M. Sharnoff, *J. Chem. Phys.* **42**, 3383 (1965).
- [125] J. M. Schrama , *Physica B* **256-258**, 637 (1998).
- [126] K. Yu. Povarov, A. I. Smirnov, O. A. Starykh, S. V. Petrov, and A. Ya. Shapiro, *Phys. Rev. Lett.* **107**, 037204 (2011).
- [127] A. I. Smirnov, K. Yu. Povarov, S. V. Petrov, and A. Ya. Shapiro, *Phys. Rev. B* **85**, 184423 (2012).
- [128] A. G. Anders and S. V. Volotski , *J. Magn. Magn. Mat.* **31-34**, 1169-1170 (1983).
- [129] L. J. De Jongh, A. C. Bottermann, F. R. de Boer, and A. R. Miedema , *J. Appl. Phys.* **40**, 1363 (1969).

Acknowledgements

I am deeply thankful to my supervisor Prof. Jochen Wosnitza, whose guidance, support, and advices from the beginning to the end enabled me to accomplish this thesis. I am deeply thankful to my scientific advisor Dr. Sergei Zvyagin for the constant scientific support, fruitful discussions, and general guidance. My special gratitude goes to Prof. Bernd Pilawa for his kind consent to be the second reviewer.

It is my pleasure to thank my colleagues at the Dresden High Magnetic Field Laboratory for the nice working atmosphere and a lot of fruitful discussions. I thank Mykhaylo Ozerov for his support in pulsed-field experiments, Oleg Ignatchik, André Dankert, Artem Pronin, Marc Uhlarz, Yurii Skourski, and Oleksiy Drachenko for the many fruitful discussions. I would like to acknowledge the technical support of Uwe Bartheld, Oliver Kersten, Ringo Sobiella, and Karsten Schulz.

Special thanks to F. Wolff-Fabris, A. Aczel, H. A. Dabkowska, and C. Petrovic for providing the samples.

I would like to appreciate the help of Hans Engelkamp and Popori Gogoi from the High Field Magnetic Laboratory (Nijmegen, the Netherlands) with the FIR experiments in magnetic fields up to 30 T.

I am deeply obliged to my teachers and former supervisors Prof. Alexander Anders and Victor Gorbach (Kharkiv National University, Ukraine), who introduced me in the world of physics and gave me the knowledge and skills necessary for becoming a scientist.

My special thank to my family and friends for constant encouragement during my way to the doctor degree.

Finally, I would like to acknowledge the support of Deutsche Forschungsgemeinschaft and EuroMagNET II.

List of publications

D. Kamenskyi, J. Wosnitza, J. Krzystek, A.A. Aczel, H.A. Dobkowska, A. Dobkowski, G.M. Luke, and S.A. Zvyagin

High – field ESR studies of the quantum spin – dimer system $Ba_3Cr_2O_8$

Journal of Low Temperature Physics **170**, 231 (2013).

S.A. Zvyagin, M. Ozerov, E. Čížmàr, D. Kamenskyi, S. Zherlistyn, T. Herrmannsdörfer, J. Wosnitza, R. Wünsch, and W. Seidel

Terahertz – range free – electron laser electron spin resonance spectroscopy : Techniques and applications in high magnetic fields

Review of Scientific Instruments **80**, 073102 (2009).

